Aramco Journal of Technology

WINTER 2020

The *Aramco Journal of Technology* is published quarterly by the Saudi Arabian Oil Company, Dhahran, Saudi Arabia, to provide the company's scientific and engineering communities a forum for the exchange of ideas through the presentation of technical information aimed at advancing knowledge in the hydrocarbon industry.

Editor

William E. Bradshaw
william.bradshaw.1@aramco.com.sa
tel: +966-013-876-0498

Production Coordination

Richard E. Doughty
Corporate Publications, Aramco Americas

Design

Graphic Engine Design Studio
Austin, Texas, U.S.A.

The *Aramco Journal of Technology* gratefully acknowledges the assistance, contribution and cooperation of numerous operating organizations throughout the company.

ISSN 1319-2388

Contents

A Systematic Approach to Deploy a Novel Non-Damaging Fracturing Fluid to Field

Prasad B. Karadkar, Mohammed I. Alabdrabalnabi, Dr. Feng Liang, and Adrian Buenrostro

Abstract /

Guar gum and its derivatives-based fracturing fluids are most commonly used in hydraulic fracturing. For high temperature wells, guar-based fracturing fluids need to be formulated with higher polymer loading and at a high pH, which leaves insoluble residue with a tendency to form scales with divalent ions. In this article, a systematic approach to field deploy a novel low polymer loading, non-damaging acrylamide-based fracturing fluid system is presented.

A thermally stable acrylamide-based polymer with a reduced polymer loading of 30% to 40% less than a guar-based fracturing fluid was considered to minimize formation damage concerns. For successful field deployment, a novel non-damaging fracturing fluid (NDFF) was evaluated in the following sequence: chemical management and quality control, optimization of fracturing fluid formulations with field water, field-mixing procedure, on-site QA/QC, friction analysis, leakoff analysis, data fracture analysis and execution of the main fracturing treatment. In both scenarios, batch mixing and on the fly mixing of linear gel were evaluated. The friction of the cross-linked fluid was analyzed by using a bottom-hole gauge. The fluid efficiency was evaluated during the data fracture analysis.

This article presents rheological studies at bottom-hole static temperatures (BHST) and cool-down temperatures of selected well candidates that demonstrate superior thermal stability of this novel fracturing fluid. With polymer loading of 25 lb/1,000 gal, the fluid viscosity stayed above 300 cP at 100 1/s shear rate for 2 hours at 290 °F. The fracturing fluid formulations were optimized using both live and encapsulated breakers with a high-pressure, high temperature (HPHT) rheometer. Due to the fast hydration of the base polymer, the linear gel was mixed in batches, and while on the fly during the main fracturing treatment.

The downhole gauge observed a slightly higher friction at a higher pumping rate during data fracture for this novel fracturing fluid in comparison to the guar-based fracturing fluid. The main fracturing treatment was successfully executed with a 45 barrel per minute (bbl/min) to 50 bbl/min pumping rate with an increased proppant concentration up to 5 pounds per gallon (ppa) using a 30/50 high strength proppant (HSP).

The fracturing fluid system based on the novel acrylamide-based terpolymer offers advantages over guar-based fracturing fluid such as low polymer loading, excellent high temperature stability, and reduced formation damage.

This article presents a systematic approach and lessons learned during novel fracturing fluid deployment.

Introduction

Hydraulic fracturing is commonly used in stimulating low permeability or damaged reservoirs. In hydraulic fracturing operations, a fracturing fluid is pumped to crack open the formation. Linear fluid is typically pumped first in pad or pre-pad treatment to initiate fractures and create the fracture geometry. A proppant laden fluid is later injected to further increase the length and width of the fractures in the formations.

At the end of a fracturing job, the pumping pressure drops. As a result, the fractures close onto the proppant, which are used to keep the fractures open during oil and gas production. The created fracture networks will facilitate the efficient flowing and production of hydrocarbons from the reservoirs.

The most commonly used hydraulic fracturing fluids are water-based fluids, such as slick water, linear fluids, cross-linked fluids, foamed fluids, and viscoelastic surfactant fluids[1-6]. For brittle shale formations, a slick water fluid system is typically used to create a complex fracture network[7]. Slick water fluids are comprised mostly of water, with low dosages of additives, including friction reducers, biocides, surfactants, scale inhibitors, etc. An acrylamide-based polymer or copolymers are the typical friction reducers. In recent years, the slick water fracturing has become a standard treating technique in the Barnett, Haynesville, or Marcellus shales[8, 9].

Slick water treatments are usually pumped at a high pumping rate — typically more than 60 barrels per minute (bbl/min) — carrying low concentrations of proppant, often at small proppant mesh sizes such as 100 mesh[4], and generating narrow fractures[10, 11]. At such high pumping rates, a high molecular weight friction reducer is used to reduce the friction pressure and related pumping power by as much as 70% to 80%.

Linear fluids are uncross-linked solutions of polymers such as guar, guar derivatives, cellulose, cellulose derivatives, or synthetic polymers such as acrylamide-based polymers and copolymers. Linear fluid viscosity typically has higher viscosity than slick water; thereby showing a much better proppant transporting capability.

For ductile rock/shale, cross-linked fluids are typically used to create the conventional bi-wing fractures. The most commonly used cross-linked fracturing fluids are guar or guar-based derivatives, including carboxymethyl hydroxypropyl guar (CMHPG), carboxymethyl guar, or hydroxypropyl guar. As the well depth increases, the temperature and formation pressure become more severe and extend into the high-pressure, high temperature (HPHT) range. Although the cross-linked guar or derivatized guar fluids can work at temperatures up to approximately 350 °F when formulated with high polymer loading and high fluid pH, these types of fluids can damage proppant packs and formations due to the insoluble residue in guar-based polymers.

Using high fluid pH to achieve high temperature fluid stability can promote the formation of undesirable divalent ion scales in the high pH environment. Various synthetic acrylamide-based fluids have been developed and reported as cost-effective alternatives. Early studies include high molecular weight acrylamide-acrylate copolymer crosslinking with metal crosslinkers such as chromium[12] and titanium or zirconium compounds[13], and acrylamide-methacrylate copolymer systems crosslinking with chromium[14].

To improve the thermal stability of the synthetic acrylamide-based polymer at high temperature, a 2-acylamdio-2-methylpropanesulfonic acid (AMPS) monomer was introduced into the polymer system. Funkhouser and Norman (2003)[15], (2006)[16], and Funkhouser et al. (2010)[17] have reported a terpolymer of AMPS, acrylamide and acrylic acid or its salts. This system has been proven to work at temperatures between 350 °F and 400 °F.

These terpolymers have been used in very high concentrations as high as 86 pounds per 1,000 gallons (pptg)[17]. Large doses of acrylamide-based polymers and copolymers may still cause formation and proppant pack damages, due to reasons like the incomplete breaking of the polymers at high concentrations. Gupta and Carman (2011)[18] reported a high temperature fluid on using a terpolymer of acrylamide, and AMPS and vinyl phosphonate crosslinking with a zirconium-based crosslinker. This system can be used at temperatures up to 450 °F. Gaillard et al. (2013)[19] reported on using acrylamide-based associative polymers crosslinking with zirconium as the fracturing fluid. The anionic polymers investigated were acrylamide-based terpolymers and tetrapolymers prepared from monomers such as sodium acrylate, sodium acrylamido-tertiary-butyl sulfonate, and a monomer with hydrophobic groups.

Liang et al. (2016)[20] and (2017)[21] reported a series of the synthetic acrylamide-based terpolymers as high temperature fracturing fluids, cross-linked either with the nano-sized particulate crosslinker, or cross-linked with the nanomaterials enhanced zirconium crosslinkers.

Recently, a high temperature, low polymer loading novel acrylamide copolymer-based cross-linked fracturing fluid system was developed for application temperatures ranging from 280 °F to 450 °F[22]. The fluid system has demonstrated robust stability at elevated temperatures while hardly causing any damages in core flow and proppant pack conductivity under laboratory testing conditions.

In this article, further development work is discussed in an effort to deploy this fluid technology to the field for real job execution. For successful field deployment, the novel non-damaging fracturing fluid (NDFF) was evaluated in the following sequence: chemical management, pre-job lab testing, field mixing procedure, on-site QA/QC, data fracture analysis, friction analysis, and finally, a main fracturing treatment to fully validate the NDFF capacity for proppant fracturing execution. Four field trials were successfully performed using NDFF.

In this article, one field case study is presented to demonstrate the journey from laboratory investigations to field deployment.

Pre-Job Laboratory Testing

The NDFF was optimized before the job to meet fluid stability criteria for the selected well candidate. A water sample from the designated water well and a chemical sample from the respective batches were collected for pre-job lab testing. A water analysis was performed to check the compatibility of the water with fracture fluid and the potential risk of scale formation when mixed with the formation water.

The NDFFs were then evaluated with different tests such as a hydration test, a vortex closure test, a crosslink/lip time test, and a rheology test at HPHT conditions.

Fracture Fluid Formulation

Table 1 lists the 25 ppt NDFF formulation. It contains a variety of different additives that are commonly used in a typical fracture fluid. Liquid gel concentrate (LGC) was produced using a 2.5 lb/gal thermally stable acrylamide-based polymer and mineral oil. It is a water in oil emulsion having 264 cP at 511 1/s at 80 °F. The 25 lb/1,000 pptg NDFF was prepared by using 10 gal/1,000 gal (gpt) polymer LGC loading. A weak organic acid was used as a buffer to maintain the fracturing fluid system's pH at approximately five.

A metal crosslinker was used to crosslink the NDFF system that can work up to 400 °F. In total, three breakers were used in the breaker package, depending on fluid stability requirements. An encapsulated breaker

Table 1 *25 ppt NDFF formulation.*

Additive	Unit	Loading
Biocide	ppt	0.5
Polymer	gpt	10
Surfactant	gpt	2.0
Clay Control	gpt	2.5
Gel Stabilizer	gpt	3.0
Buffer	gpt	3 - 4
Crosslinker	gpt	0.6 - 0.9
Live Breaker	gpt	1 - 5
Encap. Breaker	ppt	5.0
Low Temperature Live Breaker	gpt	0.5 - 1

was designed for a fluid stability of more than 300 °F, a live breaker was designed for 250 °F to 300 °F, and a low temperature live breaker was designed for an application temperature below 250 °F.

Table 1 also lists the typical loading range of the additives. Depending on the fracture fluid's stability requirement, the buffer, crosslinker, and breaker loading are optimized, and discussed next. It is important to mention that the performance of the polymer in this study might be affected by the interactions with some additives. Fluid formulation has been optimized for different temperature ranges in consideration of the cool-down conditions.

The listed additives in this article are not the only ones accepted to work with the proposed polymer, but were part of the ones used for this case. Implementation of other additives is possible. The corresponding polymer performance needs to conduct the evaluation of possible effects on additives implementation as they can enhance or degrade the final polymer-based gel performance.

Rheology

Rheological testing was conducted to evaluate the stability of the NDFF under bottom-hole conditions. The rheological properties influences fluid leakoff, which affects fracture width and fracture extension[23]. The linear gel of the NDFF was prepared by hydrating 10 gpt LGC polymer in freshwater added with biocide. The apparent viscosity of the linear gel was measured at a different temperature using a Fann 35 viscometer at 511 1/s shear rate using a R1B1 rotor bob combination. Figure 1 shows the viscosity of the 25 ppt linear polymer in NDFF at different temperatures. This chart was utilized to quality check linear fluid in both the lab and field-testing.

To prepare the cross-linked NDFF, the desired amount of surfactant, clay control agent, gel stabilizer, breaker, buffer and crosslinker was added and

Fig. 1 *Linear 25 ppt NDFF viscosity at different temperatures.*

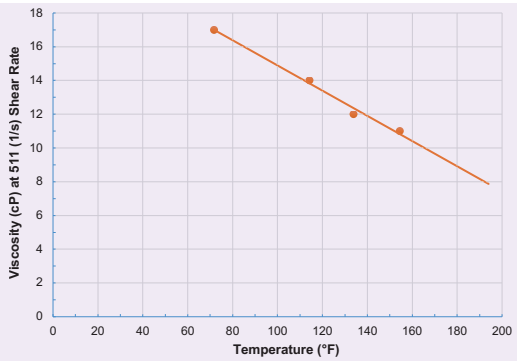

mixed well. The pH of the NDFF was adjusted to five using a buffer before crosslinker addition. The required crosslinking/lip time was achieved by varying the buffer loading. The required lip time, 3 minutes 30 seconds, was achieved using 3.2 gpt buffer loading and by maintaining the fracture fluid system's pH at five. The rheological tests were performed using shear history simulation stated in BS ISO standard 13503-1:2003. Figure 2 shows the NDFF after crosslinking.

Figure 3 shows the 25 ppt NDFF stability at different temperatures for one of the field trials. The fluid stability was judged by viscosity measurements with respect to time at 100 1/s with shear cycles. The fluid stability time was defined as the time required to reach 300 cP viscosity at 100 1/s. The bottom-hole static temperature (BHST) of the selected well candidate was 290 °F, which was considered for pad stage fluid optimization. The cool-down temperatures, 270 °F, 240 °F, and 210

Fig. 2 *Picture of fluid developed "lip" after crosslinking the NDFF.*

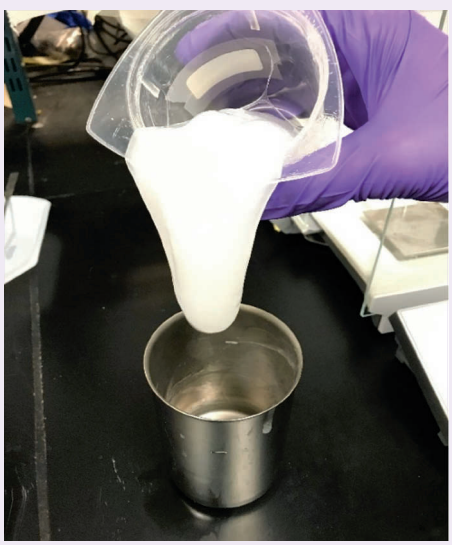

Fig. 3 *The 25 ppt NDFF rheology at different temperatures for one of the field trials.*

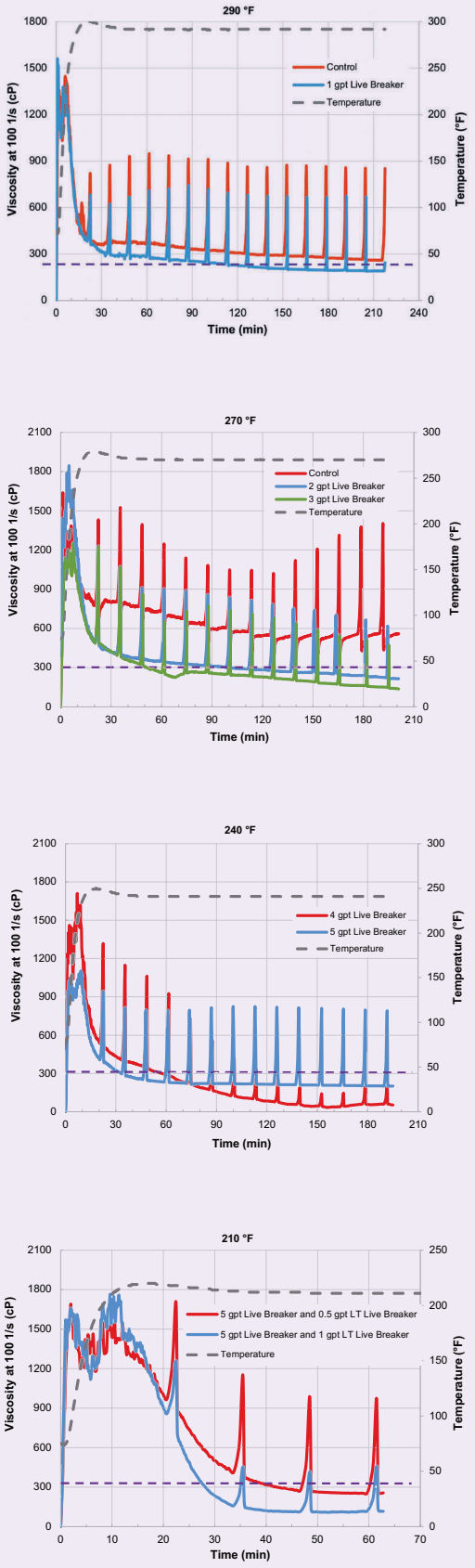

°F were considered for proppant laden stages fluid optimization. For each cool-down temperature, since the encapsulated breaker is relatively stable, only live breaker loading was optimized to achieve the desired fluid stability time.

At 290 °F, the control test without breakers shows a thermal degradation rate of the cross-linked fluid. The pump time for the selected well candidate was 60 minutes, so the fluid stability for this temperature was desired to be 60 minutes, which was achieved by the addition of 1 gpt of live breaker.

At 270 °F, live breaker loading was increased to 2 gpt and 3 gpt, which provided 90 minutes and 45 minutes of fluid stability, respectively. At 240 °F, live breaker loading was further increased to 4 gpt and 5 gpt, which provided 60 minutes and 30 minutes of stability, respectively. At 210 °F, a low temperature live breaker was introduced in addition to the live breaker for aggressive breaking at lower temperature ranges. The low temperature live breaker was increased from 0.5 gpt to 1 gpt to achieve a faster break time of 40 minutes and 28 minutes at 210 °F; and a 5 gpt live breaker was also kept for additional breaking performance.

In all stages, a 5 ppt encapsulated breaker was also added for better fracture conductivity cleanup after closure. The fracking engineer designed a blender schedule for the selected well candidate utilizing the optimized fluid formulation. Similar steps were followed in pre-job lab testing to conduct four different field trials for successful field deployment of this new technology.

Field Execution

The NDFF was successfully field deployed in four different well candidates. Out of four, the NDFF was semi-batch mixed for one field trial and for the rest of the three trials the fluid was mixed on the fly. Before the actual field job, a yard test was performed where a tote tank full of LGC was pumped through with a liquid additive pump from a blender at a rate of 21 gal/min for 30 minutes. This yard test was performed only to check LGC pumpability with liquid additive pumps for on the fly mixing.

Figure 4 shows a typical site layout for fracking operation. While during the semi-batch mixing only linear gel was prepared in the fracking tanks or water tanks batch wise, while all other additives, including proppant, were added on the fly. Linear gel was prepared by adding the desired amount of LGC polymer in a tank filled with field water and the mixture circulated by using a centrifugal pump. While during the on the fly mixing, LGC polymer was added in the LGC mixture and kept rolling. Water from water tanks, and polymer from the LGC mixture, were sucked using a blender and then mixed in a hydration tank.

The hydration tank has compartments where fluid gets enough residence time for full hydration. During the field job, linear gel from the hydration tank, additives from the chemicals trailer, and proppant were mixed in a blender tub and supplied to the suction side of the high-pressure pumps. The discharges from a

Fig. 4 *Typical site layout for a fracking operation.*

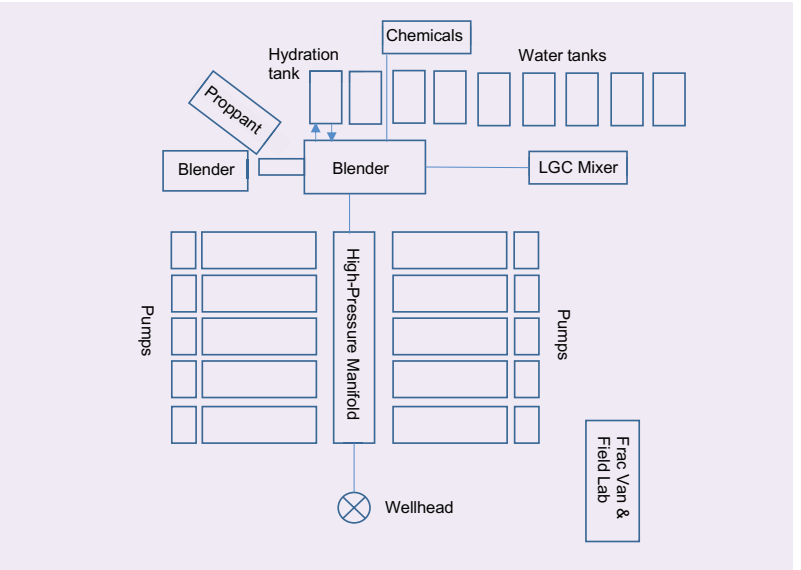

series of pumps were connected to the high-pressure manifold supplying the wellhead.

Quality Control On-site

The field case study described in this article was pumped semi-batch wise. A 4,000 bbl linear gel was prepared by mixing eight fracking tanks. Linear gel samples were collected from the tank for quality control, and viscosity adjustment was done by adding LGC polymer or water in the tank with circulation using a centrifugal pump.

Table 2 lists the quality control results using linear gel from each tank. The linear gel viscosity was achieved in the range from 17 cP to 19 cP at 511 1/s and buffer loading was measured as 4 gpt to get the desired lip time and pH. Batch mixing of the linear gel was very time-consuming and waste fluid was left in each tank bottom.

Table 3 lists the cross-linked NDFF quality control steps during the main fracturing treatment. Different samples during each stage were collected from a high-pressure manifold. The pH and lip time of each collected sample was measured. All steps in each substage were pumped as per plan, except step 4. There was an operational issue with the buffer liquid additive pump, which was addressed by switching to a backup pump. The pH during step 4 was recorded as 5.7, which delayed the crosslinking/lip time to 5 minutes and 11 seconds.

Figure 5 shows the proppant laden cross-linked 25 ppt NDFF collected at step 8 that shows uniform proppant suspension.

Table 3 *The quality control steps of the cross-linked NDFF during the main fracturing treatment.*

Step No.	Stage Name	pH	Lip Time (min:sec)
1	PAD 1	5.16	2:50
2	0.5 ppa R-30/50 HSP	5.26	2:45
3	1 ppa R-30/50 HSP	5.23	2:50
4	PAD 2	5.7	5:11
5	0.5 ppa R-30/50 HSP	5.1	2:55
6	1 ppa R-30/50 HSP	5.12	3:00
7	2 ppa R-30/50 HSP	5.11	3:45
8	3 ppa R-30/50 HSP	5.16	3:50
9	4 ppa R-30/50 HSP	5.24	3:20
10	5 ppa R-30/50 HSP	5.22	3:10

Table 2 *The quality control results of each batch mixed linear gel.*

Tank #	1	2	3	4	5	6	7	8	9	10
Fluid	Water	Linear Gel								Water
pH	7.7	7.1	7.08	7.12	7.13	7.15	7.18	7.21	7.08	7.57
Viscosity (cP) at 511 (1/s)	—	18	18	17	17	19	19	19	19	—
Buffer Loading (gpt)	—	4	4	4	4	4.2	4	4.2	4	—
Lip Time (min:sec)	—	4:30	4:00	4:10	3:50	3:55	4:10	3:45	3:50	—
Cross-linked pH	—	5.31	5.12	5.29	5.14	5.23	5.31	5.21	5.1	—

Fig. 5 *Proppant laden cross-linked 25 ppt NDFF collected during the main fracturing treatment.*

Data Fracture Analysis

A data fracture analysis was performed using cross-linked 25 ppt NDFF without proppant to simulate the main fracture treatment. The fracture diagnostic tests aids in designing and completing the main hydraulic fracturing treatment. This analysis helps to obtain more representative estimates of an instantaneous shut-in pressure (ISIP), fracture gradient, net fracture pressure, and fluid friction on real conditions, fluid efficiency, and fluid loss coefficients.

This information was used to optimize pad volume and select the best fluid-loss additives for the main treatment and to design the pumping schedule. Prior to the data fracture analysis, a downhole gauge was placed above the perforations to measure the downhole pressure for enhanced fracture performance analysis and friction analysis, which was successfully retrieved before the main fracture treatment.

Figure 6 shows the data fracture treatment plot using 25 ppt NDFF. The data fracture treatment was started with displacing wellbore fluids with 25 ppt cross-linked NDFF. This full wellbore displacement step was performed to obtain accurate downhole pressure readings for friction analysis. The data fracture analysis was continued with a step rate test by increasing the slurry rate from 15 bpm to 45 bpm with a 5-bpm rise in slurry rate. After achieving the maximum slurry pumping rate, i.e., 45 bpm, 25 ppt cross-linked NDFF was pumped for 10 minutes. The pumps were shutdown to evaluate hydrostatic pressure for friction analysis, ISIP, and pressure decline analysis.

A total of 577 bbl of 25 ppt cross-linked NDFF was pumped for the data fracture analysis; the ISIP was 11,745 psi with a 10,940-psi closure pressure. Using pressure decline data, the fluid efficiency was estimated to 15%. This low fluid efficiency was anticipated due to low polymer usages. For the main fracture treatment, the slurry rate was increased to 45 bpm from 40 bpm to quantify lower fluid efficiency. To improve the fluid efficiency, further improvement in fluid development is ongoing.

Friction Analysis

Bottom-hole treating pressure (BHTP) is critically required to design hydraulic fracturing jobs. In the absence of a bottom-hole gauge, the BHTP is calculated by using surface pressure, friction pressure, and hydrostatic pressure. The computed values of BHTP is subject to the assumption that the friction pressure and hydrostatic pressure calculations are reliable. While using newly developed fracturing fluid, it is critical to calibrate friction numbers for data acquisition software to estimate the BHTP in understanding formation behavior during treatment.

The downhole memory gauge was installed before the data fracture analysis, and successfully retrieved afterwards to calibrate the friction numbers. This analysis was carried out using a memory gauge, Kuster K10 Quartz at a depth of 13,000 ft measured depth (true vertical depth: 12,949 ft and well deviation: 24°). The friction numbers were estimated for a completion with an inside diameter of 2.93". The friction pressure is calculated based on the following formula:

Fig. 6 *The data fracture treatment plot using 25 ppt NDFF.*

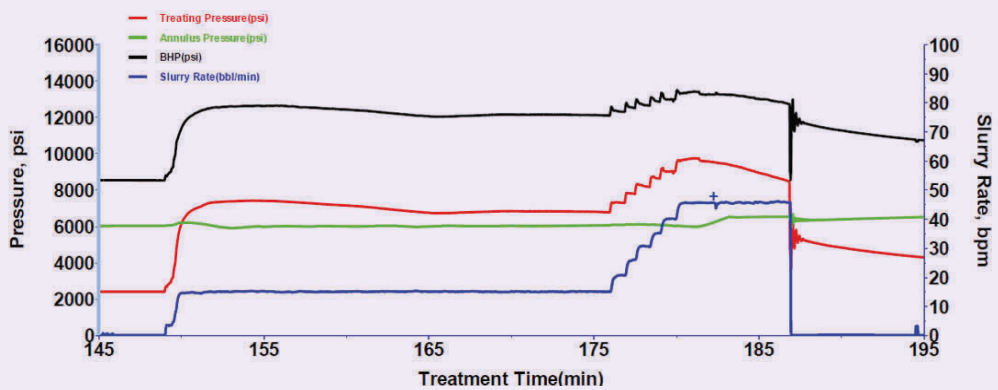

$$P_{friction} = P_{wellhead} + P_{hydrostatic} - BHTP. \quad (1)$$

The hydrostatic pressure was calculated to 6,330 psi by subtracting the wellhead ISIP from the bottom-hole ISIP. The bottom-hole ISIP was recovered from the memory gauge. This hydrostatic pressure was used in conjunction with the wellhead (from the surface gauge) and bottom-hole pressure (BHP) (from the memory gauge) to calculate friction numbers for different rates using Eqn. 1.

Table 4 lists the friction numbers at different rates for both cross-linked and linear NDFF.

The friction behavior of 40 ppt CMHPG fracture fluid was compared with 25 ppt NDFF, Fig. 7. The NDFF showed slightly higher than the conventional CMHPG fracture fluid. At 40 bpm, the NDFF showed 140 psi/1,000 ft friction pressure whereas the CMHPG fracture fluid showed 120 psi/1,000 ft.

Main Fracturing Treatment

The main fracturing treatment with 25 ppt NDFF was successfully pumped without any operational issues. Table 5 lists the stage names, and Fig. 8 shows the main fracturing treatment plot. The 25 ppt NDFF was pumped at 45 bbl/min with 3,000 bbl of slurry volume and then 241,000 lb of 30/50 high strength proppant (HSP) was placed. The proppant concentration was ramped from 0.5 pounds per gallon (ppa) up to 5 ppa of proppant concentration. The maximum BHP was recorded as 15,395 psi and the wellhead pressure (WHP) was 10,434 psi. After the main fracturing treatment, the ISIP was 6,775 psi and the bottom-hole ISIP was 12,996 psi.

During the flush step, a decrease in WHP was observed. It should show an increase in WHP as hydrostatic pressure is decreasing due to a reduction of proppant mixed slurry height. The higher slurry friction that was already discounted with the increase in proppant concentration could cause this. Further development in the NDFF to improve friction is ongoing.

Fig. 7 The friction comparison of (a) 25 ppt NDFF fracturing fluid, and (b) 40 ppt CMHPG fracturing fluid.

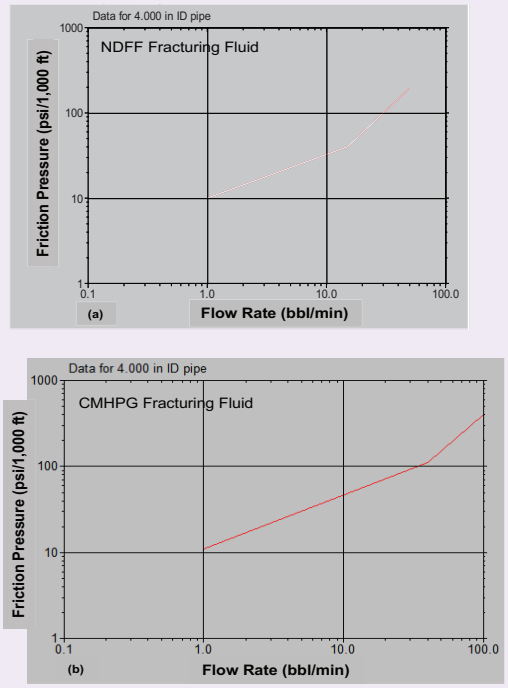

From Laboratory to Field Trials

Challenges from the field and the result of research and development provided a path to deploy the NDFF system in the field. For high temperature wells, guar-based fracturing fluids need to be formulated with

Table 4 The friction numbers at different rates for both cross-linked and linear NDFF.

Cross-linked 25 ppt NDFF					
Rate (bpm)	**BHP_Memory Gauge (psi)**	**WHP (psi)**	**P_Hydrostatic (psi)**	**P_Friction (psi)**	**P_Friction (psi/1,000 ft)**
15	12,460	6,760	6,330	630	44
20	12,625	7,260	6,330	965	67
25	12,910	7,780	6,330	1,200	83
30	13,100	8,170	6,330	1,400	97
35	13,150	8,560	6,330	1,740	120
40	13,320	9,000	6,330	2,010	139
45	13,460	9,620	6,330	2,490	172
Linear 25 ppt NDFF					
45	13,250	8,530	6,330	1,609	111

Table 5 *The stage design for the main fracturing treatment using 25 ppt NDFF.*

Step No.	Stage Name	Fluid Name	Rate (bbl/min)	Volume (gal)
1	PAD 1	25 ppt NDFF Cross-linked	45	12,000
2	0.5 ppa R-30/50 HSP	25 ppt NDFF Cross-linked	45	4,000
3	1 ppa R-30/50 HSP	25 ppt NDFF Cross-linked	45	4,000
4	PAD 2	25 ppt NDFF Cross-linked	45	22,000
5	0.5 ppa R-30/50 HSP	25 ppt NDFF Cross-linked	45	6,000
6	1 ppa R-30/50 HSP	25 ppt NDFF Cross-linked	45	8,000
7	2 ppa R-30/50 HSP	25 ppt NDFF Cross-linked	45	14,000
8	3 ppa R-30/50 HSP	25 ppt NDFF Cross-linked	45	18,000
9	4 ppa R-30/50 HSP	25 ppt NDFF Cross-linked	45	12,000
10	5 ppa R-30/50 HSP	25 ppt NDFF Cross-linked	45	10,000
11	Flush	25 ppt NDFF Linear gel	45	8,958

higher polymer loading and at a high pH, which leaves insoluble residue, enhancing formation damage concerns. During the research and development phase, polymer loading was reduced without compromising the proppant carrying capacity of the fracturing fluid.

A thermally stable acrylamide-based polymer with reduced polymer loading of 30% to 40% less than the guar-based fracturing fluid was developed to minimize formation damage concerns. Figure 9 shows different tasks involved in the deployment of the NDFF from the laboratory to the field. After research and development, a polymer and cross-linked package was synthesized to pilot scale with the collaboration of chemical manufacturing companies.

In chemical management tasks, sub-tasks like bulk size chemical manufacturing, MSDS preparation, logistic, import permit documentation, chemical handling, and storage were involved. After selecting the well candidate, based on water source, BHST and job design, the NDFF formulation was optimized during pre-job lab testing. Based on the limitations of the field equipment, semi-batch mixing or an on the fly mixing process was decided.

After transporting the chemicals to the location, QA/QC tests of the water sample and NDFF system were conducted to ensure everything was going as per plan. To redesign the job based on formation response, a data fracture analysis was conducted. Before the data fracture analysis, a downhole memory gauge was placed above the perforation to conduct friction analysis. After data fracture, the job was redesigned and planned for a rate higher than 45 bpm to mitigate reduced fluid efficiency — due to lower polymer loading. After data

Fig. 8 *The main fracture treatment plot of the 25 ppt NDFF.*

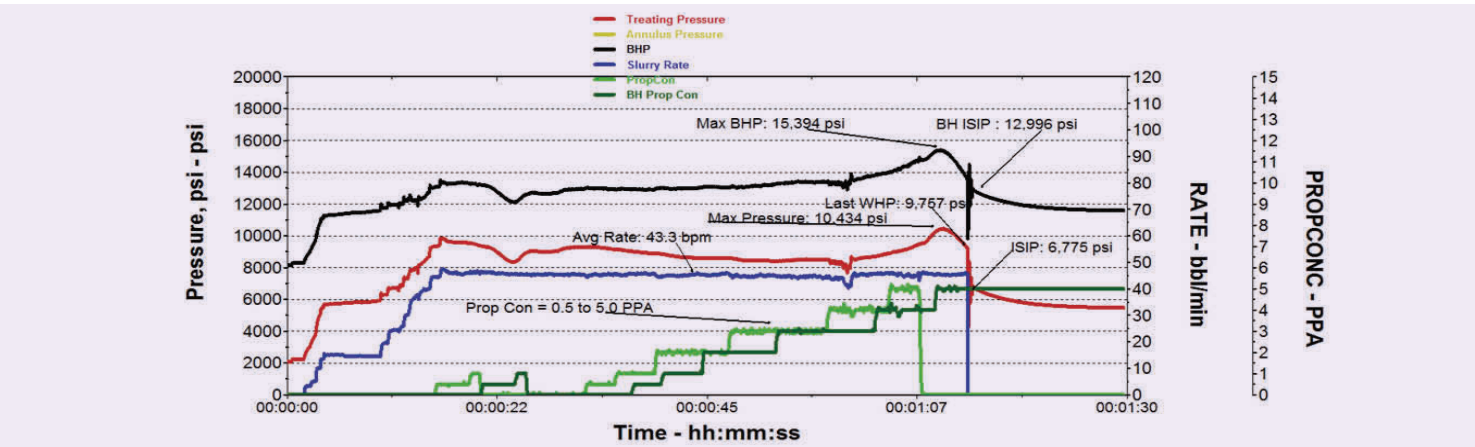

Fig. 9 *Different tasks involved in the deployment of the NDFF from the laboratory to the field.*

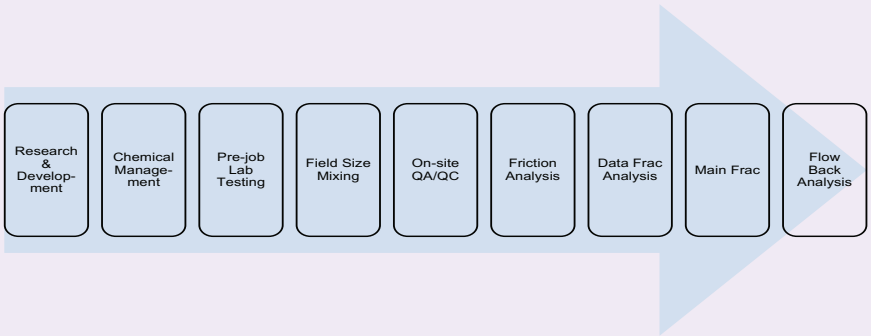

fracture, the main fracturing treatment was pumped without any operational issues. Finally, the well was flowed back for flow back analysis. The NDFF was pumped in four wells having different well completions and temperatures.

Conclusions

The novel acrylamide terpolymer-based NDFF system offers advantages over guar-based fracturing fluid such as low polymer loading, excellent high temperature stability and less formation damage. Based on efforts to transform this technology from laboratory to the field, the following conclusions can be drawn:

- Pre-job laboratory testing allows for breaker package optimization for selected well candidates with reduced polymer loading. The maximum BHST well candidate, 320 °F, was field-tested with 25 ppt base polymer loading.
- The NDFF can be mixed both semi-batch wise and on the fly.
- On-site quality control provided confirmation on fluid consistency, both in the lab and field environment.
- During data fracture analysis, the friction analysis, fluid efficiency, and formation response was evaluated to design the main fracturing treatment.
- The main fracturing treatment was successfully placed with 5 ppa proppant concentration; the maximum proppant concentration was tested to 7 ppa for other field trails.
- Despite observing a trend of higher friction than other polymer systems, the NDFF can confidently place proppant on a regular proppant fracture job while increasing the proppant pack retained conductivity as the amount of solid material is decreased compared with lower friction polymer systems.

Acknowledgments

The authors would like to express their sincere thanks to their colleagues Dr. Mohammed Bataweel and Justin Abel for their support during field implantation; and Brady Crane, Abdullah Garni, and Ahmad Busaleh for laboratory testing.

This article was prepared for presentation at the Offshore Technology Conference Asia, Kuala Lumpur, Malaysia, November 2-6, 2020.

References

1. Fink, J.K.: *Oil Field Chemicals*, Gulf Professional Publishing, MA, 2003, 495 p.
2. Al-Muntasheri, G.A.: "A Critical Review of Hydraulic Fracturing Fluids over the Last Decade," SPE paper 169552, presented at the SPE Western North American and Rocky Mountain Joint Meeting, Denver, Colorado, April 16-18, 2014.
3. Li, L., Al-Muntasheri, G.A. and Liang, F.: "A Review of Cross-linked Fracturing Fluids Prepared with Produced Water," *Petroleum*, Vol. 2, Issue 4, December 2016, pp. 313-323.
4. Wang, X., Sun, H., Zhou, J., Guerin, M., et al.: "A Non-Damaging Polymer Fluid System for Conventional and Unconventional Formations," SPE paper 174280, presented at the SPE European Formation Damage Conference and Exhibition, Budapest, Hungary, June 3-5, 2015.
5. Samuel, M., Card, R.J., Nelson, E.B., Brown, J.E., et al.: "Polymer-Free Fluid for Hydraulic Fracturing," SPE paper 38622, presented at the SPE Annual Technical Conference and Exhibition, San Antonio, Texas, October 5-8, 1997.
6. Kefi, S., Lee, J., Pope, T.L., Sullivan, P., et al.: "Expanding Applications for Viscoelastic Surfactants," *Oilfield Review*, Vol. 16, Issue 4, Winter 2004/2005, pp. 10-23.
7. Chong, K.K., Grieser, W.V., Passman, A., Tamayo, H.C., et al.: "A Completions Guide Book to Shale-Play Development: A Review of Successful Approaches toward Shale-Play Stimulation in the Last Two Decades," SPE paper 133874, presented at the Canadian Unconventional Resources and International Petroleum Conference, Calgary, Alberta, Canada, October 19-21, 2010.
8. Ketter, A.A., Daniels, J.L., Heinze, J.R. and Waters, G.: "A Field Study Optimizing Completion Strategies for Fracture Initiation in Barnett Shale Horizontal Wells," SPE paper 103232, presented at the SPE Annual Technical Conference and Exhibition, San Antonio, Texas, September 24-27, 2006.
9. King, G.E.: "Thirty Years of Gas Shale Fracturing: What Have We Learned?" SPE paper 133456, presented at the SPE Annual Technical Conference and Exhibition, Florence, Italy, September 19-22, 2010.

10. Palisch, T.T., Vincent, M.C. and Handren, P.J.: "Slick Water Fracturing: Food for Thought," SPE paper 115766, presented at the SPE Annual Technical Conference and Exhibition, Denver, Colorado, September 21-24, 2008.

11. Liang, F., Sayed, M., Al-Muntasheri, G.A., Chang, F.F., et al.: "A Comprehensive Review on Proppant Technologies," *Petroleum*, Vol. 2, Issue 1, March 2016, pp. 26-39.

12. Rhudy, J.S. and Knight, B.L.: "Fracturing Fluid," U.S. Patent No. 3,938,594, February 1976.

13. Williams, D.A., Horton, R.L., Newlove, J.C. and Chumley, R.E.: "Method of Treating Subterranean Formations Using a Non-Damaging Fracturing Fluid," U.S. Patent No. 5,007,481, April 1991.

14. Golinkin, H.S.: "Process for Fracturing Well Formations Using Aqueous Gels," U.S. Patent No. 4,137,182, January 1979.

15. Funkhouser, G.P. and Norman, L.R.: "Synthetic Polymer Fracturing Fluid for High Temperature Applications," SPE paper 80236, presented at the International Symposium on Oil Field Chemistry, Houston, Texas, February 5-7, 2003.

16. Funkhouser, G.P. and Norman, L.R.: "Methods of Fracturing Subterranean Zones Penetrated by Wellbores and Fracturing Fluids Therefore," U.S. Patent No. 6,986,391, January 2006.

17. Funkhouser, G.P., Holtsclaw, J. and Blevins, J.: "Hydraulic Fracturing under Extreme HPHT Conditions: Successful Application of a New Synthetic Fluid in South Texas Gas Wells," SPE paper 132173, presented at the SPE Deep Gas Conference and Exhibition, Manama, Kingdom of Bahrain, January 24-26, 2010.

18. Satya Gupta, D.V. and Carman, P.: "Fracturing Fluid for Extreme Temperature Conditions is just as Easy as the Rest," SPE paper 140176, presented at the Hydraulic Fracturing Technology Conference, The Woodlands, Texas, January 24-26, 2011.

19. Gaillard, N., Thomas, A. and Favero, C.: "Novel Associative Acrylamide-Based Polymers for Proppant Transport in Hydraulic Fracturing Fluids," SPE paper 164072, presented at the SPE International Symposium on Oil Field Chemistry, The Woodlands, Texas, April 8-10, 2013.

20. Liang, F., Al-Muntasheri, G.A. and Li, L.: "Maximizing Performance of Residue-Free Fracturing Fluids Using Nanomaterials at High Temperatures," SPE paper 180402, presented at the SPE Western Regional Meeting, Anchorage, Alaska, May 23-26, 2016.

21. Liang, F., Al-Muntasheri, G., Ow, H. and Cox, J.: "Reduced Polymer Loading, High Temperature Fracturing Fluids by Use of Nanocrosslinkers," *SPE Journal*, Vol. 22, Issue 2, April 2017, pp. 622-631.

22. Liang, F., Li, L., and Al-Muntasheri, G.A.: "Non-Damaging Fracturing Fluid System for High Temperature Unconventional Formations," SPE paper 183673, presented at the SPE Middle East Oil and Gas Show and Conference, Manama, Kingdom of Bahrain, March 6-9, 2017.

23. Al-Hulail, I.A., Karadkar, P., Al-Janabi, Y.H., Al-Khabaz, H., et al.: "The Future of Fracture Acidizing: A Low pH, Robust, and Residue-Free Cross-linked Fracturing Fluid," SPE paper 182891, presented at the Abu Dhabi International Petroleum Exhibition and Conference, Abu Dhabi, UAE, November 7-10, 2016.

About the Authors

Prasad B. Karadkar

M.S. in Chemical Engineering, Nagpur University

Prasad B. Karadkar is a Petroleum Engineer with the Production Technology Team of Saudi Aramco's Exploration and Petroleum Engineering Center – Advanced Research Center (EXPEC ARC). Prior to joining Saudi Aramco in April 2016, he worked as a Senior Technical Professional for Halliburton for 9 years. Prasad's areas of expertise include developing new fluid systems in the area of hydraulic fracturing, acidizing, diversion, and water shutoff.

He has authored and coauthored 16 papers, published one patent, and has several patent applications in process.

In 2003, Prasad received his B.S. degree in Chemical Engineering from Shivaji University, Kolhapur, India, and in 2007, he received his M.S. degree in Chemical Engineering from Nagpur University, Nagpur, India.

Mohammed I. Alabdrabalnabi

B.S. in Chemical Engineering, King Fahd University of Petroleum and Minerals

Mohammed I. Alabdrabalnabi joined Saudi Aramco in August 2015 as a Petroleum Engineer with the Production Technology Division of Saudi Aramco's Exploration and Petroleum Engineering Center – Advanced Research Center (EXPEC ARC).

His research interests include fracturing fluids, water shutoff fluid systems, sand control, and condensate banking.

Mohammed received his B.S. degree in Chemical Engineering from King Fahd University of Petroleum and Minerals (KFUPM), Dhahran, Saudi Arabia.

Dr. Feng Liang

Ph.D. in Organic Chemistry, Rice University

Dr. Feng Liang is currently a Research Science Specialist at the Aramco Americas (formally Aramco Services Company), Aramco Research Center-Houston. She has now been with the company for almost seven years.

Prior to joining the Aramco Research Center, Feng was a Principal Scientist at Halliburton for nearly eight years. Her research interests are the new materials and product development in fracturing fluid, advanced fluid additives, waterless fracturing technologies, biodegradable diversion materials, sand control products, cement additives, and nanomaterials reinforced elastomers.

Feng is a contributor to many patents and technical papers. She holds over 57 issued U.S. patents and 30 additional published patent applications. Feng is the author and coauthor of more than 70 technical papers, with a few in very high impact factor journals such as the *Journal of the American Chemical Society* and *Nano Letters*. She has also coauthored two book chapters as well. Feng's publications have received over 3,700 citations.

She is a member of the Society of Petroleum Engineers (SPE) and the American Chemical Society (ACS). Feng received the 2017 SPE Production and Operations Award for the Gulf Coast North American Region. She also received the 2017 Effective Publication Award from Saudi Aramco's Exploration and Petroleum Engineering Center – Advanced Research Center (EXPEC ARC).

Feng received her Ph.D. degree in Organic Chemistry from Rice University, Houston, TX.

Adrian Buenrostro

M.S. in Mechanical Engineering, National Autonomous University of Mexico

Adrian Buenrostro is a Senior Petroleum Engineer in the Gas Production Engineering Division of the Southern Area Production Engineering Department of Saudi Aramco. He has 18 years of experience in the oil and gas industry, related to production and completion engineering, management, training and mentoring, sales and marketing, mainly over stimulation duties; experience acquired in Latin America, Europe, and Saudi Arabia.

Adrian is a member of the Society of Petroleum Engineers (SPE) and a certified SPE Engineer. He has written multiple technical articles for international publications and coauthored several more. Adrian regularly works in new technology development; patents and innovation ideas support his contributions, i.e., fracturing with natural sand and the machine learning for stimulation.

He received both his B.S. and M.S. degrees in Mechanical Engineering from the National Autonomous University of Mexico. Adrian received the Mexican National Engineering Medal for his engineering work in 2001.

Conformance Improvement System and Method by Use of Microemulsions

Dr. Victor A. Torrealba, Dr. Hussein Hoteit and Ahmed J. Alabdulghani

Abstract /

The performance of many improved and enhanced oil recovery (EOR) techniques in conventional reservoirs are frequently degraded by conformance problems. The presence of high permeability streaks or thief layers between injection and production wells typically results in premature water breakthrough, high water cut, and deficient volumetric sweep. As a result, significant oil volumes in the reservoir may not be contacted by the injection fluid.

Several conformance improvement techniques, e.g., foams, gels, and resins, have been developed and practiced in improved oil recovery operations. Each technique has its own advantages and limitations related to deployment practicality, effectiveness, and durability.

In this article, a novel conformance improvement method (CIM) was introduced that can be considered practical, effective, and durable. The CIM process consists of cyclical injections of pulse slugs of surfactant alternating with brine. The surfactant slug compositions are selected based on the rheological behavior of the microemulsion phase. The chemical slugs are configured such that the viscosity of the injected fluids is kept low to preserve injectivity and to ensure invasion of the conformance agent toward the thief zones. The trailing brine slugs are designed to produce a high viscosity microemulsion as they mix with the leading surfactant slugs in the reservoir. The proposed process leads to a reduction in the effective mobility of the fluids in the thief layers. As a result, the chase waterflood (WF) would divert into previously uncontacted layers to improve sweep efficiency.

The potential of the proposed CIM in improving oil recovery is demonstrated by various simulations of reservoir cases under WF. Various sensitivities were performed to investigate the effectiveness of the proposed process that include well spacing, permeability contrast, size of the thief layers, heterogeneity, and size of the chemical pulse slugs. Simulations showed that this process is effective in addressing reservoir conformance issues, and therefore, it has the potential to improve sweep efficiency and recovery factor (RF) in the reservoir with distinct thief layers. The treatment surfactant volumes are relatively small, which enables this process to be cost-effective.

Introduction

Oil recovery from a subsurface reservoir is typically expressed as the product of displacement and sweep efficiencies[1]. The first is defined as the ratio of displaced to contacted volumes, while the second is defined as the ratio of contacted to in place volumes. Reservoir conformance is a measure of the volumetric sweep efficiency during oil recovery processes[2].

Conformance problems can be caused by the presence of high permeability streaks, thief layers, faults, or fractures in the reservoir. These geological features act as preferable conduits for the injected fluids, thereby causing significant oil zones in the reservoir to be unflooded.

One of the key gaps in poorly managed improved oil recovery/enhanced oil recovery (EOR) projects is the lack of diagnosis and treatment of the conformance problems[2]. Conformance improvement methods (CIMs) should be low risk and low-cost procedures within the reservoir management workflow that result in a quantifiable increase in oil recovery.

In addition to reservoir heterogeneity, volumetric sweep is typically diminished from the high mobility ratio in the displacement process. For instance, in immiscible gas or waterflooding (WF) of viscous oil reservoirs, the mobility ratio is often significantly larger than one of the receding displaced fluids, i.e., unfavorable mobility, because of the viscosity contrast between the injection fluid and the oil. Such oil displacement conditions may also result in poor conformance[3-6]. In addition to viscosity contrast, relative permeabilities play a similar role is determining the total mobility for each phase[6]. Adequate mobility control can divert the injected fluid to contact a higher percentage of the reservoir pore volume (PV). This work focuses on addressing reservoir conformance issues when reservoir heterogeneity is the primary cause.

Using chemicals for conformance improvement is not a new technology. White et al. (1973)[7] studied the use

of polymers to curb high water cuts in oil producing wells during secondary production. They showed that as the injected viscous polymer solution tended to flow into high permeability zones, the subsequent injected water diverted toward unswept regions of the formation. The authors reported that this process was effective in decreasing the water-oil ratio by 60% to 90% for more than 200 treated producing wells.

Using polymers, however, manifests several limitations related to preserving well injectivity, irreversible permeability reduction from polymer entrapment in rock formation, and the degradation and quality of polymer that is sensitive to the reservoir temperature and concentration of the total dissolved solids in water[8-10]. Particularly, due to the polymer's reduction of fluid mobility, it tends to divert the injected polymer solution into the high permeability regions, which may result in the plugging of both high and low permeability regions, and severely impact the injectivities.

Vadgama and Hinkle (1973)[11] introduced the concept of cross-flooding, whereby sweep efficiency is improved by changing injection well patterns during WF. Field implementation of cross-flooding showed an increase in oil recovery without a significant additional expenditure to the project.

Bernard et al. (1980)[12] studied the use of foam to improve conformance of carbon dioxide (CO_2) flooding. The interaction of a surfactant, CO_2, and water could form foams at reservoir or surface conditions. The presence of foam can significantly increase the overall gas-foam viscosity, therefore, it is used as a near wellbore conformance agent. One advantage of foams over polymers is in the ability to generate foams in situ that helps to overcome well injectivity issues.

Subsequently, similar to polymers, foams exhibit stability issues at reservoir conditions, especially with the presence of oil. There are other challenges in propagating foams away from the wellbore. The use of foam lacks long-term reservoir effectiveness, therefore, the process may need to be frequently repeated. More recently, Singh and Mohanty (2015)[13] studied the use of nanoparticles to stabilize foams. Consequently, the interactions of surfactant and nanoparticles with the subsurface fluids and formations at reservoir conditions are not well understood.

Vinot et al. (1989)[14] studied sodium silicate gels to improve field-scale conformance during WF. At deployment, the solution needs to be of low viscosity when injected, and with sufficient time as the solution propagates in the reservoir, gelation forms and viscosity increases. A key challenge in gel-based conformance improvement applications is in designing and controlling the gelling time. Generally, gel treatments are effective, but they are associated with a risk of damaging the well because of the difficulty in reverting the process if the formed gel does not end up in the intended zones.

Sydansk (1994)[15] and (1994)[16] proposed polymer enhanced foams as a possible bridge between foaming and gelling technologies. Polymer enhanced foams are similar to conventional foams with the addition of a water-soluble polymer to the aqueous phase. This process results in enhanced viscosity and stability of the conformance agent compared to conventional foams, however, this approach inherits the essential limitations of polymers and foams that were previously discussed. Another concern is related to possible component segregation when introducing multiple components of chemicals that may transport at different speeds in the reservoir. For instance, surfactants and polymers have different adsorption and partitioning behaviors, therefore, the overall composition may not remain constant as the fluid propagates away from the wellbore.

Ferris et al. (1996)[17] studied the use of bacteria for conformance control. Bacteria were introduced to precipitate calcium carbonate in high permeability channels. This study was, however, limited to sand packs with single-phase flow. The time scale for mineralization was in the order of 100 PVs of injection, which may render this technology unpractical for reservoir-scale applications, as bacteria have other limitations in high temperature and high salinity reservoirs.

Emulsions, or macroemulsions, are thermodynamically unstable, but kinetically stabilized mixtures of two immiscible fluids, e.g., oil and water. Dispersed phase droplets are considerably large, and typically above 0.1 mm[18, 19]. The size of dispersed phase droplets is inversely proportional to the kinetic energy used in fabricating the macroemulsion[20], but because of thermodynamic instability, the droplets tend to coalesce until phase separation occurs. To slow down the emulsion breakthrough, emulsifiers can be used that help prolong the life of the emulsion.

Bai et al. (2000)[21] also studied the use of crude oil emulsions for use as a selective water shutoff technology describing positive results. Romero et al. (1996)[22] studied the use of heavy oil-in-water emulsions as a plugging material in high permeability sands. They conducted coreflood experiments at 80 °C, with a confining pressure of 3,000 psi and an injection pressure of 1,000 psia. For some cases, they observed the lack of emulsion stability at the inlet, which generated plugging and injectivity loss. One key drawback of emulsion solutions is that oil, as part of the emulsion, is typically injected into the reservoir, which may not be ideal in most cases.

Microemulsions, on the other hand, are thermodynamically stable mixtures of two immiscible fluids. This work proposes to use microemulsion solutions configured with specific surfactant concentrations and salinity as a treatment for reservoir conformance improvement. Microemulsion solutions form from the interaction of surfactant, oil, and brine components[1, 23]. Microemulsions are complex fluids that contain microscopically discontinuous domains of oil and water, separated by a surfactant interfacial layer[24]. Microemulsion phase behavior and rheology have been extensively studied for surfactant EOR[25-30]. Surfactants alone or with combinations of other chemicals are typically used for EOR[1].

The proposed CIM is based on cyclical injection of pulse surfactant slugs of varying salinities. The CIM harnesses the complex rheological behavior of microemulsions to achieve two key requisites for the conformance process: (1) the viscosities of injected solutions are kept relatively low to preserve well injectivity, and (2) the injected solutions, when mixed with the in situ oil in the targeted zones in the reservoir, produce microemulsion solutions with high viscosity.

The objective is to reduce the effective mobility of fluids in the high permeability layers, and thereby enhance the fluid flow diversion within the layered system. The potential of the proposed CIM in improving volumetric sweep efficiency and oil recovery factor (RF) is shown through a series of simulations using an academic chemical EOR simulator. Various sensitivities are explored to understand the effectiveness of the CIM under various reservoir and process conditions.

Methodology

Our proposed CIM consists of injecting surfactant slugs of varying composition and salinity into the injection wells exhibiting conformance issues. The objective is to generate a microemulsion phase in situ with sufficiently high viscosity to reduce the total fluid mobility in the high permeability regions of the reservoir. This treatment can promote flow divergence toward the previously unswept regions of the reservoir.

Different methods, such as crosswell tracers, well testing, and modeling can be used to identify injection and production wells exhibiting conformance issues. This CIM process is intended to be applied to treat injection wells with established WF. In principle, the process could also be applied to treat production wells, however, this scenario has not been investigated in this work.

Figure 1 is a schematic of the CIM treatment procedure applied to water injectors experiencing conformance issues. The CIM treatment consists of the injection of a surfactant slug at a given salinity (X_{CS}) caused by a brine slug at a different salinity (X_{CW}). The injection salinities are selected based on the phase behavior and viscosity of the surfactant-brine-oil system under consideration. The treatment could be repeated for multiple cyclical slugs.

In Fig. 1, X_{W1} and X_{W2} represents the PV injection of water before and after the treatment, respectively. The treatment design in terms of the number of cycles, size of the slugs, surfactant concentrations and salinity gradients can be optimized based on the fluids' phase and viscosity behaviors at field conditions. The success of the CIM process relies on two key conditions:

1. The viscosities of both surfactant and brine slugs are kept sufficiently low to preserve well injectivity. The other benefit is to minimize surfactant invasion of the low permeable zones by maintaining a high mobility flood. With a high mobility flood, the injected chemical slugs would follow the baseline WF flow path, which is essentially through the high permeable streaks. This treatment process overcomes a major drawback in low mobility conformance agents, like gels, that tend to enhance flow diversion next to the wellbore where the conformance agent may divert to the low permeability layers and cause undesired plugging.
2. For a given surfactant concentration, the microemulsion viscosity can be designed by controlling the salinity, Figs. 2 and 3. The salinity of the leading

Fig. 1 *Schematic of the injection schedule used to test the effectiveness of the proposed conformance improvement. After a mature WF has been established, the treatment is deployed, and then WF is resumed.*

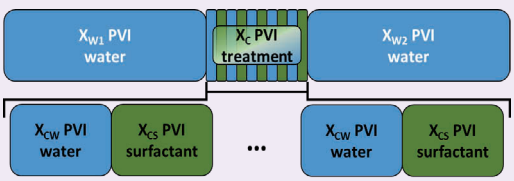

Fig. 2 *Phase behavior data and Hand's model results for a salinity scan. Experimental data from Tagavifar et al. (2017)[30].*

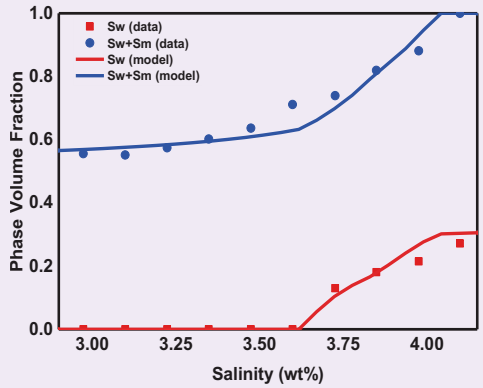

Fig. 3 *Viscosity data and the viscosity model results using both the new viscosity model (Eqn. 1) and the model by Camilleri et al. (1987)[31] for a salinity scan. The experimental data is from Tagavifar et al. (2017)[30]. The water viscosity (X_m = –1) and oil viscosity (X_m = 1) are shown for reference.*

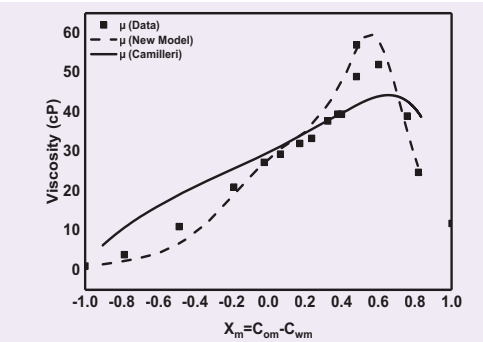

surfactant slug is selected to be outside the peak viscosity region. On the other hand, the salinity of the trailing brine slug is selected to achieve a salinity gradient with the leading slug that encloses the conditions to encounter the peak viscosity.

The objective is to design the salinities of the leading and trailing slugs such that the microemulsion phase with peak viscosity is generated in situ and away from the wellbore. The viscosity of the leading slug (surfactant) is preferred to be higher than that of the trailing slug (brine) to improve conditions for mixing with oil in situ, thereby forming the intended high viscosity microemulsion phase within the high permeable layers.

This approach should not be confused with surfactant flooding for EOR. The objective in chemical EOR is to target the optimum salinity to generate Winsor Type III microemulsion to minimize interfacial tensions (IFT). Here, the target microemulsion phase corresponds to Winsor Type II- or Type II+, but not Type III.

Besides the salinity gradient, the surfactant slug volume is another key design parameter. This work quantifies the surfactant slug volume in terms of the PV of the treated thief layers (PV_{thief}) and the number of cycles considered. The surfactant concentration should stay above the critical micelle concentration before and after dilution with the trailing brine slug. For the cases considered in this article, the volume of the chase brine slugs was selected to be equal to the surfactant slugs, i.e., $X_{CS} = X_{CW}$. The total volume of the conformance treatment is therefore $X_C\ PV_{thief}$, where,

$$X_C = \mathcal{N}(X_{CS} + X_{CW}). \quad (1)$$

In Eqn. 1, $\mathcal{N}$ is the number of cycles. As $\mathcal{N}$ increases, the number of contacts between the leading and trailing slugs increases, which improves the conditions to form high viscosity microemulsions in the thief layer. After the CIM treatment, WF is resumed by injecting X_{W2} PVs of water.

As discussed, it is critical to properly characterize the phase and viscosity behaviors of the fluid system. For instance, Figs. 2 and 3 show the phase behavior and viscosity data from Tagavifar et al. (2017)[30] for a typical brine-oil surfactant system. Hand's model was used to replicate the phase behavior data, Fig. 2. The microemulsion viscosity was modeled as a function of composition and salinity using a microemulsion viscosity model that allows the better capture of viscosity data, including the double peak behavior exhibited by some microemulsion systems using pure alkanes[29].

The two-peak behavior is typically encountered when the microemulsion phase transitions from Type II- to Type II+. The model is able to accurately capture the experimental data for a wide range of salinity, and therefore, microemulsion compositions, improving upon the modeling of the alternative by Camilleri et al. (1987)[31].

The relevant model parameters that were used to match the data are listed in Table 1. Figure 3 shows the viscosity limits for water (1 cP) and oil (11 cP). Those viscosity limits are not typically achieved during a salinity scan for a fixed overall composition.

This work demonstrates the CIM process using the microemulsion data given in Figs. 2 and 3. Our target is to produce in situ the oil-rich microemulsion that corresponds to the viscosity peak, as it appears in Fig. 3. The salinity gradient is selected outside the optimum salinity range to avoid mobilization of the microemulsion phase due to decreasing IFTs. Based on the phase behavior shown in Fig. 2, the microemulsion viscosity is about 58 cP when the salinity is calculated to be at 5 wt% — the reported viscosity data falls outside the salinity range of the phase behavior scan.

In this work, the leading surfactant slug is selected at a higher salinity, 10 wt%, while the trailing brine slug is selected at a lower salinity, 4 wt%. The achieved salinity gradient (4 wt% to 10 wt%) is outside the three-phase region and corresponds to a Type II+ microemulsion environment. The peak viscosity at 5 wt% can be achieved in the reservoir upon in situ mixing of the low and high salinity slugs.

Results

In this section, we present various simulation studies to demonstrate the proposed CIM. We first consider a 1D problem to illustrate the multiphase flow and trapping mechanisms induced by the chemical treatment. We then consider 2D cross-sections where we investigate various sensitivities on a simplified two-layer system, Fig. 4. We then consider more complex channeled systems with high contrast in local heterogeneity. Next, we consider a 10-layer system with two different

Table 1 *The phase behavior and viscosity parameters for the data[30] used in Figs. 2 and 3.*

Phase Behavior Parameters for Hand's Model					
Cs_{m0}	C_{sm1}	Cs_{m2}	CS_{eL} (meq/mL)	CS_{eU} (meq/mL)	
0.06	0.02	0.03	0.65	0.80	
Viscosity Parameters for the New Model					
X_{m1}	X_{m2}	δ_1 (cP)	δ_2 (cP)	α_1	α_2
0.17	0.56	1,300	2,000	5	20

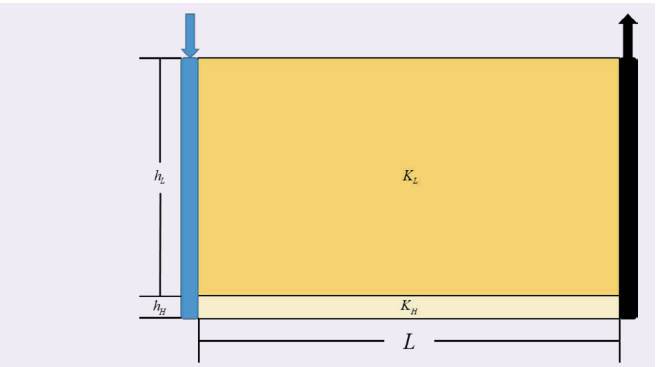

Fig. 4 *A schematic of the reservoir configuration used in our sensitivity study, showing the thickness of the low permeability (KL) layer with thickness (hL) at the top, the high permeability (KH) layer with thickness (hH) at the bottom, and the well spacing (L).*

Dykstra-Parsons coefficients. We also consider a 3D sector case using a real reservoir model. Finally, we consider a grid sensitivity analysis.

For all cases other than the 1D case, we selected a total of five cycles of treatments. We also assumed that the pre- and post-WFs correspond to 1 PV each, i.e., $X_{W1} = X_{W2} = 1$ PV. For all cases, we used a modified version of a chemical flooding simulator[32] with an implementation of a new microemulsion viscosity model. All surfactant slugs were 3% by volume of surfactant at a high salinity of 10 wt%, and the brine slugs were at a lower salinity of 4 wt% based on the rheology and phase behavior of the system under consideration.

Demonstration of Concept

Test Case 1D: We first consider a 1D domain with 100 ft length where the injector is placed at one end and the producer at the other end. The grid block size in this simulation is 1 ft. Additional grid refinements did not change the overall conclusions of this test case. A detailed grid size sensitivity is addressed in the last example.

The 1D domain is initialized with undersaturated oil at saturation, $S_o = 80\%$, and water at its irreducible saturation, $S_w = S_{wirr} = 20\%$. The domain is homogeneous with rock permeability, $K = 500$ mD, and porosity, $f = 25\%$. The other fluid and rock properties are shown in Table 2. Water is injected at a constant rate of 0.1 PV injection/year and the production well is constrained with a minimum bottom-hole pressure (BHP) equal to the initial pressure.

We define a dimensionless effective salinity, C_{SeD}, as the ratio of reservoir effective salinity, C_{Se}, to the injected effective salinity, C_{SeI}. The injection process is described as follows. We first establish a WF baseline at 1 PV injection where water is injected at $C_{SeD} = 1$, that is, the injected water salinity matches the initial salinity in the reservoir. The chemical slug size of 0.05 PV injection and a surfactant concentration of 3 wt% is then injected at $C_{SeD} = 1$. A high salinity water slug of 0.05 PV size is then injected at $C_{SeD} = 2.5$. The surfactant slug/chase-water cycle could be repeated if needed and the slug injection order could be reverted. In this example, only one cycle is injected. Regular WF is then resumed.

Table 2 *The relevant simulation parameters related to reservoir initial conditions, well constraints, relative permeabilities, and capillary desaturation parameters.*

Reservoir Initial Conditions						
P_{res}	S_o	CS_e	*Porosity*			
1,000 psia	$1 - S_{wirr} = 0.8$	2.0 meq/mL	25%			
Well Constraints						
q			P_{prod}			
0.1 PV Injection/Year			1,000 psia			
Relative Permeability						
	Low Capillary Number			**High Capillary Number**		
Phase	S_r	k_j^o	n	S_r	k_j^o	n
Water	0.2	0.9	1.5	0.1	0.5	1.3
Oil	0.3	0.1	1.5	0.1	0.5	1.3
Microemulsion	0.3	0.1	1.5	0.1	0.1	1.3
Capillary Desaturation Parameters						
	Water	Oil	Microemulsion			
	1,865	10,000	364			

This test case is 1D, therefore, it is not suitable to use to study the well conformance issue. The 2D and 3D test cases provided later address the well conformance issue and the flow diversion behavior. We also note that the treatment design, including the chemical slug sizes and the injection order in these examples, may not be optimum. The objective here is to provide a focused analysis of the in situ mixing process and the resulting phase behavior and fluid properties.

The remaining oil saturation in the domain before chemical injection is shown at PV injection = 1, Fig. 5. Figure 5 also shows the oil saturation vs. distance (bottom graph) after the chemical treatment cycle at PV injection = 1.1, 2, and 3. It also shows the microemulsion phase saturation (middle graph), and the corresponding microemulsion viscosity (top graph).

At PV injection = 1.1, a microemulsion phase is developed within a distance of about 20 ft from the injector. The oil saturation corresponding to the microemulsion phase location is zero, which indicates that the microemulsion is a Winsor Type II+. The corresponding microemulsion viscosity (top) is not constant within the microemulsion zone and peaks at about 50 cP. This microemulsion viscosity behavior is related to the salinity concentration and its impact on the microemulsion composition, as will be discussed later.

The increase in microemulsion viscosity results in a low mobility of the microemulsion phase that persists for extended WF, as shown at PV injection = 2 and 3. We also notice that the chemical slug results in the development of an oil bank ahead of the microemulsion leading front (at PV injection = 1.1). This oil bank, however, dissipates and fails to propagate away from the injection zone. The poor mobilization of this Type II+ microemulsion is expected and it serves our intention to induce a low mobility phase to divert flow. This flow divergence mechanism is demonstrated in the 2D and 3D test cases.

The high viscous microemulsion phase is desired to form away from the injector wellbore to avoid injectivity loss. To further analyze the fluid mixing effect on the microemulsion phase behavior in the reservoir, we plot various fluid properties vs. PV injection at two locations in the domain: one near the injector wellbore (at 2 ft) and one away from the injector wellbore (at 20 ft). We first show the fluid mixing behavior away from the wellbore.

Figure 6 shows the overall concentrations (volume fractions) of the oil, brine, and surfactant components (bottom graph). It also shows the aqueous, oleic, and microemulsion phase saturations (middle graph), the dimensionless effective salinity (top left), and the microemulsion viscosity (top right). These fluid properties

Fig. 5 *The oleic phase saturations vs. distance from the injector at PV injection = 1, which corresponds to the remaining oil saturation before the chemical treatment, and at PV injection = 1.1, 2, and 3 are shown on the graph in the bottom. The microemulsion phase saturation (middle), and the corresponding microemulsion viscosity (top) are also shown at PV injection = 1.1, 2, and 3. The locations with zero oleic saturation and non-zero microemulsion saturation correspond to a Type II+ microemulsion phase.*

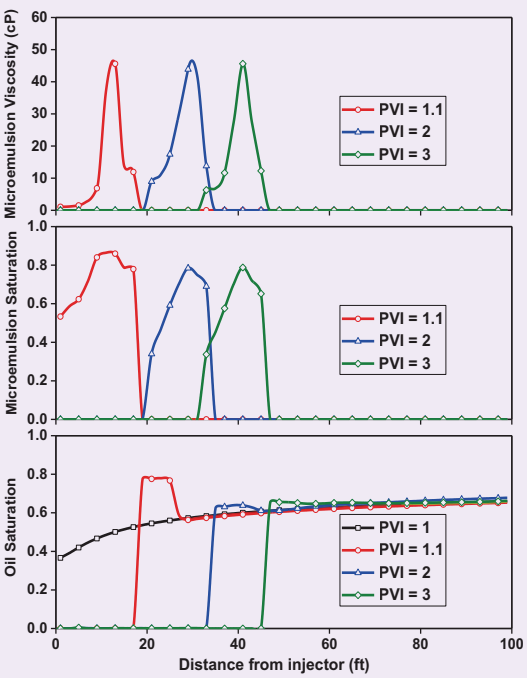

Fig. 6 *The overall concentrations (volume fractions) of the water, oil, and surfactant components are shown vs. PV injection (bottom graph) at a location 20 ft from the injector. Notice that the surfactant concentration is magnified (x10) for visualization purposes. The saturations for the aqueous, oleic, and microemulsion phases are shown in the middle graph. The top graph shows the corresponding microemulsion phase viscosity and the dimensionless effective salinity, C_{seD}. The initial condition of the reservoir (high salinity) corresponds to a Winsor Type II+ environment.*

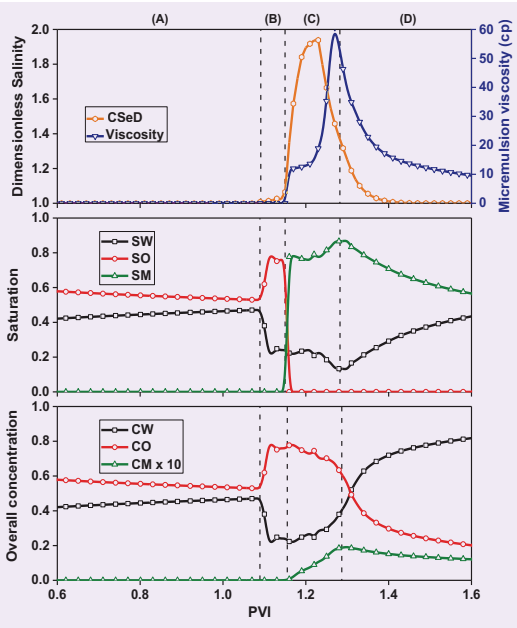

are extracted from a simulation grid block at 20 ft from the injector and plotted vs. PV injection during the time interval, PV injection = 0.6 to 1.6.

Four time regimes, (A), (B), (C), and (D) are distinguished and separated with dashed lines. Time regime (A) occurs during the WF, and therefore, no effect of the chemical slug is observed yet. Oil saturation is decreasing from water displacement, as expected.

In time regime (B), an oil bank displaced downstream of the microemulsion phase shows up before the appearance of the surfactant slug. Note that in time regimes (A) and (B), the saturations and the overall concentrations of oil and water are equivalent, i.e., in the absence of a microemulsion phase the water and oil components are only present in the water and oil phases, respectively.

In time regime (C), however, the accumulation of surfactant concentration (CM plot) results in component separation and in the appearance of a Type II+ microemulsion phase (SM plot). The Type II+ microemulsion appearance corresponds to the disappearance of the oleic phase (SO plot). It also corresponds to a reduction in the aqueous phase saturation (SW plot) as part of the water component partitions into the microemulsion phase.

In time regime (D), surfactant concentration diminishes as well as the salinity. As a result, the microemulsion phase transitions from an oil-rich to a water-rich Type II+ microemulsion. The top graph shows the corresponding microemulsion viscosity and the brine dimensionless effective salinity, C_{SeD}. Notice that the microemulsion viscosity peaks at about 60 cP, which corresponds to a specific salinity and microemulsion composition.

To explain this behavior, we show the microemulsion viscosity and the effective salinity vs. $X_m = C_{om} - C_{wm}$, where C_{om} and C_{wm} are the oil and water volume fractions in the microemulsion phase, respectively. The sign of X_m indicates if the microemulsion phase is oil-rich when positive or water-rich when negative.

Figure 7 (left) displays the dilution path of the microemulsion phase composition, i.e., C_{sm}, C_{om}, and C_{wm}, on a ternary diagram. This dilution path is encountered during different times, i.e., PV injection, at a fixed location, 20 ft from the injector. The change in the microemulsion composition is a result of a change in the overall composition of the oil-water surfactant system and a change in the effective salinity, (right). Figure 7 (right) also shows the microemulsion viscosity vs. the microemulsion content indicator, X_m.

This viscosity behavior is essentially a reproduction of the input viscosity model previously seen in Fig. 3. The peak viscosity is encountered when the salinity C_{SeD} is about 1.4, i.e., $C_{Se} \approx 5.5\%$ and the corresponding X_m is approximately 0.5, indicating an oil-rich Type II+ microemulsion. The provided microemulsion viscosity model also shows that when X_m becomes more negative, the viscosity tends to decrease toward the water-phase viscosity. Therefore, before injecting the high salinity slug to trigger the high viscosity microemulsions, it is

Fig. 7 *The dilution path on the ternary diagram (left) shows the behavior of the microemulsion composition, i.e., C_{sm} (top apex), C_{wm} (left apex), C_{om} (right apex), encountered at 20 ft from the wellbore. The graph on the right shows the microemulsion viscosity and the effective salinity vs. $X_m = C_{om} - C_{wm}$ at the same location (20 ft).*

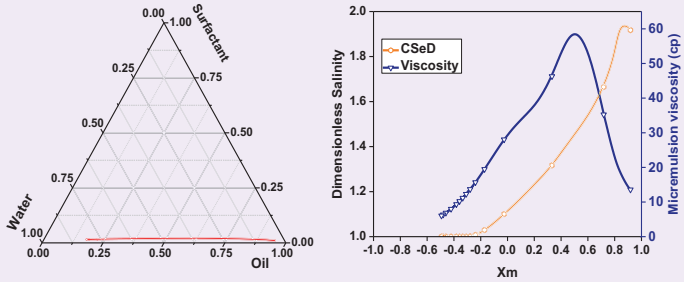

beneficial to displace the oil away from the near wellbore while keeping the salinity low to prevent producing oil-rich microemulsions, i.e., $X_m > 0$ near wellbore.

In our test case, this objective is achieved by injecting the first low salinity surfactant slug that could displace the oil away from the near wellbore with low viscous microemulsions. Figure 8 (left) shows the dilution path of the microemulsion phase composition in the near wellbore (at 2 ft). The microemulsion phase appears to be a water-rich Type II+ microemulsion. Figure 8 (right) shows the salinity and the microemulsion viscosity vs. X_m. The microemulsion phase exhibits low viscosity and the plot shows that the microemulsion phase is displaced away before the high salinity slug takes effect.

We note that the objective of displacing oil from the near wellbore can also be achieved with relatively low viscous Type II- or Type III microemulsions. The objective of developing a high viscous microemulsion away from the wellbore is likely to be achieved using Type II+ microemulsions. Achieving both objectives, i.e., displacing oil from the near wellbore and forming high viscous microemulsion away from the wellbore, is possible with careful design of the surfactant slug

Fig. 8 *The dilution path on the ternary diagram (left) shows the behavior of the microemulsion composition, i.e., C_{sm} (top apex), C_{wm} (left apex), C_{om} (right apex), encountered at 2 ft from the wellbore. The graph on the right shows the microemulsion viscosity and the effective salinity vs. $X_m = C_{om} - C_{wm}$ at the same location (2 ft).*

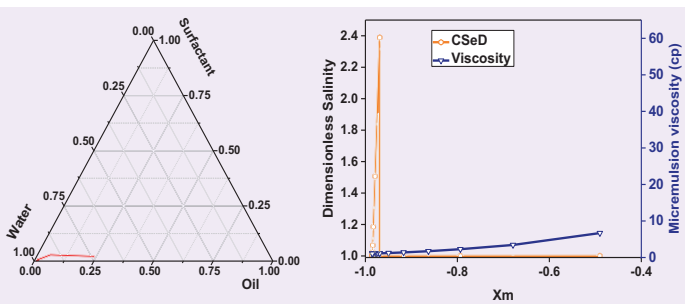

sizes and the salinity gradients.

Test Case 2D: We consider a 2D vertical cross-section with one injector and one producer as shown in Fig. 4. We performed several sensitivities to investigate the CIM performance related to the thief layer size, well spacing, and the permeability contrast. The thief layer size, well spacing, and permeability contrast are parametrized, respectively, by the ratio of the thief layer thickness to the total reservoir thickness, $h_H/(h_H + h_L)$, the aspect ratio, $L/(h_H + h_L)$, and the permeabilities contrast, K_H/K_L. The total thickness of the reservoir is fixed (100 ft).

The reservoir is discretized into a structured grid with grid block dimensions of 20 ft × 2 ft, in the x- and z- directions. Besides the reservoir parameters, we considered varying the total surfactant volume, NX_{CS}, as a percentage of the thief layer's PV. The relevant simulation properties and parameters are listed in Table 2, and the different cases evaluated in our sensitivity study are summarized in Table 3.

To demonstrate the concept in 2D, we first consider a reference case with parameters listed in Table 3. Figure 9 shows the oil saturation distribution maps at the end of the displacement for an extended WF, Fig. 9a, and the CIM process, Fig. 9b. Without the CIM, water mostly channels through the high permeability layer, as expected. With the CIM, the high viscosity microemulsion reduces the conductivity of the high permeability layer, resulting in an improved vertical sweep efficiency of the low permeability layer.

Figures 10a and 10b shows the residual phase saturations for the oil and microemulsion phases at the end of the displacement process, respectively. The plots show that the surfactant solutions preferentially enter the high permeability layer, thereby decreasing IFTs and driving the swept blocks to a high capillary number state.

Figure 11a shows the oil RF and the injection BHP, and Fig. 11b shows the oil cut as a function of PV injection for the cases with CIM and without the CIM (baseline WF). The treatment started after 1 PV injection of WF. For the reference case, the thief layer corresponds to 10% of the total reservoir PV, and the total injected NX_{CS} is 50% of the thief layer's PV. We considered five slug cycles, each leading surfactant cycle, X_{CS}, at 0.01 PV, and the corresponding trailing high salinity water cycle, X_{CW}, also at 0.01 PV.

Simulations showed that the incremental RF from the baseline WF is about 3.5%, which corresponds to about 60% improvement in the oil recovery relative to the baseline case. During the treatment, the injection BHP increased to about 1,500 psia and then declined

Fig. 9 *Oil saturation distribution at the end of the displacement process for an extended WF (a), and the CIM process (b) for the reference case. There is significant diversion of the injection fluid toward the low permeability layer.*

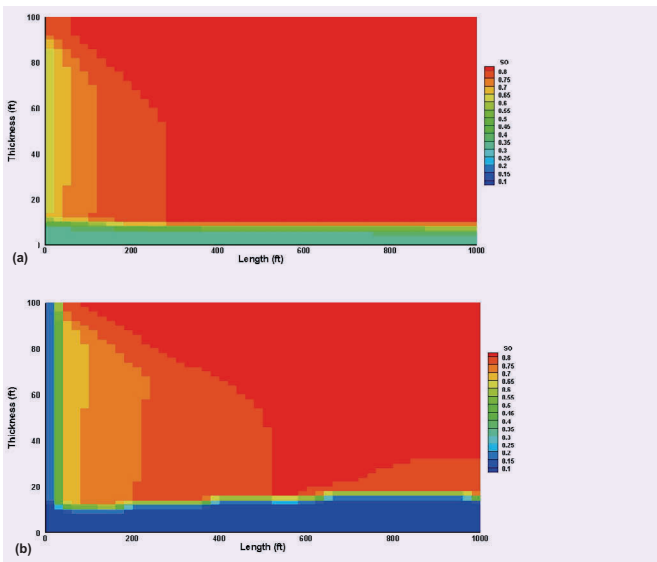

Table 3 *A list of key reservoir and process parameters investigated for the sensitivity analysis considered in Figs. 1 and 4.*

Cases	NX_{CS}	$L/(h_H + h_L)$	$h_H/(h_H + h_L)$	K_H/K_L
Reference Case	50%	10	0.1	50
Case 1: Low NX_{CS}	25%	10	0.1	50
Case 2: High NX_{CS}	75%			
Case 3: Low $L/(h_H + h_L)$	50%	5	0.1	50
Case 4: High $L/(h_H + h_L)$		20		
Case 5: Low $h_H/(h_H + h_L)$	50%	10	0.04	50
Case 6: High $h_H/(h_H + h_L)$			0.5	
Case 7: Low K_H/K_L	50%	10	0.1	10
Case 8: High K_H/K_L				100

and stabilized at about 1,100 psia during the post-WF period. Stabilization of the injection pressure after the treatment above the baseline injection pressure is an indication of the conformance treatment success. The impact of the treatment was also reflected in the oil cut, reaching a peak value of about 60%, compared to about 1% for the baseline WF.

Fig. 10 *The residual phase saturations for the oil (a), and microemulsion (b) phases at the end of the displacement process. The plots show that the residual saturations shift to the high capillary number values in the presence of the surfactant solution, emphasizing the preference of the treatment fluid to penetrate into the thief layer.*

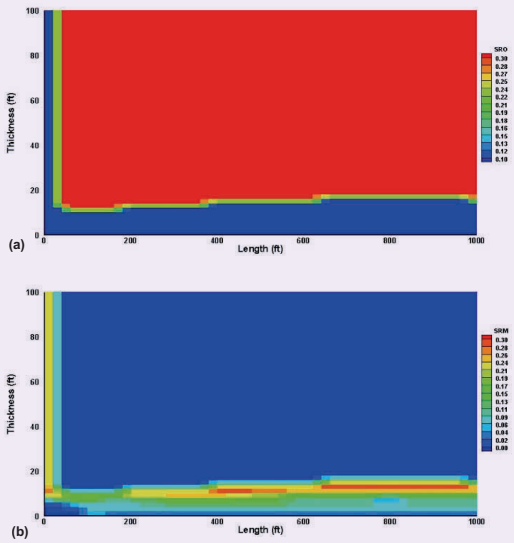

Fig. 11 *(a) The oil RF and injection BHP, and (b) oil cut as a function of PV injection without the CIM (WF) and with the CIM for the reference case.*

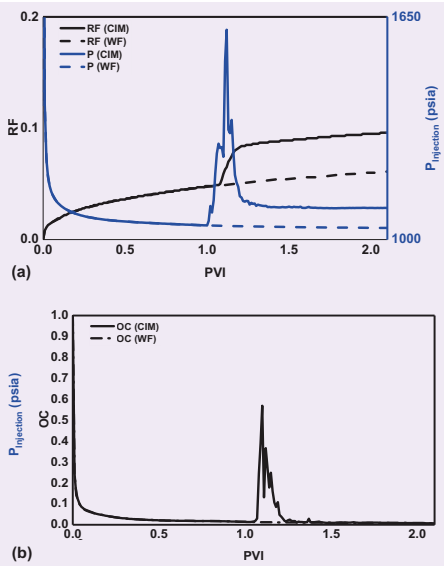

Sensitivity Study

All subsequent cases in our sensitivity analysis address perturbations of one parameter at a time from the reference case, as previously described in Table 3. Figure 12 shows the corresponding RF, and BHP responses vs. PVs injected with and without CIM for all cases in the sensitivity study. Cases 1 and 2 show the impact of the total surfactant injection volume on the ultimate recovery performance. The incremental RF consistently increased from 1.7% of original oil in place (OOIP) for the low injection volume (Case 1 with 25%) to 3.1% for Case 2 with a higher injection volume (75%).

As expected, more NX_{CS} injected translates into higher incremental oil recovery post-treatment. The maximum injection pressure during the treatment was about 1,250 psia for the low volume case and about 1,500 psia for the high volume case. The stabilized incremental pressure compared to the reference case was about 70 psia for the low case and about 60 psia for the high case.

Fig. 12 *The oil RF and injection BHP as a function of PV injection for all cases considered in the sensitivity study and outlined in Table 2. The first row from the top shows the impact of the percentage of the thief layer considered for the total surfactant volume with 25% (left) and 75% (right). The second row shows the impact of the reservoir aspect ratio with 5% (left) and 20% (right). The third row shows the impact of the thief layer size as percentage of the total vertical size of the reservoir with 4% (left) and 50% (right). The fourth row shows the impact of the permeability ratio between the high permeability layer and the low permeability layer with 10% (left) and 100% (right).*

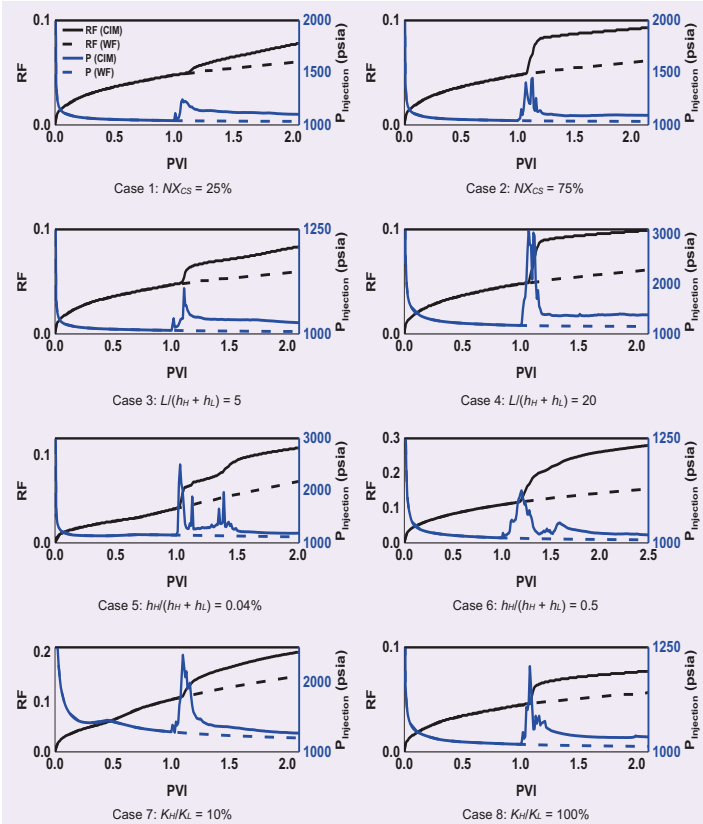

Cases 3 and 4 show the impact of changing the reservoir aspect ratio from 5% to 20%. After 1 PV injection post-treatment, the IRF was 2.4% OOIP for the low case and 3.9% OOIP for the high case. As the aspect ratio increases, there is more interfacial area between the low and high permeability layers, which enhances flow diversion. Furthermore, for the high aspect ratio case, the treatment translated into higher resistance to flow as evidenced by the increased injection BHP. The maximum pressure during the treatment was over 1,100 psia for the low case and over 3,100 psia for the high case. The stabilized value of the incremental pressure after 1 PV injection of water injection post-treatment was over 20 psia for the low case and over 230 psia for the high case.

Cases 5 and 6 show the impact of changing the thickness of the thief layer as a percentage of the total reservoir thickness from 4% to 50%. After 1 PV injection post-treatment, the IRF was 3.8% OOIP for the low case and 12.5% OOIP for the high case. As the thickness increases, there is more oil to be recovered from improving the sweep within the high permeability layer in addition to the oil recovered by diverting the injection fluid to the low permeability layer. The maximum pressure during the treatment was about 2,500 psia for the low case and over 1,120 psia for the high case. The stabilized value of the incremental pressure after 1 PV injection of water injection post-treatment was over 70 psia for the low case and over 10 psia for the high case.

Finally, Cases 7 and 8 show the impact of permeability contrast as it changes from 10% to 100%. After 1 PV injection post-treatment, the IRF was 4.8% OOIP for the low case and 2.0% OOIP for the high case. As the permeability contrast decreases, it is easier to divert the injection fluids into the low permeability layer. The maximum pressure during the treatment was about 2,400 psia for the low case and over 1,200 psia for the high case. The stabilized value of the incremental pressure after 1 PV injection of water injection post-treatment was approximately 70 psia for the low case and over 20 psia for the high case.

For the surfactant system and set of parameters evaluated, the cases of the high aspect ratio (large well spacing), small thief layer thickness, and low permeability contrast yielded pressures that may be too high in the presence of injection pressure constraints, e.g., formation fracture pressure or maximum pump pressure. For such cases, we could either consider a treatment based on the Type II- environment — lower salinities — that will result is lower microemulsion viscosity or a different surfactant system with lower microemulsion viscosity peaks.

Impact of Local Heterogeneity

In this example, we consider a vertical cross-section extracted from the upper Ness formation provided in the 10th SPE comparative solution[32]. This model is highly channeled and characterized by contrasting geological features. Figure 13 shows the selected 2D cross-section, and the corresponding permeability map. In this model, the thief zones correspond to about 50% of the total reservoir PV. Similar to the previous simulation cases, we considered five slug cycles where each X_{CS} is 0.05 PV of the thief layer. As discussed previously, the treatment volume is a design parameter and the NX_{CS} considered here are not meant to be optimal.

Figure 14a shows the oil RF, injection BHP, and Fig. 14b the oil cut as a function of PV injection for the case with CIM treatment compared to the baseline WF case. After 1 PV injection post-treatment, the incremental RF was 16.1% OOIP, the maximum pressure during the treatment was over 3,700 psia, and the stabilized incremental pressure after 1 PV injection of water injection post-treatment was over 290 psia. This case demonstrates the potential of our proposed technique in the presence of local heterogeneity within the thief layer. The oil cut results show the clear benefit of the

Fig. 13 *The permeability distribution for a vertical layer of the upper Ness formation. Permeability data from Christie and Blunt (2001)[32].*

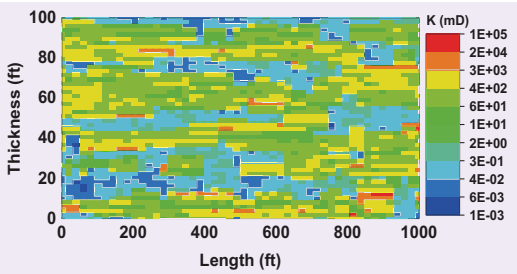

Fig. 14 *(a) The oil RF, injection BHP, and (b) oil cut as a function of PV injection without the CIM (WF) and with the CIM for the Ness case.*

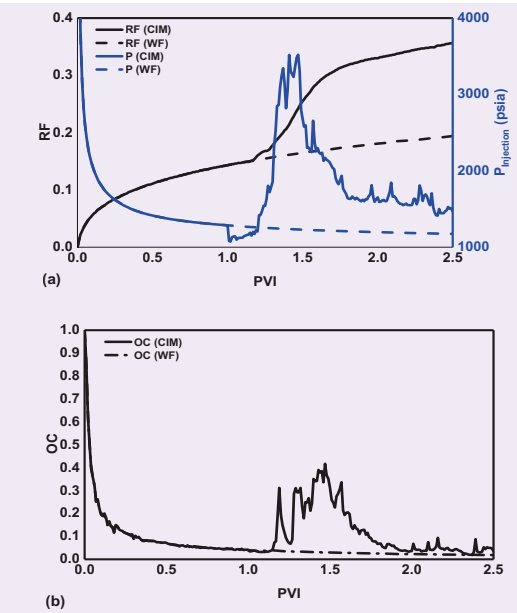

treatment, reaching a peak value of approximately 42%, compared to about 3% for the baseline WF.

Figure 15 shows the oil concentration distribution maps at the end of the displacement for the baseline WF case, Fig. 15a, and for the CIM case, Fig. 15b. The displacement process without the CIM has a relatively low sweep efficiency within the high permeability regions, compared to the CIM process where significant flow diversion is observed.

Figure 16a shows the permeability distribution, with an increased contrast between the high and low permeability zones. Figure 16b shows the viscosity distribution of the trapped microemulsion phase at the end of the displacement. Comparing these two maps shows that the treatment is effective in forming a lasting high viscosity microemulsion in the high permeability regions of the reservoir.

Fig. 15 *(a) The oil distribution at the end of the displacement for the baseline WF case, and (b) with the CIM for the Ness case.*

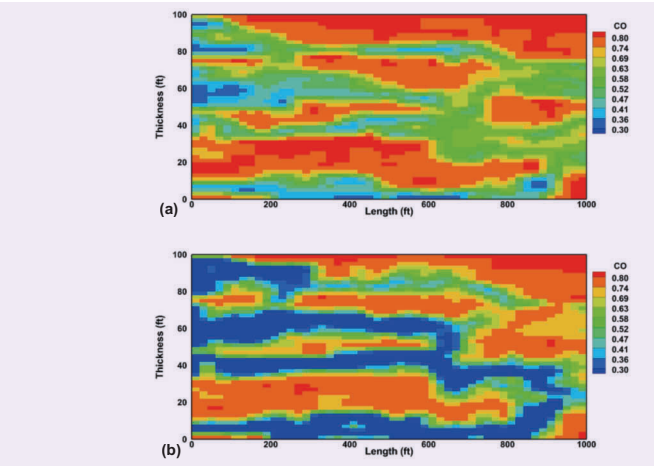

Fig. 16 *(a) The permeability distribution showing the contrast between low and high permeability regions, and (b) the microemulsion viscosity distribution at the end of the displacement, i.e., 1 PV injection of water after the treatment.*

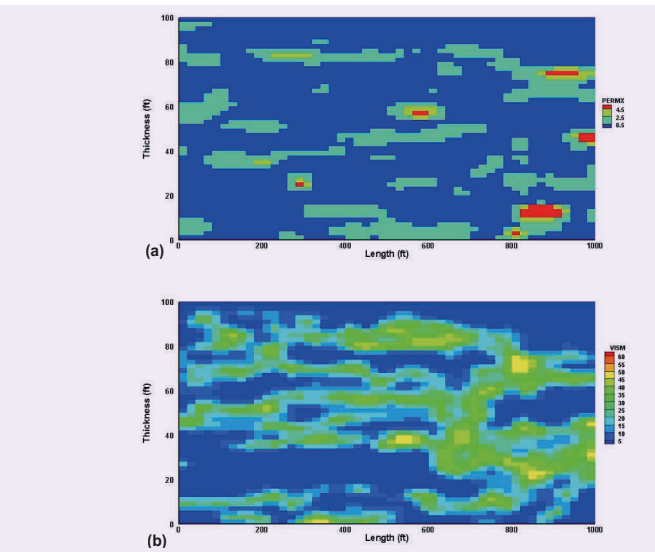

Impact of Vertical Heterogeneity in Multilayered Systems

In this last case, we consider the sensitivity in vertical heterogeneity as measured by the Dykstra-Parsons coefficient, V_{DP}, for two 10-layer systems. The CIM treatment corresponds to the reference case previously described in Table 3. Each layer has the same thickness, and the corresponding permeabilities are shown in Figs. 17a and 17b for the low V_{DP} = 0.86 and high V_{DP} = 0.96, respectively. For both cases, there are three thief layers and the remaining are low permeable zones. The low V_{DP} case is constructed based on the high V_{DP} case, but only modifying layers 8 and 9 (from top to bottom). For both cases, the thief layers correspond to 30% of the total reservoir PV, and the total injected NX_{CS} is 50% of the thief layers.

Figures 18a and 18b show the oil RF, and injection BHP as a function of PV injection for the cases with low and high Dykstra-Parsons coefficients, respectively. After 1 PV injection post-treatment, the incremental RF was 7.6% OOIP for the low case and 8.0% OOIP for the high case. The maximum pressure during the treatment was about 1,180 psia for the low case and over 1,190 psia for the high case.

Figures 19a and 19b shows the oil concentration maps at the end of the displacement for the low V_{DP} with and without the CIM treatment, respectively. Figures 19c and 19d shows the oil concentration maps at the end

Fig. 17 *The permeability distribution for a 10-layer reservoir with Dykstra-Parsons coefficient (V_{DP}) of 0.86 (a) and 0.96 (b). For both cases, the thief layers are the third, seventh, and 10th from the top, and the only changes are in the eighth and ninth layer.*

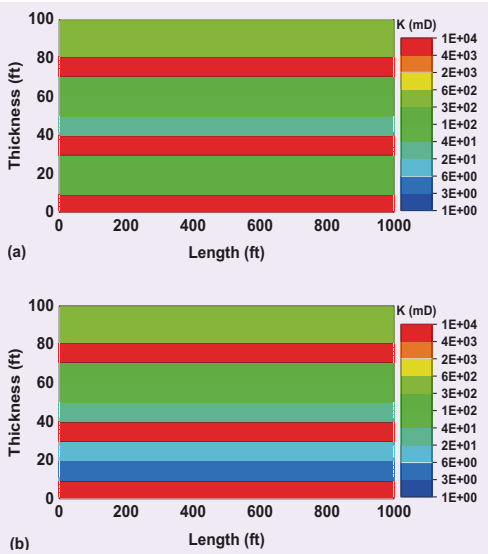

Fig. 18 *The oil RF and injection BHP as a function of PV injection without the CIM (WF) and with the CIM for the case of V_{DP} = 0.86 (a) and V_{DP} = 0.96 (b).*

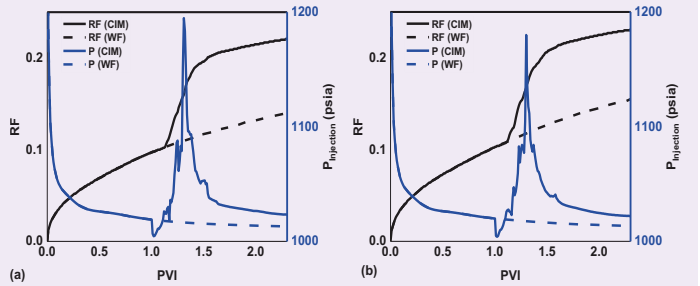

Fig. 19 *The oil distribution at the end of the displacement process for the baseline and CIM cases with V_{DP} = 0.86 and V_{DP} = 0.96.*

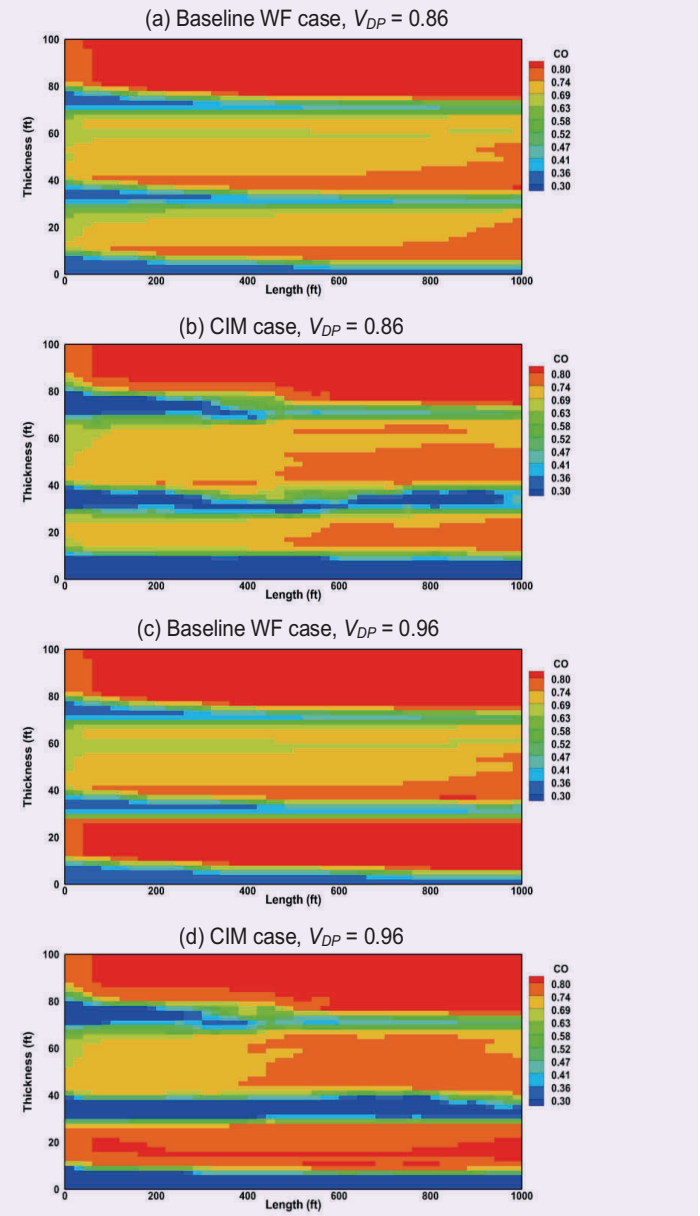

of the displacement for the high V_{DP} with and without the CIM treatment, respectively. Without the CIM, the injected water mostly channels through the three thief layers, while with the CIM, additional sweep can be observed as a result of enhanced flow diversion to the low permeability layers.

Conclusions

In this article, we introduced a novel CIM based on the injection of cyclical surfactant slug solutions. The concept is to treat wells with conformance issues with one or multiple cycles of relatively low viscous surfactant slugs to form a high viscous microemulsion phase that would divert flow toward the unswept low permeable zones.

The method relies on the behavior of the microemulsion phase as a function of the phase composition and effective salinity. There are two key steps involved in the treatment process. In the first step, a low salinity surfactant slug forming a low viscous microemulsion phase is used to displace oil away from the near wellbore to prevent injectivity loss. A chase slug using high salinity water is then injected to induce a high viscous microemulsion phase.

We presented several test cases using simulations to highlight the key flow mechanisms and fluid phase behavior involved in the conformance treatment. We further studied a series of sensitivities accounting for volume of the injected surfactant slug, well spacing, size of the thief layers, permeability contrast, layer heterogeneity, number of layers, vertical heterogeneity, and grid block size. We also demonstrated the concept on a 3D field application. Below are some key results:

- Simulations showed that the proposed CIM treatment is possible by carefully designing the surfactant slugs and the salinity gradients.
- The CIM was found to be effective in improving RF and sweep efficiency from low permeability zones for all cases considered.
- The success of the treatment is a result of the formation of high viscosity microemulsions in the high permeability zones, which induced flow diversion into the low permeability zones.
- For all cases considered, the increased reservoir resistance was maintained long after switching to WF, which is an indicator for the durability of the conformance treatment.
- We presented a new microemulsion viscosity model that improves on the modeling of viscosity data to more accurately describe the microemulsion-based conformance treatment.
- The grid size effect should be examined carefully to improve the reliability of simulations. The grid sensitivity study in this work showed that the grid block size should be within a 10 ft to 20 ft range, and models with coarser grids may not be reliable.
- Laboratory experiments will be required to further validate the proposed methodology.

Nomenclature

Roman

C = Volumetric composition, dimensionless
CS_e = Effective salinity, meq/mL
h = Reservoir height, ft
k = Relative permeability, dimensionless
K = Permeability, mD
L = Reservoir length (inter-well spacing), ft
n = Corey exponent, dimensionless
$\mathcal{N}$ = Number of cycles, unitless
P = Pressure, psia
q = Injection rate, PV injection/year
S = Phase saturation, dimensionless
V_{DP} = Dykstra-Parsons coefficient, dimensionless
X = PVs injected of the treatment fluid
X = Composition variable, dimensionless

Greek

α = Exponent coefficient in viscosity model, dimensionless
δ = Scaling coefficient in viscosity model, cP
μ = Phase viscosity, cP

Subscripts

C = Conformance
D = Dimensionless
i = i^{th} component
I = Injection condition
j = j^{th} phase
m = Microemulsion phase
M = Surfactant component
o = Oil component or phase
s = surfactant component
S = Surfactant injection
w = Water component or phase
W = Waterflood
0 = Low salinity condition
1 = First viscosity peak (i.e., water-rich peak)
1 = Optimum salinity condition
2 = Second viscosity peak (i.e., oil-rich peak)
2 = High salinity condition

Superscript

o = End point

References

1. Lake, L.W., Johns, R., Rossen, B. and Pope, G.: *Fundamentals of Enhanced Oil Recovery*, Society of Petroleum Engineers, 2014, 496 p.
2. Sydansk, R.D. and Romero-Zerón, L.: *Reservoir Conformance Improvement*, Society of Petroleum Engineers, 2010, 138 p.
3. Gaucher, D.H. and Lindley, D.C.: "Waterflood Performance in a Stratified, Five-Spot Reservoir — A Scaled-Model Study," *AIME Petroleum Transactions*, Vol. 219, Issue 1, December 1960, pp. 208-215.
4. Gogarty, W.B.: "Mobility Control with Polymer Solutions," *Society of Petroleum Engineers Journal*, Vol. 7, Issue 2, June 1967, pp. 161-173.
5. Lee, K.S. and Claridge, E.L.: "Areal Sweep Efficiency of Pseudoplastic Fluids in a Five-Spot Hele-Shaw Model," *Society of Petroleum Engineers Journal*, Vol. 8, Issue 1, March 1968, pp. 52-62.
6. Gogarty, W.B., Meabon, H.P. and Milton Jr., H.W.: "Mobility Control Design for Miscible-Type Waterfloods Using Micellar Solutions," *Journal of Petroleum Technology*, Vol. 22, Issue 2, February 1970, pp. 141-147.
7. White, J.L., Goddard, J.E. and Phillips, H.M.: "Use of Polymers to Control Water Production in Oil Wells," *Journal of Petroleum Technology*, Vol. 25, Issue 2, February 1973, pp. 143-150.
8. Zhang, G. and Seright, R.S.: "Conformance and Mobility Control: Foams versus Polymers," SPE paper 105907, presented at the International Symposium on Oil Field Chemistry, Houston, Texas, February 28-March 2, 2007.
9. Hoteit, H., Alexis, D., Adepoju, O.O., Chawathe, A., et al.: "Numerical and Experimental Investigation of Polymer-Induced Resistance to Flow in Reservoirs Undergoing a Chemical Flood," SPE paper 181720, presented at the SPE Annual Technical Conference and Exhibition, Dubai, UAE, September 26-28, 2016.
10. Clifford, P.J. and Sorbie, K.S.: "The Effects of Chemical Degradation on Polymer Flooding," SPE paper 13586, presented at the SPE Oil Field and Geothermal Chemistry Symposium, Phoenix, Arizona, March 9-11, 1985.
11. Vadgama, U.N. and Hinkle, B.B.: "Cross-Flooding to Improve Waterflood Efficiency in Big Sinking Field, Kentucky," *Journal of Petroleum Technology*, Vol. 25, Issue 9, September 1973, pp. 1021-1024.
12. Bernard, G.C., Holm, L.W. and Harvey, C.P.: "Use of Surfactant to Reduce CO_2 Mobility in Oil Displacement," *Society of Petroleum Engineers Journal*, Vol. 20, Issue 4, August 1980, pp. 281-292.
13. Singh, R. and Mohanty, K.K.: "Synergy between Nanoparticles and Surfactants in Stabilizing Foams for Oil Recovery," *Energy and Fuels*, Vol. 29, Issue 2, 2015, pp. 467-479.
14. Vinot, B., Schechter, R.S. and Lake, L.W.: "Formation of Water-Soluble Silicate Gels by the Hydrolysis of a Diester of Dicarboxylic Acid Solublized as Microemulsions," *SPE Reservoir Engineering*, Vol. 4, Issue 3, August 1989, pp. 391-397.
15. Sydansk, R.D.: "Polymer-Enhanced Foams Part 2: Propagation through High Permeability Sandpacks," *SPE Advanced Technology Series*, Vol. 2, Issue 2, April 1994, pp. 160-166.
16. Sydansk, R.D.: "Polymer-Enhanced Foams Part 1: Laboratory Development and Evaluation," *SPE Advanced Technology Series*, Vol. 2, Issue 2, April 1994, pp. 150-159.

17. Ferris, F.G., Stehmeier, L.G., Kantzas, A. and Mourits, F.M.: "Bacteriogenic Mineral Plugging," *Journal of Canadian Petroleum Technology*, Vol. 35, Issue 8, August 1996, pp. 56-61.

18. Zhai, X. and Efrima, S.: "Chemical and Physical Aspects of Macroemulsions Stabilized by Interfacial Colloids," *The Journal of Physical Chemistry*, Vol. 100, Issue 26, 1996, pp. 11019-11028.

19. Wennerstrom, H., Soderman, O., Olsson, U. and Lindman, B.: "Macroemulsions vs. Microemulsions," *Colloids and Surfaces A: Physicochemical and Engineering Aspects*, Vols. 123-124, May 1997, pp. 13-26.

20. Gupta, A., Narsimhan, V., Hatton, T.A. and Doyle, P.S.: "Kinetics of the Change in Droplet Size during Nanoemulsion Formation," *Langmuir*, Vol. 32, Issue 44, 2016, pp. 11551-11559.

21. Bai, B., Han, M., Li, Y., Wei, M., et al.: "Selective Water Shutoff Technology Study and Application of W/O Emulsions," SPE paper 59320, presented at the SPE/DOE Improved Oil Recovery Symposium, Tulsa, Oklahoma, April 3-5, 2000.

22. Romero, L., Ziritt, J.L., Marin, A., Rojas, F., et al.: "Plugging of High Permeability — Fractured Zones Using Emulsions," SPE paper 35461, presented at the SPE/DOE Improved Oil Recovery Symposium, Tulsa, Oklahoma, April 21-24, 1996.

23. Winsor, P.A.: *Solvent Properties of Amphiphilic Compounds*, Butterworths Scientific Publications, London, 1954, 207 p.

24. Strey, R.: "Microemulsion Microstructure and Interfacial Curvature," *Colloid and Polymer Science*, Vol. 272, Issue 8, 1994, pp. 1005-1019.

25. Khorsandi, S. and Johns, R.T.: "Robust Flash Calculation Algorithm for Microemulsion Phase Behavior," *Journal of Surfactants and Detergents*, Vol. 19, Issue 6, September 2016, pp. 1273-1287.

26. Torrealba, V.A. and Johns, R.T.: "Coupled Interfacial Tension and Phase Behavior Model Based on Micellar Curvatures," *Langmuir*, Vol. 33, Issue 47, 2017, pp. 13604-13614.

27. Acosta, E., Szekeres, E., Sabatini, D.A. and Harwell, J.H.: "Net Average Curvature Model for Solubilization and Supersolubilization in Surfactant Microemulsions," *Langmuir*, Vol. 19, Issue 1, 2003, pp. 186-195.

28. Labrid, J.C.: "Oil Displacement Mechanisms by Winsor's Type I Micellar Systems," SPE paper 8325, presented at the SPE Annual Technical Conference and Exhibition, Las Vegas, Nevada, September 23-26, 1979.

29. Bennett, K.E., Davis, H.T., Macosko, C.W. and Scriven, L.E.: "Microemulsion Rheology: Newtonian and non-Newtonian Regimes," SPE paper 10061, presented at the SPE Annual Technical Conference and Exhibition, San Antonio, Texas, October 4-7, 1981.

30. Tagavifar, M., Herath, S., Weerasooriya, U.P., Sepehrnoori, K., et al.: "Measurement of Microemulsion Viscosity and Its Implications for Chemical Enhanced Oil Recovery," *SPE Journal*, Vol. 23, Issue 1, February 2018, pp. 66-83.

31. Camilleri, D., Fil, A., Pope, G.A., Rouse, B.A., et al.: "Improvements in Physical-Property Models Used in Micellar/Polymer Flooding," *SPE Reservoir Engineering*, Vol. 2, Issue 4, November 1987, pp. 433-440.

32. Christie, M.A. and Blunt, M.J.: "Tenth SPE Comparative Solution Project: A Comparison of Upscaling Techniques," *SPE Reservoir Evaluation and Engineering*, Vol. 4, Issue 4, August 2001, pp. 308-317.

33. UTCHEM-9.0 Chemical Flooding Research Simulator (Computer software developed by the University of Texas at Austin, Texas), 2000.

About the Authors

Dr. Victor A. Torrealba

Ph.D. in Petroleum Engineering, King Abdullah University of Science and Technology

Dr. Victor A. Torrealba is a Postdoctoral Fellow at the King Abdullah University of Science and Technology, Thuwal, Saudi Arabia. His focus is on modeling, simulation, and experiments probing relevant mechanisms for improved oil recovery/enhanced oil recovery (IOR/EOR) processes.

Victor's research interest includes IOR/EOR using gas and chemical technologies.

He received B.S. degree (Honors), and his M.S. and Ph.D. degrees from Pennsylvania State University, College Station, PA, all in Petroleum Engineering.

Dr. Hussein Hoteit

Ph.D. in Applied Mathematics, University of Rennes 1

Dr. Hussein Hoteit is an Associate Professor in Reservoir Engineering and the Program Chair of Energy Resources and Petroleum Engineering (ERPE) at King Abdullah University of Science and Technology (KAUST), Thuwal, Saudi Arabia.

Before joining KAUST, Hussein worked for ConocoPhillips and Chevron Companies for about 12 years, where he conducted projects related to chemical enhanced oil recovery (EOR), CO_2 EOR, steam flood, EM heating, to name a few.

Hussein's current research includes chemical EOR, geological CO_2 storage, improved oil recovery optimization, data-driven machine learning, and reservoir simulation development.

He has earned several Society of Petroleum Engineers (SPE) awards, including SPE Distinguished Lecturer in 2009, and served as Associate Editor for the *SPE Journal* for more than 10 years.

Hussein received his B.S. degree in Pure Mathematics and Computer Sciences from Lebanese University, Lebanon, M.S. and Ph.D. degrees in Applied Mathematics from the University of Rennes 1, Rennes, France.

Ahmed J. Alabdulghani

M.S. in Petroleum Engineering, King Abdullah University of Science and Technology

Ahmed J. Alabdulghani is Production Engineer working in the Ras Tanura Production Engineering Division of Saudi Aramco's Northern Area Production Engineering Department. He started his career as a Production Engineer working in Manifa Field. Ahmed became involved in rigless interventions, electric submersible pump design and installation, multiphase flow meter calibration, and well testing.

Throughout his career, Ahmed has worked in several assignments, including the production and reservoir management system (Manara), the water adaptive inflow control device (W-AICD), and the development of downhole equipment to enhance the coiled tubing intervention reach.

He is currently a candidate in the Production Engineering Specialist Program (PESP) in Well Completion and Wellhead Equipment.

Ahmed completed Saudi Aramco's College Degree Program for Non-Employees. He then received a scholarship to study for his B.S. degree in Petroleum Engineering at the University of Manchester in the U.K., graduating in 2010. In 2019, Ahmed received his M.S. degree Petroleum Engineering from King Abdullah University of Science and Technology.

Automatic Carbonate Rock Facies Identification with Deep Learning

Sonali Pattnaik, Dr. Songhua Chen, Dr. Adly Helba, and Dr. Shouxiang M. Ma

Abstract /

Linking depositional properties and post-depositional diagenetic modifications of a rock with its petrophysical attributes remains a great challenge for carbonate rock characterization, formation evaluation, and petrophysical rock typing. Generally, characterization of carbonate rock facies is labor intensive, which requires an experienced geologist to interpret and integrate core, petrographic thin sections, and borehole image logs.

In this approach, the carbonate lithofacies are identified with an emphasis on the diagenetic features, such as grain packing, micritization, cementation, and dolomitization, as well as diagenetic/karstic dissolution, and related connected or partial connected interparticle pores, intra-particle pores, separate and oversized vugs, and micrite microporosity, etc. Here, we focused on developing a deep learning based technique for automatizing the manual facies identification process, a powerful tool to provide consistent and faster turnaround interpretations of geological facies for applications such as petrophysical parameter prediction.

In this article, an architecture for unsupervised multiclass semantic segmentation of carbonate facies that incorporates deep U-Net based architecture is presented. The advantages of using such a network comes from adding skip connections, which allows for a better flow of information in the network. This in return ensures comparable performances along with better feature representation for semantic segmentation tasks. Although many machine learning techniques have been previously applied for facies image analysis automation, the foundation is always the effectiveness of segmentation of multiple overlapping objects in the image. In case of carbonate rocks, diagenesis amplifies the heterogeneity complication. Therefore, to deal with this heterogeneity of carbonates we focused on unsupervised approaches because supervised learning methods can become very impractical due to the daunting task of manual feature labeling.

Multiple experiments were conducted on representative images of three types of carbonate facies (grainstone, rudstone, and packstone) to evaluate the performance of our segmentation algorithm and provide quantitative metrics useful for geological and petrophysical applications. Additionally, the segmentation algorithm is also used to detect primary resistive features from resistivity-based borehole images. The consistent segmentation results have proved both the effectiveness and validity of the algorithm.

Introduction

Lithofacies Family (LFF) and Lithofacies Type (LFT)

Rock facies identification and classification using cores, thin sections, and image logs are the most important methods for reservoir characterization. Generally, under the lithofacies classification scheme, the carbonate lithofacies family (LFF) from mudstone to rudstone and dolostone can be further classified into lithofacies types (LFTs) and sublithofacies types (SLFTs) relying on depositional and diagenetic properties, Fig. 1.

- The families of LFFs are distinguished primarily based on the depositional fabric that is reflected by the relative abundance of grains vs. mud matrix.
- The LFTs are differentiated on the basis of depositional texture, structures, and allochem types.
- The SLFTs are ranked based on the impact of diagenetic alterations and the nature of pore systems.

Therefore, effective semantic segmentation focused on resolving and identifying key parameters such as rock allochems vs. matrix/cements, separate/connected vugs vs. interparticle/micropores. In addition, other diagenetic features are crucial to characterization of carbonate facies.

Automation of Rock Facies Characterization

The families of LFF classification can be considered as a semantic segmentation or a pixel level classification problem. The main objective is to create machine learning models that systematically interprets facies constituents from thin sections, and image logs by standardizing descriptions and reducing subjectivity while

Fig. 1 *LFFs and LFTs[1, 2].*

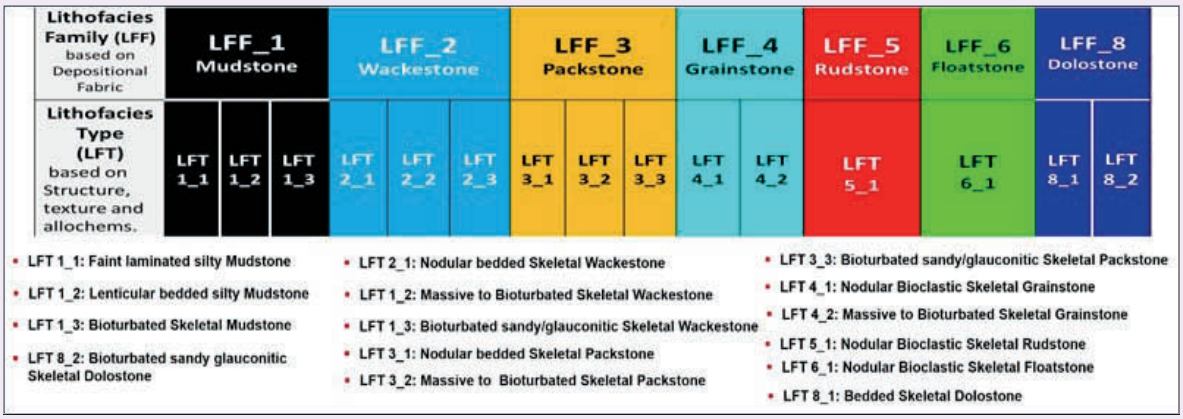

handling large data sets.

Several attempts based on supervised machine learning, computer vision and statistical analysis have been made for effective thin section segmentation and image log interpretation. Jobe et al. (2018)[3] presented methods based on advanced image analysis and machine learning for geological feature prediction from thin section images. The first approach uses pore geometry as features to train four machine learning models for reservoir zone prediction. The second approach uses convolutional neural networks (CNNs) to recognize Dunham's rock fabric classes (grainstone, packstone, wackestone, and mudstone) from thin section images[1].

Abedini et al. (2018)[4] proposed two intelligent machine learning models based on shallow learning and deep learning for identification of the porosity types from thin sections. Machine learning methods based on artificial neural networks and random forest classifiers have proven to be efficient and effective for mineralogy and porosity identification from petrographic thin sections of carbonate rocks[5]. Gupta et al. (2019)[6] used deep neural networks to automatize prediction of geological features from borehole images with minimal manual intervention. Lima et al. (2019)[7] proposed an unsupervised neural network model for borehole image data clustering that helped in facies pattern recognition.

With the advent of fully CNNs[8], end-to-end deep learning pipelines can be built for performing semantic segmentation of large image data sets. Pattnaik et al. (2020)[9] presented clustering techniques and stacked U-Net based architecture for unsupervised carbonate thin section segmentation. Inspired by the success of U-Net[10] and Deep ResUnet[11], we propose a modified stacked U-Net based framework for semantic segmentation of carbonate facies. The proposed pipeline has been tested and evaluated on the three most important families of LFFs — grainstone, rudstone, and packstone — that are common to many carbonate reservoirs and is easily extendable to other rock types as well.

The advantage of using such a network comes from adding skip connections between layers, which alleviates the problem of vanishing gradient and allows better information flow between low and high levels of the network. This in return ensures better performance for facies semantic segmentation tasks resolving and identifying overlapping petrographic constituents like cements vs. grains, intra- vs. inter-particular pores, and other diagenesis features.

The rest of the article is organized according to the following workflow.

- First, we introduce semantic segmentation, the machine learning challenges for petrographic and borehole resistivity images of carbonate facies, and describe how we tackle them.
- Then, we present our methodology to automate the precise location; areal coverage and labeling of the constituent petrographic elements in an unsupervised manner for the studied three carbonate families. The segmentation results for thin sections are used to determine grain size distribution for the entire image database to draw comparative conclusions between the carbonate types.
- Finally, we demonstrate that the developed segmentation method automatically picks up high and low resistive patterns from the borehole image logs.

Semantic Segmentation

Semantic segmentation for carbonate petrographic images and borehole image logs is a process of partitioning and labeling the image into geologically meaningful regions. Subsequently, the high heterogeneity of most carbonate rocks inherited from a complex paragenesis of depositional and diagenetic processes makes pattern recognition and labeling a daunting task. This necessitates an automated workflow that can alleviate manual efforts for performing petrographical analysis for large image data sets and also encourages cross team collaborations by building a single classification scheme.

The present work strives to handle the following

challenges generally faced while performing machine learning for semantic segmentation of microscopic and borehole images.

1. Due to common heterogeneities in most carbonates, Fig. 2, improper pixel-wise labeling by applying supervised segmentation can make a machine learning algorithm learn inconsistent patterns. Even if we apply supervised learning, the pixel-wise labeling will be subjective to interpretations of individual subject matter experts and results may not always be consistent. This limitation is mitigated by conducting unsupervised pattern recognition for the entire image data set.
2. Discrete sensors and pads from typical borehole imaging tools leave gaps between adjacent pads, in which the formation are not sensed, resulting in multiple gaps on the image log display. In this case, we use a deep learning method for borehole image gap infilling.
3. It is often difficult to obtain a huge training database to cover the great variation of heterogeneities to train machine learning models. We overcome this with data augmentation by image cropping, rotation of images, light variation, etc.
4. Data from multiple wells may adequately represent most families of LFFs with different characteristics. The developed model can act as a starting point or as pre-trained weights for other wells; so that we do not have to train everything from scratch each time.

Methodology

A successful segmentation for carbonates must address a key question: How can the networks learn the heterogeneity and complexity of carbonates to output a high spatial resolution segmentation map that is capable of segmenting small objects and delineating sharp boundaries? U-Net is a popular architecture for supervised image segmentation due to its high performance, easy trainability, and adaptability on small data sets. It has an encoder-decoder type of architecture, which captures the context information at multiple scales.

Figure 3 shows the contracting path, or the encoder, which applies max pooling operations to encode the input into feature representations at multiple levels. The expansive path, or the decoder, uses several upsampling operations to semantically project the low resolution representation learned by the encoder onto high resolution. However, the main drawback of using U-Net for carbonate facies segmentation is lacking of supervised data. To fully exploit the utility of U-Net in handling the complex carbonate heterogeneities and ensure it still produces superior segmentation results, a new stacked U-Net architecture-based pipeline is used.

Network Architecture

Xia and Kulis (2017)[12] proposed a stacked U-Net architecture by concatenating two U-Net modules by using two loss functions. The first U-Net module, Fig. 4, takes the thin section images as the input and generates the segmentation map of the images. The first module uses a differentiable soft normalized cut-loss function, which is variant of a normalized cut[13].

The second module takes the segmented output of the first module as the input and reconstructs the original input images of the same dimension. The second loss function is the reconstruction loss, which is a least squares error function between the original inputs and reconstructed outputs. The stacked U-Net architecture leverages the use of two U-Nets in handling the heterogeneity and complexity of carbonate features, because the iterative combination of the two loss functions helps balance the trade-off between the accuracy of reconstructed output and the consistency in the learning complex patterns for the segmented output.

The main disadvantage of stacked U-Net architecture is that the losses do not change significantly after a certain number of iterations, and the network might be trapped in a suboptimal solution[14]. To increase the information flow between the two U-Nets and prevent degradation of gradients, skip connections are added to connect both U-Nets. This prevents the saturation of the loss function after certain iterations and improves performance.

Fig. 2 *Carbonate heterogeneities due to various allochem types and composition, depositional fabric and texture, diagenetic alterations, and related pore system.*

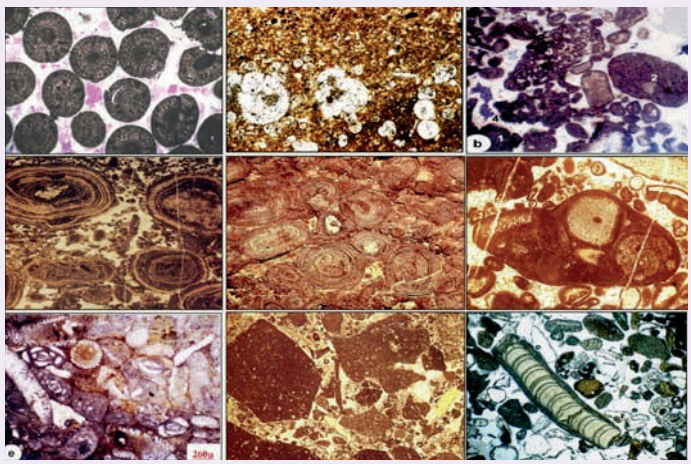

Fig. 3 *The U-Net architecture for image segmentation. Note that the U-Net has a contracting path and an expanding path that gives it a "U" like structure.*

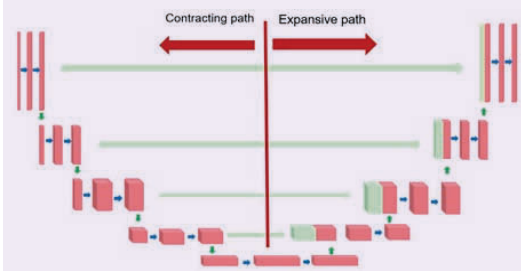

Fig. 4 *The stacked U-Net architecture for unsupervised image segmentation after adding skip connections.*

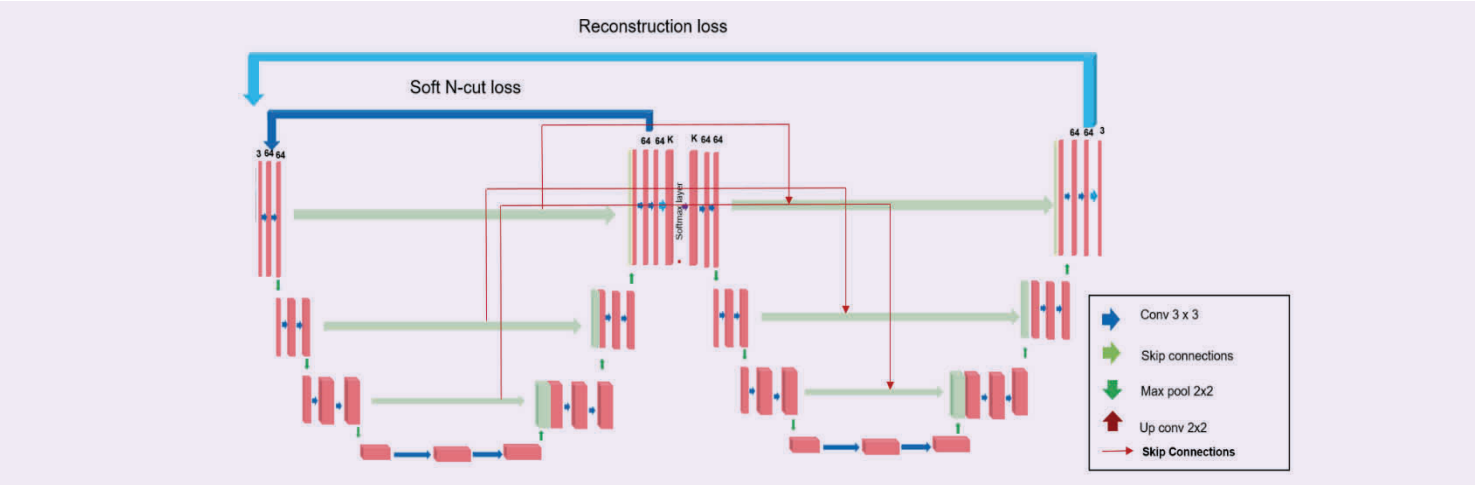

Petrographic Image Data Acquisition and Data Augmentation

The number of studied thin section images for grainstone, rudstone, and packstone are 114, 34, and 89, respectively. Each image is 1,400 × 900 pixels in size. The stacked U-Net architecture as previously described is an unsupervised, complex, and deeper neural network. To achieve superior performances and ease the training process, we can either use pre-trained network weights and then fine-tune it to our target data set or use extensive data augmentation.

Subsequently, as the pre-trained weights are not available in this study, we augmented our data sets by brightness adjustment, rotation, and random cropping. This data augmentation also makes the process more robust and less prone to overfitting.

Training

The proposed model was implemented using Tensorflow and optimized through the Adam optimization algorithm[15]. Theoretically, the network can take arbitrary size images as input as we fully use CNNs, however, it will need large graphic processing unit memory to store the model weights. Therefore, we resize images to 200 × 200 pixels to train the model.

A total of 30,000 input samples are generated. We trained the model with a mini batch size of three images on a NVIDIA P100 graphic processing unit with an initial learning rate of 10^{-4}, which was subsequently reduced by a factor of 0.3 after every 1,000 iterations. The network was finally converged after 25,000 iterations.

Output Refinement and Post-Processing

Due to zero padding in the convolutional layers, the output pixel values near the boundaries of the image have lower accuracy. Therefore, when we crop the images, we use an overlap strategy to produce better results. The final step is to merge segments appropriately to form the final image segments using hierarchical segmentation, which is a bottom-up greedy approach[16]. Figure 5 shows the segmentations results.

Application Example 1: Characterization of Grain Size Distribution

To demonstrate applications of the methodology previously described, the grains are subsequently segmented to better understand the grain size distribution, Fig. 6, for the three types of carbonates by performing further statistical calculations[17].

Grainstones are grain supported carbonate rocks with little mud content and most of their grain size (diameter) is less than 2,000 μm, Fig. 6a. Rudstones are grain supported carbonate facies that have at least 10% of the grain sizes larger than 2,000 μm, Fig. 6b.

Fig. 5 *Stacked U-Net segmentation results for families of LFFs: grainstone, rudstone, and packstone. Left: Original image. Middle: Machine learning prediction. Right: Final segmentation map after postprocess.*

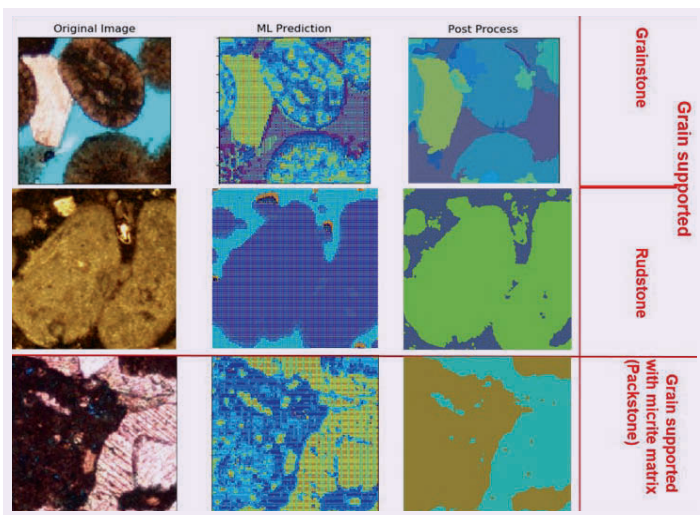

Fig. 6 *Predicted grain size distribution: (a) grainstones, (b) rudstones, and (c) packstones.*

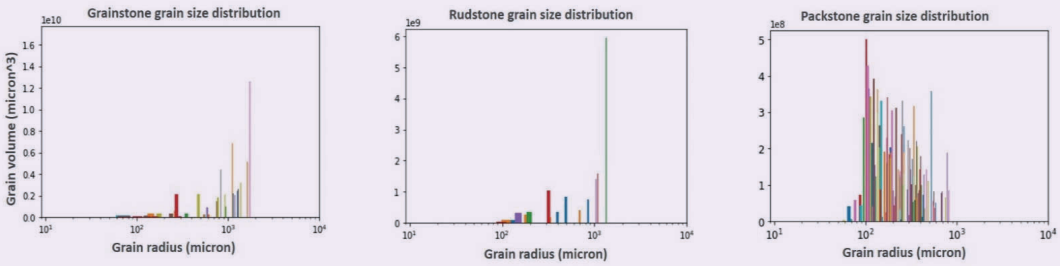

Packstones are grains supported with particle sizes that are less than 2,000 μm. In this case, the grain sizes vary mostly between 50 μm to 700 μm, Fig. 6c.

Application Example 2: Interpretation of Borehole Image Logs

Borehole resistivity images are useful to help better understand the distribution of resistivity values in surrounding rock formations under drilling conditions and are used in reservoir characterization such as structural dip determination, fractures, micro-fault characterization, facies analysis, stratigraphic studies, and petrophysical analysis, etc.

The model developed for unsupervised segmentation is versatile enough that it can be extended to detect primary features for facies pattern recognition and formation characterization using borehole images. The goal is to lay the groundwork for building an automated workflow for carbonate facies classification and identification using core images, thin sections, and borehole image logs.

Data Pre-Processing

The studied resistivity image data set are water-based mud borehole image logs with high borehole coverage and are mostly logged across the carbonate formations. They are constructed from high-resolution resistivity measurements made by pad-mounted arrays of electrodes. In this arrangement of pad-mounted electrodes, the coverage area depends on the distribution of the electrode arrays in relation to the borehole circumference. Images rendered from these resistivity imager tools include inevitable gaps represented by vertical-slanted white/gray stripes, Fig. 7, whenever the borehole circumference exceeds the total width of the mounted electrode pads.

Usually, geologists are skilled at inferring this missing information, and they will generally succeed in interpretation of continuous sinusoidal features — dipping planar boundaries intersecting a well. Consequently, faults, fractures, partial sinusoids, and other more complex patterns present a challenge, and interpretation may be subjective.

Equally important is the fact that filling the borehole gaps on image logs will act as a starting point for automated feature analysis for borehole images using machine learning and the gaps are an impediment to this process as they will mislead machine learning to recognize spurious patterns. In this study, a deep learning method for borehole gap infilling was used to build continuous logs, Fig. 7.

Training

We trained the stacked U-Net on the image log data sets consisting of 10,000 dynamic images. Each image is resized to 200 × 200 pixels like the thin section process, however, due to the use of the full CNNs, images of any size will work. To increase the prediction accuracy and ensure that each part of the borehole is well represented in the training samples, we use the overlap strategy while building the training samples with at least a 20% overlap. We divide the data set into 80% training and 20% test data sets.

Results

For simplicity of presenting the output of the machine learning experiments, we show the original borehole image on the left (high resistivity) and the segmented output on the right (low resistivity) for two examples, Fig. 8. By convention, low-resistivity features, such as

Fig. 7 *Left track: Original borehole image. Right track: Full borehole image after using the deep learning method for gap infilling.*

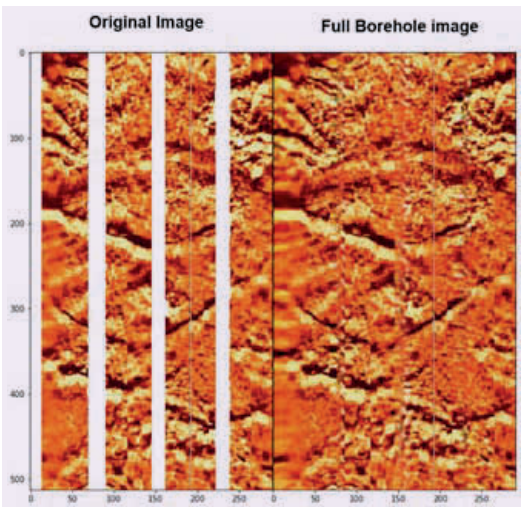

Fig. 8 *Stacked U-Net segmentation results for high and low resistivity features for borehole images.*

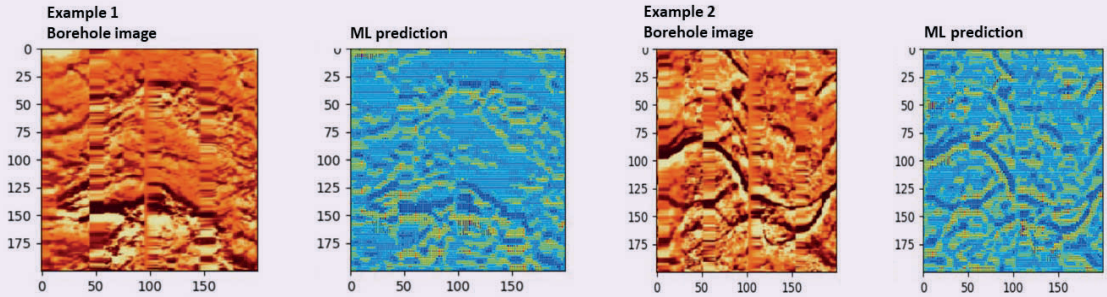

shales or conductive mud filled fractures, are displayed as dark colors. High-resistivity features, such as quartz or calcite cemented nodules or bands in sandstones and tightly cemented carbonates, are displayed as shades of yellow and white.

The high and the low resistive patterns have been picked up by the model automatically and enables recognition of similarities. This will serve as the features set for further facies classification.

Conclusions

From the work presented in this article, the following points are concluded.

- We demonstrated thin section segmentation results for all three families of carbonate LFF; grainstones, rudstones, and packstones, using improved stacked U-Nets.
- Adding skip connections in the stacked U-Nets facilitated information propagation between both U-Nets. This not only helps in improving the training performance but also allows us to build deeper networks for unsupervised segmentation. Even though carbonate facies have a strong diagenetic overprint and have widely varying grain sizes and mud content, this method was able to resolve the consistency challenges by building a faster way to segment the thin section images.
- The model was also able to detect primary features for facies pattern recognition and formation characterization using borehole images.
- This method is versatile, and will help build a workflow for the classification and identification of carbonate facies by tying core images and thin sections with image logs.

Acknowledgments

This article has taken inspiration from the articles presented at the SPWLA Saudi Arabia Chapter and the DGS Topical Workshop on Linking Geological Facies and Petrophysical Rock Types, on November 28, 2017.

The authors would also like to thank Mahmoud Eid of Halliburton for his assistance during the project.

This article was prepared for presentation at the SPE Annual Technical Conference and Exhibition, virtual, October 27-29, 2020.

References

1. Dunham, R.J.: "Classification of Carbonate Rocks According to Depositional Texture," in Ham, W.E. (ed.), *Classification of Carbonate Rocks*, American Association of Petroleum Geologists Memoir 1, 1962, pp. 108-121.
2. Embry, A.F. and Klovan, J.E.: "A Late Devonian Reef Tract on Northeastern Banks, Island, N.W.T.," *Bulletin of Canadian Petroleum Geology*, Vol. 19, Issue 4, December 1971, pp. 730-781.
3. Jobe, T.D., Vital-Brazil, E. and Khait, M.: "Geological Feature Prediction Using Image-Based Machine Learning," *Petrophysics*, Vol. 59, Issue 6, December 2018, pp. 750-760.
4. Abedini, M., Ziaii, M., Negahdarzadeh, Y. and Ghiasi-Freez, J.: "Porosity Classification from Thin Sections Using Image Analysis and Neural Networks Including Shallow and Deep Learning in Jahrum Formation," *Journal of Mining and Environment*, Vol. 9, Issue 2, 2018, pp. 513-525.
5. Rubo, R.A., de Carvalho Carneiro, C., Michelon, M.F. and dos Santos Gioria, R.: "Digital Petrography: Mineralogy and Porosity Identification Using Machine Learning Algorithms in Petrographic Thin Section Images," *Journal of Petroleum Science and Engineering*, Vol. 183, December 2019, p. 106382.
6. Gupta, K.D., Vallega, V., Maniar, H., Marza, P., et al.: "A Deep-Learning Approach for Borehole Image Interpretation," paper presented at the SPWLA 60th Annual Logging Symposium, The Woodlands, Texas, June 15-19, 2019.
7. Lima, L., Bize-Forest, N., Evsukoff, A. and Leonhardt, R.: "Unsupervised Deep Learning for Facies Pattern Recognition on Borehole Images," OTC paper 29726, presented at the Offshore Technology Conference Brasil, Rio de Janeiro, Brazil, October 29-31, 2019.
8. Long, J., Shelhamer, E. and Darrell, T.: "Fully Convolutional Networks for Semantic Segmentation," in *Proceedings of the IEEE Conference on Computer Vision and Pattern Recognition*, 2015, pp. 3431-3440.
9. Pattnaik, S., Chen, S., Shao, W. and Helba, A.: "Automating Microfacies Analysis of Petrographic Images," paper presented at the SPWLA 61st Annual Logging Symposium, Virtual Online Webinar, June 24-July 29, 2020.
10. Ronneberger, O., Fischer, P. and Brox, T.: "U-Net: Convolutional Networks for Biomedical Image Segmentation," in Navab, N., Hornegger, J., Wells, W. and Frangi, A. (eds.) *Medical Image Computing and Computer-Assisted Intervention*,

Lecture Notes in Computer Science, Vol. 9351, Springer, 2015, pp. 234-241.

11. Zhang, Z., Liu, Q. and Wang, Y.: "Road Extraction by Deep Residual U-net," *IEEE Geoscience and Remote Sensing Letters*, Vol. 15, Issue 5, May 2018, pp. 749-753.
12. Xia, X. and Kulis, B.: "W-Net: A Deep Model for Fully Unsupervised Image Segmentation," arXiv preprint arXiv:1711.08506, November 2017.
13. Shi, J. and Malik, J.: "Normalized Cuts and Image Segmentation," *IEEE Transactions on Pattern Analysis and Machine Intelligence*, Vol. 22, Issue 8, August 2000, pp. 888-905.
14. Chen, W., Zhang, Y., He, J., Qiao, Y., et al.: "Prostate Segmentation Using 2D Bridged U-net," paper presented at the International Joint Conference on Neural Networks, Budapest, Hungary, July 14-19, 2019.
15. Kingma, D.P. and Ba, J.L.: "Adam: A Method for Stochastic Optimization," paper presented at the International Conference on Learning Representations, Banff, Alberta, Canada, April 14-16, 2014.
16. Arbelaez, P., Maire, M., Fowlkes, C. and Malik, J.: "Contour Detection and Hierarchical Image Segmentation," *IEEE Transactions on Pattern Analysis and Machine Intelligence*, Vol. 33, Issue 5, 2011, pp. 898-916.
17. Beucher, S.: "The Watershed Transformation Applied to Image Segmentation," *Scanning Microscopy*, Supplement, January 1992, pp. 299-325.

About the Authors

Sonali Pattnaik

M.S. in Applied Mathematics, University of Washington

Sonali Pattnaik is a Senior Scientist in Physics working in Halliburton's Technology Center. She joined Halliburton in 2018, and has since worked on multiple important projects within the Wireline Product service line.

In Sonali's current role at Halliburton, her research efforts are based on creating fast and efficient machine learning, data science, and deep learning solutions using cutting-edge technologies. The application domains that Sonali focuses on are petrophysics, carbonate reservoirs, wireline cased hole, etc. She has already submitted four patent applications as the first inventor in less than two years of her career.

Sonali received her B.S. degree in Exploration Geophysics from the Indian Institute of Technology, Kharagpur, India. She received her M.S. degree in Applied Mathematics from the University of Washington, Seattle, WA. Sonali holds a second M.S. degree in Computational Geophysics from Colorado School of Mines, Golden, CO.

Dr. Songhua Chen

Ph.D. in Physics, University of Utah

Dr. Songhua Chen is currently the Senior Manager of Nuclear Magnetic Resonance (NMR) Sensor Physics Discipline at Halliburton. Since joining Halliburton 8 years ago, he has been leading a team of scientists and mathematicians to research and design new wireline XMR and LWD MRIL sensors, as well as to optimize NMR data acquisition, processing, and interpretation methodologies.

Most recently, Songhua's interest focuses on carbonate pore typing, unconventional reservoir fluid identification, and applying data analytic approaches in petrophysical interpretation. In the last several years, he has also been closely collaborating with colleagues in Saudi Aramco's RDD on a number of applied research projects to advance carbonate formation evaluation technologies, core analysis methods, and machine learning and deep learning applications.

Prior to joining Halliburton, Songhua was with Baker Hughes for 15 years as a staff Scientist and NMR Interpretation Project Leader, and later became Senior Manager of the Integrated Interpretation Group to develop technologies involving NMR, geochemistry, fluid sampling/testing interpretations, and pore scale modeling. Prior to working in the energy service industry, he was a Senior Scientist at Texas A&M University, College Station, TX.

Songhua is an inventor or co-inventor of 70 U.S. patents in NMR downhole sensors, data processing and analytics, inversion, core analysis, and integrated petrophysics. He is the author or coauthor of numerous publications, including book chapters, peer-reviewed journal papers, and conference proceedings.

Songhua has been an active member of the Society of Petroleum Engineers (SPE), the Society of Petrophysicists and Well Log Analysts (SPWLA), and a past member of the American Physical Society, the Society of Exploration Geophysicists (SEG), and the Society of Core Analysts (SCA). He has co-chaired two SPWLA NMR topical conferences and served once on SPWLA's Technology committee. Songhua was selected twice as the SPWLA Distinguished Speaker in 2006 and 2013, respectively, and in 2019 was the recipient of SPWLA's Distinguished Technical Achievement Award.

He received his B.S. degree in Physics from Southeast University, Nanjing, China, and his Ph.D. degree in Physics from the University of Utah, Salt Lake City, UT.

Dr. Adly Helba

Ph.D. in Clastics Sedimentology, Cairo University

Dr. Adly Helba is a Senior Geoscience Advisor at Halliburton, since 2009. Currently based in Saudi Arabia, he leads a geoscience team in analysis and geological interpretation of resistivity images in both single and multiwell projects within the MENA region.

Before joining Halliburton, Adly was a staff member (Assistant Professor) in the Geology Department in Cairo University and a consultant in Bapetco, Oil Search, Norec, and Schlumberger companies.

In 1981, he received his B.S. degree in Geology from Cairo University, Giza, Egypt. Adly received his M.S. degree in Carbonate Sedimentology in 1987, and his Ph.D. degree in Clastics Sedimentology from Cairo University in 1991.

Dr. Shouxiang M. Ma

Ph.D. in Petroleum Engineering, New Mexico Institute of Mining and Technology

Dr. Shouxiang M. "Mark" Ma is a Senior Consultant overseeing research and development, subject matter technical support, and professional development in the Advanced Petrophysical Modeling Group of Saudi Aramco's Reservoir Description and Simulation Department. Prior to this, he was Supervisor of the Petrophysical Support & Study Unit, advisor at the Upstream Professional Development Center, and Lead Petrophysicist for logging operations.

Before joining Saudi Aramco in 2000, Mark worked at the Exxon Production Research Company, Wyoming Western Research Institute, New Mexico Petroleum Recovery Research Center, and China Yangtze University.

He served as a chairperson of the 2013 Society of Petroleum Engineers (SPE) Formation Evaluation Award Committee, the 2018 SPE Annual Technical Conference and Exhibition Formation Evaluation Committee, and the 2019 International Petroleum Technology Conference Education Week.

Mark was awarded the 2019 SPE MENA Formation Evaluation Award and the SPE International Distinguished Member Award in 2020.

He currently serves on the *JPT* Editorial Board and the Society of Petrophysicists and Well Log Analysts (SPWLA) Board of Directors for the Middle East and Africa area. Mark is also an Associate Editor for the *Journal of Petrophysics*, and Vice President of the SPWLA Saudi Arabia Chapter.

He received his B.S. degree from the China University of Petroleum, Shandong, China, and his M.S. and Ph.D. degrees from the New Mexico Institute of Mining and Technology, Socorro, NM, all in Petroleum Engineering.

The Effects of Crude Oil Gravity and Composition on EOR Surfactants Selection and Performance

Amer M. Alanazi, Dr. Abdulkarim M. Al-Sofi, Ziyad F. Kaidar, and Dr. Khaled Abdelgawad

Abstract /

Surfactant applicability for enhanced oil recovery (EOR) is conventionally characterized by their efficiency in reducing oil-water interfacial tension (IFT). A suitable surfactant for one crude oil might not be suitable for another in terms of lowering the IFT. Therefore, formulations should be revisited for particular cases, especially with changes in crude oil API gravity. In this work, we investigate the performance of various EOR surfactants and their behaviors with different crude oil samples from Super Light to Extra Heavy.

EOR surfactants of different classes showed a suitable compatibility in high salinity brines and at high temperatures. The gravities of tested crude oil samples ranged from 8° to 37° API. Crude oil properties were validated using a viscometer and a density meter. The experimental work focused on IFT measurements and critical micelle concentrations (CMC). IFTs were measured using a spinning drop tensiometer at a fixed concentration and the CMCs were determined using a Du Noüy ring-type tensiometer.

CMCs of the amphoteric and nano-encapsulated ionic surfactants were found to be very low compared to that of cationic and nonionic surfactants. Both amphoteric and nano-encapsulated ionic surfactants demonstrated superior results across all benchtop studies. They have exhibited a better temperature stability with low- and high-salinity brines. Both showed low IFT values of approximately 0.02 mN/m for Light crude oil. Those IFT values remained the lowest compared to other surfactants with heavier crude oil samples, but gradually increased to 0.18 mN/m for the heaviest crude oil. In terms of IFT equilibration, the amphoteric and nano-encapsulated ionic surfactants resulted in IFT values that gradually increased with the increase of oil viscosity. This was quite opposite for the cationic quaternary ammonium and anionic alfa olefin sulfonate surfactants. The different behavior of surfactants with crude oils of varying compositions indicate the distinctive reaction of each surfactant with a specific crude oil.

The results highlight the effects of crude oil gravity and composition on the surfactant's ability to result in a low IFT. Coupled with CMC measurements at elevated temperatures, a good insight can be established for evaluating the performance and potential of a surfactant for EOR application.

Introduction

Enhanced oil recovery (EOR) applications have a significant potential to maximize oil recovery. Typically, oil is either trapped because of capillary forces or bypassed, due to unfavorable well placement or reservoir characteristics. Chemical injection is one of the EOR techniques that is used to recover oil beyond the conventional methods. Chemical EOR mostly relies on surfactants and polymers. Polymers address sweep and bypassing by improving the mobility ratio. Surfactants achieve ultra-low interfacial tension (IFT), and possibly alter rock wettability, to mobilize the trapped oil.

Surfactants are defined as organic amphiphilic compounds used to reduce the IFT between two immiscible fluids and are frequently used as detergents, wetting agents, emulsifiers, foaming agents, and dispersants. Any surfactant contains two parts: the hydrophilic (water-soluble) and the hydrophobic (water insoluble). The hydrophilic end acts as a head while the other lipophilic end acts as a tail. The amphiphilic nature of surfactants allows the surfactants to adsorb at the interfaces between oil and water, thereby lowering both the IFT between the oil and water phases.

Surfactants are classified by the type of head to anionic (negative charge head), nonionic (neutral head), cationic (positive charge head), and zwitterionic (negative/positive charge). In addition to surfactants, short chain aliphatic alcohols are used as co-solvents. Although most of the co-solvents increase the IFT by decreasing solubilization ratios, they favorably reduce the microemulsion viscosity and the time required for microemulsions to reach an equilibrium state[1-2]. Co-solvents can also enhance the aqueous phase chemical stability by increasing the solubility of the surfactant in brine[3]. Surfactants detach oil drops by lowering IFT between the oil and water phase to ultra-low values, which results in capillary numbers large enough to overcome capillary

forces and mobilize oil[4].

An efficient chemical EOR requires the presence of adequate amounts of surfactant molecules at the oil and water interface. Surfactants are injected above the critical micelle concentration (CMC) that is defined as the concentration at which surfactant molecules start to form aggregates into micelles[5]. The aggregation process occurs due to the interaction energy of the electrostatic and hydrophobic process inside the system. This aggregation effect causes the loss of surfactant molecules at the interface.

The design of a suitable surfactant formulation can be challenging for specific reservoir conditions. Surfactants in the EOR process are very sensitive to reservoir conditions such as salinity, temperature, and pH. A few of the early studies performed at harsh reservoir conditions indicated that conventional surfactants are not suitable for such conditions. This, in turn, has led recent efforts to develop new technologies, chemicals, and formulations, including bio- and nano-surfactants[6-7].

The performance of surfactants similar to other co-injected chemicals in EOR varies based on the gravity and composition of the crude oil. This is particularly important when applying chemical EOR in heavy crude reservoirs[8]. The crude oil composition can greatly control the design of the chemical EOR process, as it imposes a huge impact on the IFT. An analysis of the oil components — acidic, aromatic, and asphaltene content — is a prerequisite for the selection of the optimum surfactant to emulsify the oil and produce a middle-phase microemulsion between injected water and the oil[9, 10].

The microemulsion phase is a thermodynamically stable mixture of the aqueous (water and co-solvent), oleic (oil and co-solvent), and interfacially active (surfactant and co-solvent) pseudo components[11]. For heavy oil, synergism is required; using a single surfactant cannot reduce IFT to ultra-low values[12, 13]. The higher the asphaltene percentage in the heavy oil, the higher are the acidic components, which favors the use of alkali in the chemical EOR slug. The presence of alkaline along the surfactant can improve the displacement of oil by acting as a sacrificial agent and by generating in situ soaps. For very high viscosity heavy oil, an alkaline/surfactant alone could form an extremely viscous emulsion that partially plugs off the preferential water pathways, diverting further injected fluids and allowing access to some of the bypassed oil. According to Bryan et al. (2013)[14] such a recovery mechanism of plugging and flow diversion has a short-term effect.

Poor selection of surfactants can result in a huge economical loss and poor oil recovery, due to undesirable wettability alteration and possible blockage of the pores. Although, careful screening is required when designing a chemical EOR process for heavy crude oil[15, 16]. Most of the previous studies have been conducted at low salinity and low temperature conditions. There are limited publications on heavy oil at harsh conditions.

Therefore, the goal of this study is to evaluate the effect of common commercial types of EOR surfactants on different types of crude oils. The study focuses on measuring the IFT and CMC, in addition to assessing compatibility of each surfactant with synthetically prepared injection water. Four of the most commercially used EOR surfactants were tested, including a nano-surfactant encapsulated in-house.

Experimental Work

Materials

Surfactant solutions. The four surfactants used in this study are: (1) anionic alfa olefin, (2) cationic quaternary ammonium, (3) amphoteric (a betaine), and (4) a nano-surfactant encapsulated in-house. The brines are deionized water and synthetic injection brine. Table 1 is the synthetic brine composition of the injection brine.

Crude oil. Four crude oils were tested in this experimental work with different viscosities. Table 2 summarizes the gravity values of the four crudes as well as their classifications and viscosities. Viscosities were measured using the Anton Paar Physica MCR 301 Rheometer.

The program takes viscosity measurements at exponentially increasing shear rates in the range from 0.01 1/s to 1,000 1/s, at constant temperatures of 25 °C, 40 °C, and 60 °C. As an internal standard and for comparison, we select viscosity values at 6.81 1/s shear rate conditions. To determine the viscosity at 90 °C, we perform an Arrhenius-based extrapolation using the lower temperature experimental data.

Table 1 *The synthetic brine composition of the injection brine.*

Salt	Concentration (ppm)
NaCl	41,041
$CaCl_2 \cdot 2H_2O$	2,384
$MgCl_2 \cdot 6H_2O$	17,645
Na_2SO_4	6,343
$NaHCO_3$	165
Total Dissolved Solids	57,612

Table 2 *The properties of the four crude oil samples.*

Crude Oil	API°	Classification	Viscosity at 25 °C (cP)
1	36	Extra Light	13
2	24	Light	101
3	15	Medium	2,220
4	8	Heavy	47,700

Table 3 lists the viscosity measurements and extrapolated values. The densities of these crude oil samples were also measured as a function of temperature.

Figure 1 illustrates the variation in the densities.

Experimental Procedure

Compatibility. The compatibility of the four different surfactants was investigated by observing the solubility behavior of 0.2 wt% solutions, prepared in injection brine and after aging for 2 weeks at both room and reservoir temperatures, 25 °C and 95 °C, respectively. Four qualitative classifications (clear, slightly hazy, hazy, and precipitate) were used to describe the observations. The formulations belonging to the clear or slightly hazy classifications are considered compatible.

CMC. Stock solutions of the four surfactants were prepared in the injection brine. Surfactant concentrations were 0.2 wt%. For each CMC measurement, 60 ml of surfactant solution was placed in the Tensiometer glass vessel, Fig. 2.

The ring was thoroughly washed with alcohol followed by distilled water, and then it was heated using a blue flame. The ring was then placed in the Tensiometer and lowered into the solution to perform the surface tension measurement. After the first measurement, the micro-dispensers were used to dilute the stock solution progressively to a lower concentration.

At each dilution point, the surface tension was measured and recorded. A sudden change in slope was observed and the intersection point represented an estimate of CMC.

IFT. Similar to the CMC test, stock solutions of the four surfactants were prepared in injection brine at concentrations of 0.2 wt%. IFT tests were performed at 90 °C using a spinning drop Tensiometer. Figure 3 shows an image of the system used. First, the tube and the instrument as a whole was thoroughly cleaned using distilled water and then the surfactant solution was injected. An oil drop was filled with a surge needle positioned against the surfactant solution. After it was inserted in the spinning drop tensiometer, we raised the temperature. The camera was adjusted and calibrated, and the rotational speeds were set between 3,000 min^{-1} and 7,000 min^{-1}. All data were processed using Vonnegut's formula[17]:

$$\sigma = \frac{1}{4}\omega^2 \times \Delta\rho \times r^3 \quad (1)$$

where σ is the IFT (dynes/cm), ω is the angular

Fig. 1 Crude oil sample density measurement as a function of the temperature.

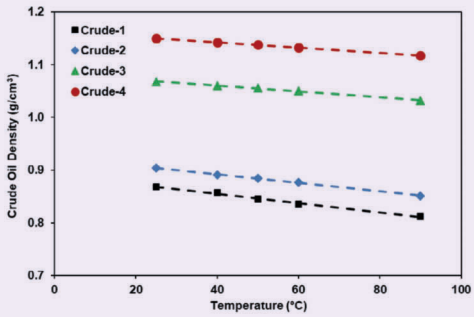

Fig. 2 The Du Noüy ring-type tensiometer with micro-dispensers for dilution.

Table 3 The viscosity measurements of four crude oil samples at different temperatures.

Temperature (°C)	Viscosity (cP)			
	Crude 1	Crude 2	Crude 3	Crude 4
25	13	101	2,220	47,700
40	9	39	473	9,260
60	6.2	20	173	1,450
90	3.7	6.1	26	123
100	3.1	4.3	15	60

Fig. 3 *The KRUSS spinning drop IFT system.*

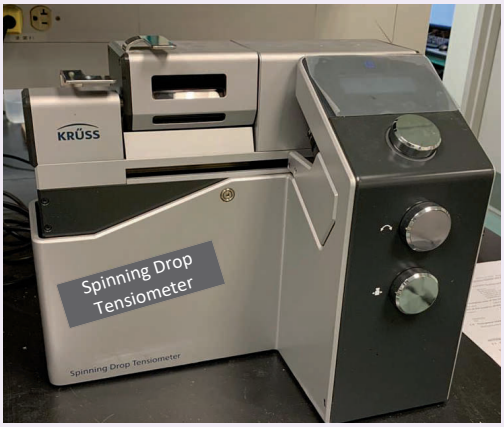

frequency (radian/sec), r is the radius of the oil drop (cm), and $\Delta\rho$ is the density difference between the two phases (g/cm^3). Several measurements were recorded for each formulation at 5-minute intervals until the IFT value reached equilibrium, Fig. 4.

Results and Discussion

Compatibility. All of the surfactant samples were found compatible with the injection water at 25 °C and 95 °C, respectively, Figs. 5 and 6.

CMC and Surface Tension. In general, the surface tension values varied slightly as the temperature varied from 25 °C to 60 °C, Fig. 7. At 60 °C, the cationic surfactant exhibited the highest surface tension, while the amphoteric resulted in the lowest. At room temperature (25 °C), the amphoteric solution surface tension was quite high — close to the highest — that was observed for the cationic surfactant.

It can be observed that the surface tension values of the other surfactants, i.e., anionic and nano-surfactant, at 60 °C are close to the amphoteric. Since the values of the amphoteric were gradually dropping with increasing temperature, we expect to have a further reduction at a higher temperature. The lower the surface tension,

Fig. 4 *The stabilization of the IFT measurement between the oil and surfactant solution at 95 °C.*

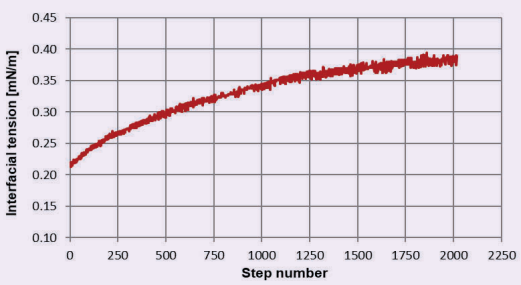

Fig. 5 *Compatibility of the surfactants with injection water at 25 °C.*

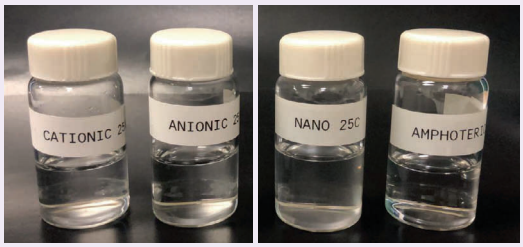

Fig. 6 *Compatibility of the surfactants with injection water at 95 °C.*

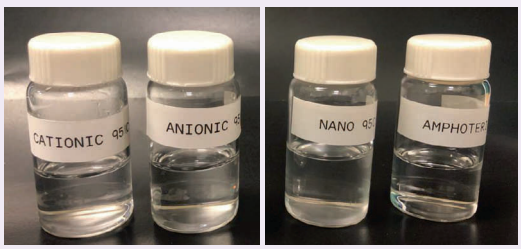

Fig. 7 *The surface tension for the four surfactants at CMC as a function of temperature, from 25 °C to 60 °C.*

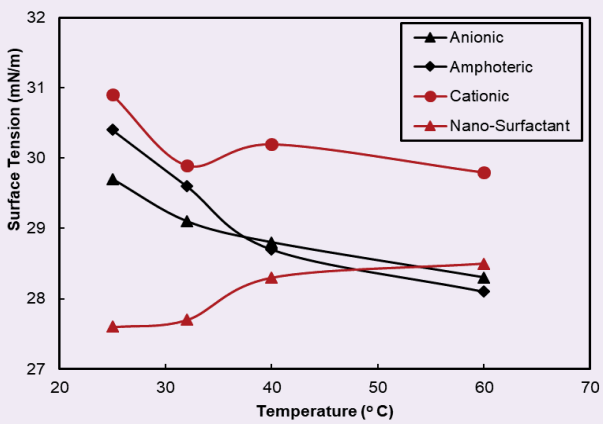

the better effect of the surfactant for EOR.

The effect of the temperature on CMC, Fig. 8, showed that the cationic surfactant exhibited very high CMC values compared to the other surfactants. The CMC value reached up to 260 ppm at 60 °C for the cationic surfactants. The CMC values for all surfactants, except the amphoteric, either slightly increased or remained constant as the temperature increased.

The CMC of the amphoteric surfactant decreased sharply as the temperature increased to 40 °C, then plateaued at around 0.8 ppm, which was the lowest CMC measured. Overall, the amphoteric surfactant

Fig. 8 *CMC values for the surfactants as a function of temperature.*

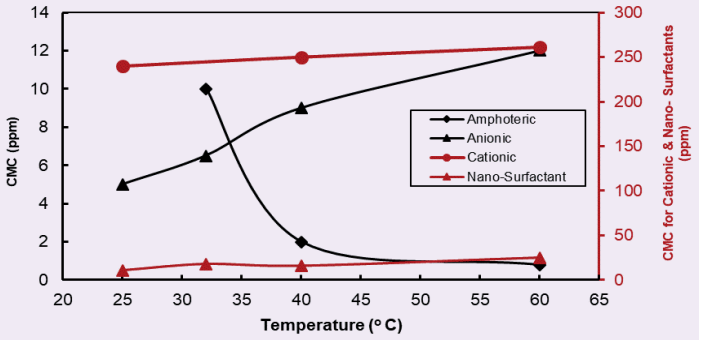

has demonstrated the most favorable surface tension and CMC values compared to the other surfactants.

IFT of Surfactants with Crude Oils at 90 °C

Figure 9 shows the results of the spinning drop tensiometer at a fixed temperature of 90 °C. It should be noted that the four crude oils resides at different reservoir conditions. For direct comparison of the surfactant's performance, we performed all tensiometry at the same temperature. Overall, the anionic and cationic samples showed distinctly higher IFT values than the amphoteric and nano-surfactant. The anionic and the cationic IFT values mostly exhibited a decreasing trend with the increase of the crude viscosity, while the amphoteric and nano-surfactant IFT values increased with the increase of oil viscosity.

The IFT values of each surfactant with the different crude oils indicate the unique interaction of the surfactants with each crude oil, which is not necessarily associated or correlated with the crude viscosity. The generalization that "the heavier the crude oil, the lower the IFT," is not always correct. Other oil components such as crude acidity and asphaltene content can highly affect the surfactant's ability to achieve a low IFT.

The lowest IFT values were around 0.02 mN/m and 0.05 mN/m. They were measured between the amphoteric surfactant and the first crude sample, and the nano-surfactant and the second crude sample, respectively. As mentioned earlier, synergism using more than a surfactant or other chemicals like alkaline is required when applying chemical EOR for heavier crude oil to achieve ultra-low IFT values[12, 13].

Fig. 9 *The IFT measurements of the surfactants and crude oils at 90 °C.*

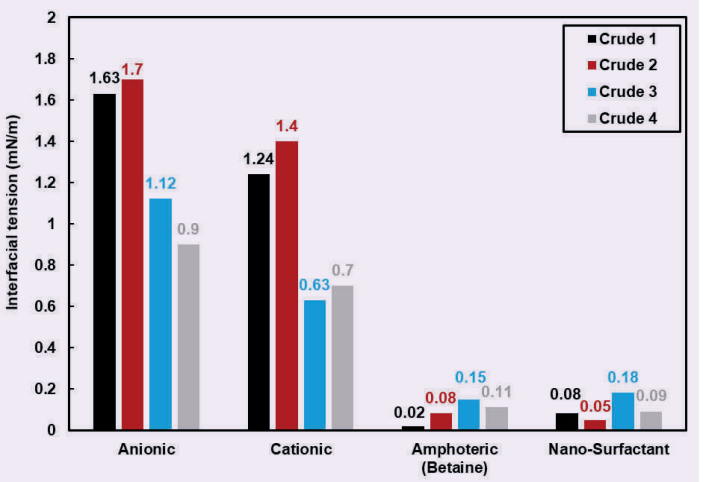

Summary and Conclusions

In this work, we evaluate the effect of crude oil gravity and composition on the selection of EOR surfactants at high temperature and high salinity. IFT values were measured using a spinning drop tensiometer for four commercial surfactants, including one nano-surfactant that was encapsulated in-house. The crude oil gravity varied between 36° and 8° API (Extra Light to Heavy crude oil).

The work included screening of surfactants using CMC and surface tension measurements at different temperatures. All four of the surfactants were prepared using a synthetic injection brine. We can summarize the main outcomes of this work as:

1. All surfactants showed good compatibility at 25 °C and 95 °C when prepared with the high salinity injection brine (total dissolved solids = 57,612 ppm).
2. The surface tension measurements showed close values at each of the measured temperatures (25 °C, 32 °C, 40 °C, and 60 °C) that ranged from 27 mN/m to 31 mN/m. Most of the surfactants showed a decreasing trend with the increase of temperature.
3. The CMC of the cationic surfactants showed remarkably high values compared to the other surfactants.
4. The CMC values for all surfactants, except the amphoteric, either slightly increased or remained constant as the temperature increased. The CMC value of the amphoteric surfactant sharply decreased as the temperature increased up to 40 °C, then plateaued with a value of 0.8 ppm at 60 °C, which was the lowest CMC measured.
5. The IFT measurements overall indicate that the anionic and cationic surfactants have distinctly higher IFT values than the amphoteric and nano-surfactants.
6. Both the anionic and the cationic IFT values exhibited a decreasing trend with increases in the crude gravity, while the amphoteric and nano-surfactant showed an opposite trend as gravity increased.
7. The IFT values of each surfactant with the different crude oils indicate the unique interaction of the surfactants with each crude oil, which is not necessarily correlated with the crude viscosity. Other oil components such as crude acidity and asphaltene content can highly affect the surfactant's ability to achieve a low IFT.
8. The lowest IFT values were around 0.02 mN/m and 0.05 mN/m, and were measured between the amphoteric surfactant and the Extra Light crude

oil, and the nano-surfactant and the Light crude oil, respectively.

Acknowledgments

The authors would like to thank Amr Abdel-Fattah for sharing samples of the nano-surfactant.

This article was prepared for presentation at the SPE Russian Petroleum Technology Conference, Moscow, Russia, October 12-14, 2020.

References

1. Fortenberry, R., Kim, D.H., Nizamidin, N., Adkins, S., et al.: "Use of Co-Solvents to Improve Alkaline/Polymer Flooding," *SPE Journal*, Vol. 20, Issue 2, April 2015, pp. 255-266.
2. Tagavifar, M., Herath, S., Weerasooriya, U.P., Sepehrnoori, K., et al.: "Measurement of Microemulsion Viscosity and Its Implications for Chemical EOR," SPE paper 179672, presented at the SPE Improved Oil Recovery Conference, Tulsa, Oklahoma, April 11-13, 2016.
3. Sahni, V., Dean, R.M., Britton, C., Kim, D.H., et al.: "The Role of Co-Solvents and Co-Surfactants in Making Chemical Floods Robust," SPE paper 130007, presented at the SPE Improved Oil Recovery Symposium, Tulsa, Oklahoma, April 24-28, 2010.
4. Liu, S., Zhang, D.L., Yan, W., Puerto, M., et al.: "Favorable Attributes of Alkali-Surfactant-Polymer Flooding," *SPE Journal*, Vol. 13, Issue 1, March 2008, pp. 5-16.
5. Fuseni, A.B., Al-Zahrani, B.H. and AlSofi, A.M.: "Critical Micelle Concentration of Different Classes of EOR Surfactants under Representative Field Conditions," SPE paper 188011, presented at the SPE Kingdom of Saudi Arabia Annual Technical Symposium and Exhibition, Dammam, Saudi Arabia, April 24-27, 2017.
6. Luque Alanis, P.A., AlSofi, A.M., Wang, J. and Han, M.: "Toward an Alternative Bio-Based SP Flooding Technology: I. Biosurfactant Evaluation," SPE paper 174621, presented at the SPE Enhanced Oil Recovery Conference, Kuala Lumpur, Malaysia, August 11-13, 2015.
7. Abdel-Fattah, A.I., Mashat, A., Alaskar, M. and Gizzatov, A.: "Nano-Surfactant for EOR in Carbonate Reservoirs," SPE paper 188046, presented at the SPE Kingdom of Saudi Arabia Annual Technical Symposium and Exhibition, Dammam, Saudi Arabia, April 24-27, 2017.
8. Malkin, A.Y., Zuev, K.V., Arinina, M.P. and Kulichikhin, V.G.: "Modifying the Viscosity of Heavy Crude Oil Using Surfactants and Polymer Additives," *Energy & Fuels*, Vol. 32, Issue 11, 2018, pp. 11991-11999.
9. McInnis, L.E., Hunter, K.D., Ellis-Toddington, T.T. and Grawbarger, D.J.: "Case Study of the Mannville B ASP Flood," SPE paper 165264, presented at the SPE Enhanced Oil Recovery Conference, Kuala Lumpur, Malaysia, July 2-4, 2013.
10. Delamaide, E., Zaitoun, A., Renard, G. and Tabary, R.: "Pelican Lake Field: First Successful Application of Polymer Flooding in a Heavy Oil Reservoir," SPE paper 165234, presented at the SPE Enhanced Oil Recovery Conference, Kuala Lumpur, Malaysia, July 2-4, 2013.
11. Zemb, T.N., Klossek, M., Lopian, T., Marcus, J., et al.: "How to Explain Microemulsions Formed by Solvent Mixtures without Conventional Surfactants," *Proceedings of the National Academy of Sciences of the United States of America*, Vol. 113, Issue 16, April 2016, pp. 4260-4265.
12. Liu, Q., Dong, M., Yue, X. and Hou, J.: "Synergy of Alkali and Surfactant in Emulsification of Heavy Oil in Brine," *Colloids and Surfaces A: Physicochemical and Engineering Aspects*, Vol. 273, Issues 1-3, February 2006, pp. 219-228.
13. Li, Y., He, X., Cao, X., Zhao, G., et al.: "Molecular Behavior and Synergistic Effects between Sodium Dodecylbenzene Sulfonate and Triton X-100 at Oil/Water Interface," *Journal of Colloid and Interface Science*, Vol. 307, Issue 1, March 2007, pp. 215-220.
14. Bryan, J., Shamekhi, H., Su, S. and Kantzas, A.: "Insights into Heavy Oil Recovery by Surfactant, Polymer and ASP Flooding," SPE paper 165440, presented at the SPE Heavy Oil Conference Canada, Calgary, Alberta, Canada, June 11-13, 2013.
15. Liu, S., Miller, C.A., Li, R.F. and Hirasaki, G.: "Alkaline/Surfactant/Polymer Processes: Wide Range of Conditions for Good Recovery," *SPE Journal*, Vol. 15, Issue 2, June 2010, pp. 282-293.
16. Rousseau, D., Bekri, S., Boujlel, J., Hocine, S., et al.: "Designing Surfactant-Polymer Processes for Heavy Oil Reservoirs: Case Studies," SPE paper 189745, presented at the SPE Canada Heavy Oil Technical Conference, Calgary, Alberta, Canada, March 13-14, 2018.
17. Gash, B. and Parrish, D.R.: "A Simple Spinning-Drop Interfacial Tensiometer," *Journal of Petroleum Technology*, Vol. 29, Issue 1, January 1977, pp. 30-31.

About the Authors

Amer M. Alanazi

M.S. in Petroleum Engineering, University of Calgary

Amer M. Alanazi is a Reservoir Engineer working for Saudi Aramco's Southern Area Oil Reservoir Management Department since 2009. He has a diversified work experience in reservoir simulation, reserves assessment, event solutions, integrated reservoir studies, production engineering, and as a petroleum researcher at the Exploration and Petroleum Engineering Center – Advanced Research Center (EXPEC ARC).

Amer is a level-2 candidate of the Technologist Development Program specializing in enhanced oil recovery (EOR) using chemical injection. He has authored and coauthored over 15 technical papers, mostly on reservoir engineering and chemical EOR.

During Amer's assignment with EXPEC ARC, he conducted several chemical EOR studies using coreflooding and micromodels. In addition, Amer led the investigation of a deep fluid diversion project using gel, presenting the findings to management.

He received the Society of Petroleum Engineers (SPE) Petroleum Engineering Certificate in 2011, and was recognized as the youngest Engineer to pass the certification exam.

Amer received his B.S. degree from King Fahd University of Petroleum and Minerals, Dhahran, Saudi Arabia, and his M.S. degree from the University of Calgary, Calgary, Alberta, Canada, both in Petroleum Engineering.

Dr. Abdulkarim M. Al-Sofi

Ph.D. in Petroleum Engineering, Imperial College London

Dr. Abdulkarim M. Al-Sofi is a Reservoir Engineer with Saudi Aramco's Exploration and Petroleum Engineering Center – Advanced Research Center (EXPEC ARC). He is currently the Champion of the Chemical Enhanced Oil Recovery Focus Area and is leading a new research initiative on heavy oil mobilization and recovery. Abdulkarim has also worked with the Reservoir Management, Reservoir Description and Simulation, and Reserves Assessment Departments.

He is the recipient of the 2009 Society of Petroleum Engineers (SPE) Annual Technical Conference and Exhibition Young Professional Best Paper Award in reservoir engineering, the recipient of the 2011 EXPEC ARC Best Presentation Award and the recipient of the 2013 Middle East Young Engineer of the Year Award.

Abdulkarim has authored 15 conference papers and seven peer-reviewed journal papers.

In 2006, he received his B.S. degree from the University of Texas at Austin, Austin, TX, and in 2010, Abdulkarim received his Ph.D. degree from Imperial College London, London, U.K., both degrees in Petroleum Engineering.

Ziyad F. Kaidar

Ziyad F. Kaidar is a Lab Technician with the Reservoir Engineering Technology Division of Saudi Aramco's Exploration and Petroleum Engineering Center – Advanced Research Center (EXPEC ARC).

He is an active member of the Society of Petroleum Engineers (SPE). Ziyad is the coauthor of two published SPE papers in the area of surfactant/polymer screening and conformance control effort.

He received his training from Saudi Aramco's Industrial Training Center (ITC) and Jubail Industrial College, Jubail, Saudi Arabia.

Dr. Khaled Abdelgawad

Ph.D. in Petroleum Engineering, King Fahd University of Petroleum and Minerals

Dr. Khaled Abdelgawad is a Postdoctorate Research Fellow in the Petroleum Engineering Department, at the College of Petroleum Engineering and Geosciences, King Fahd University of Petroleum and Minerals (KFUPM). Prior to this, he worked as a Research Assistant at KFUPM, 2011-2013, and as a Lecturer in the Petroleum Engineering Department, 2013-2018.

Khaled visited the Petroleum Engineering Department at the University of Texas at Austin for three months participating in a research exchange program in the area of chemical enhanced oil recovery (EOR). His research is directed at productivity enhancement and chemical EOR.

Khaled is an active member of the Society of Petroleum Engineers (SPE). He is the author of 12 published journal papers and has presented at several international SPE conferences. His papers are all published all by SPE.

Khaled holds three patents in the area of EOR and well stimulation.

He received his B.S. degree in Petroleum Engineering from Suez University, Suez, Egypt, and his M.S. and Ph.D. degrees from KFUPM, all in Petroleum Engineering.

Regional in Situ Stress Prediction in Frontier Exploration and Development Areas: Insights from the First 3D Geomechanical Model of the Arabian Plate

Dr. Rajesh Goteti, Dr. Yaser A. Alzayer and Dr. Hyoungsu Baek

Abstract /

We present results from the first ever 3D geomechanical model that supports pre-drill prediction of regional in situ stresses throughout the Arabian Plate. Using data from published studies, we developed a 3D finite element of the Arabian tectonic plate that takes into account interaction between its complex 3D plate geometry and present-day plate boundary velocities, to calculate elastic stresses in the Arabian crust. The model geometry captures the first-order topographic features of the Arabian Plate such as the Arabian shield, the Zagros Mountains, and the sedimentary thickness variations throughout the tectonic plate.

The results provide useful insights into the variations in the in situ stresses in sediments and crystalline basement throughout Arabia. The interaction between forces from different plate boundaries results in a complex transitional stress state — thrust/strike slip or normal/strike slip — in the interior regions of the plate such that the regional tectonic stress regime at any point may not be reconciled directly with the anticipated Andersonian stress regimes at the closest plate boundary. In the sedimentary basin east of the Arabian shield, the azimuths of the maximum principal compressive stresses (AMPS) change from ENE in SE portions to ~N-S in northern portions of the plate. The shape of the plate boundary, particularly along the collisional boundaries, plays a prominent role in controlling both the relative magnitudes and orientations of the principal stresses.

In addition, the geometry of the Arabian shield and variations in the sedimentary basin thickness cause significant local stress perturbations over 10 km to 100 km of length scales in different regions of the plate. The model presented here provides useful insights into the impact of plate boundary forces and crustal architecture on the regional stresses, in the absence of perturbation from local geological features such as faults, basin boundaries, and mechanical stratigraphy.

The results can be used in various applications in the petroleum industry such as exploration well planning, regional field development planning, hydraulic fracture stimulation design, wellbore stability analysis, and underground carbon storage.

Introduction

Knowledge of present-day stresses in sedimentary basins and the underlying crust is essential for applications in the petroleum industry, underground carbon storage, civil and mining engineering, and geothermal industry[1-5]. Two key factors exert first-order control on the regional stress patterns in the continental crust. These are the plate boundary forces and the intraplate forces arising from surface loads, e.g., mountain belts, and lateral density variations[6]. This conclusion is supported by the global patterns in the in situ stresses, documented through initiatives such as the World Stress Map[7], Fig. 1a, the Australian Stress Map[4, 8], Fig. 1b, and various studies in North America[9], Fig. 1c.

In this article, we investigate the impact of the aforementioned factors on the in situ elastic stress state within one of the youngest continental plates viz., the Arabian Pate. The Arabian Plate originated ~25 Ma ago[10, 11] by rifting of NE Africa to form the Gulf of Aden (GoA) and the Red Sea. The continental breakup was followed by the formation of a collision zone with eastern Turkey, Eurasia, and the Indo-Australian plate, which resulted in the formation of the Eastern Anatolian fault system, the Zagros fold and thrust belt (ZFTB), the Makran fold and thrust belt (MFTB), and the Owen Fracture Zone (OFZ), Fig. 2.

These boundaries define the present-day plate tectonic framework of the Arabian continental lithosphere. The interaction among various forces at these tectonic boundaries and displacements in the Arabian Plate result in a complex in situ stress field in the interior of the plate. As a result, stress at any given point in the plate cannot be directly reconciled with the anticipated Andersonian stress regime[12] at the closest plate boundary, Table 1.

Fig. 1 *(a) Data from the World Stress Map[7] showing the azimuths of the maximum horizontal stresses at and inside plate boundaries, (b) Results from a 2D geomechanical model of the Australian plate. The black arrows show the predicted azimuths of the maximum horizontal stresses[14], and (c) Stress regime map for the North American plate[9], showing the azimuth of the maximum horizontal stresses superposed on the tectonic fault regimes of Anderson (1951)[12].*

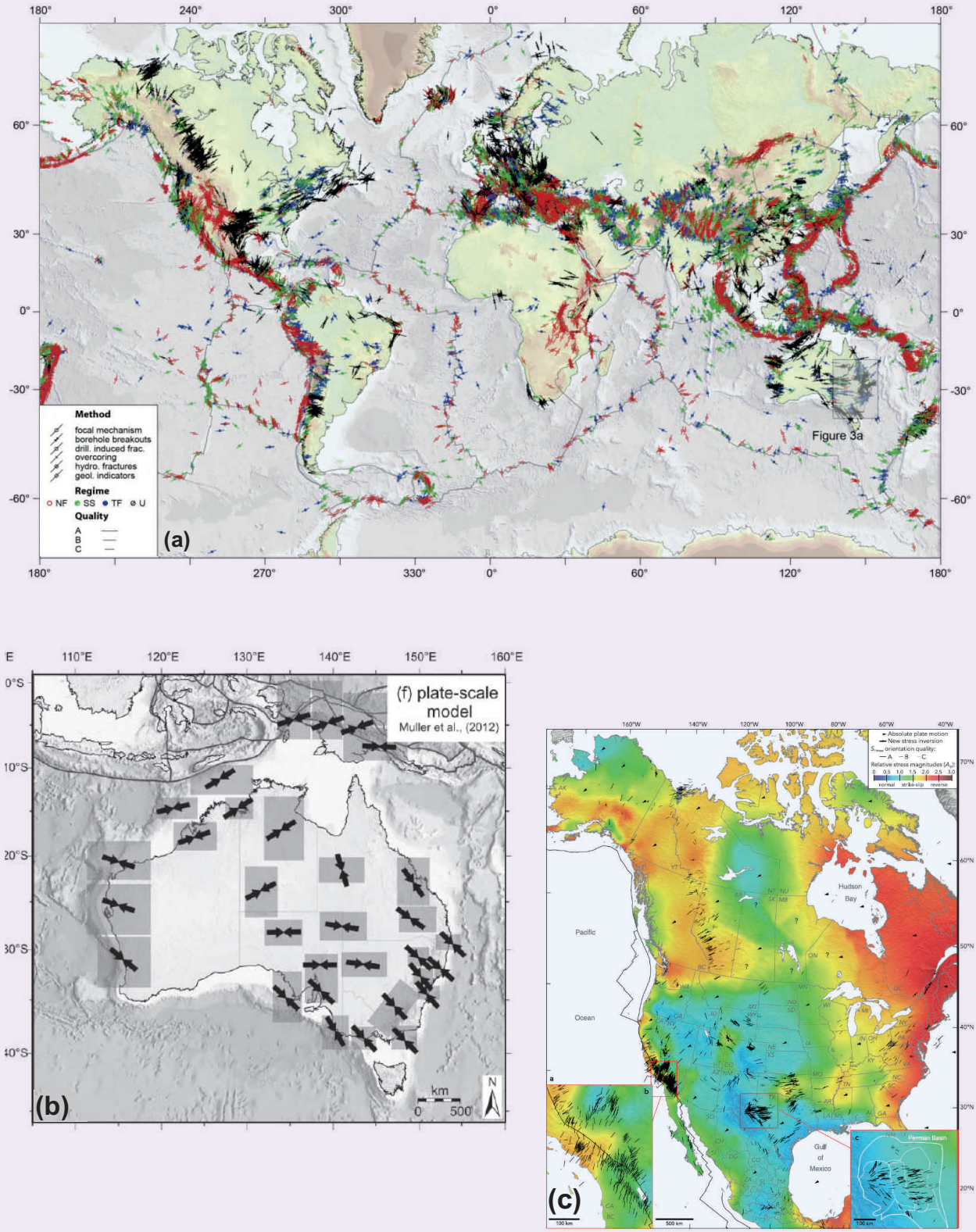

Fig. 2 *(Center) The residual GPS velocities of the Arabian plate[13] and schematic representation of the Arabian plate boundaries using block models[15]. Each boundary is characterized by a distinct stress regime. Arabian Gulf (AG), Red Sea (RS), Dead Sea fault (DSF), Zagros fold and thrust belt (ZFTB), Makran fold and thrust belt (MFTB), Owen Fracture Zone (OFZ), and Gulf of Aden (GoA).*

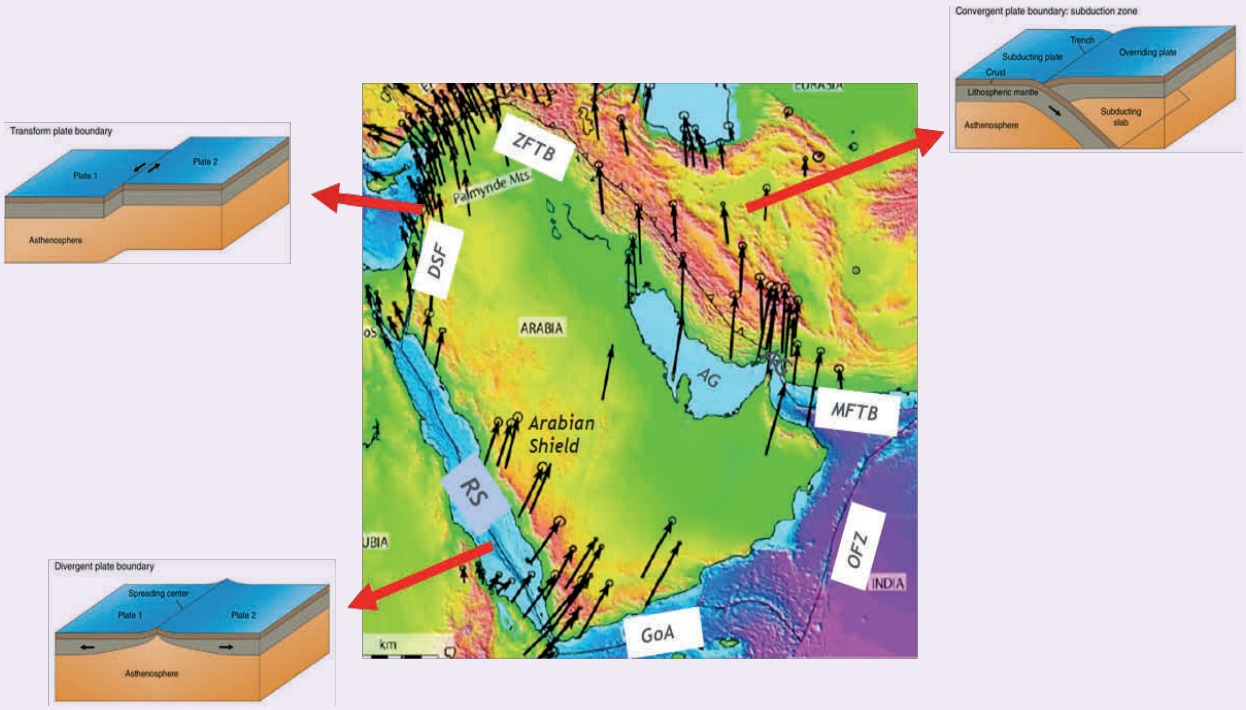

Table 1 *Tectonic stress regimes along various segments of the Arabian plate boundary.*

Geographical Feature	Associated Tectonic Margin Type	Anticipated Tectonic Stress Regime Along the Margin
Red Sea	Rift margin	Normal fault ($S_v > S_{HMax} > S_{HMin}$)
Gulf of Aqaba	Transform fault	Strike slip fault ($S_{HMax} > S_v > S_{HMin}$)
Eastern Anatolian fault	Transform fault	Strike slip fault ($S_{HMax} > S_v > S_{HMin}$)
ZFTB	Continental collision zone	Thrust fault ($S_{HMax} > S_{HMin} > S_v$)
MFTB	Continental collision zone	Thrust fault ($S_{HMax} > S_{HMin} > S_v$)
OFZ	Transform fault	Strike slip fault ($S_{HMax} > S_v > S_{HMin)}$
GoA	Rift margin	Normal/Transtensional fault ($S_v > S_{HMax} > S_{HMin}$)

In this article, we present some preliminary results from the first ever 3D geomechanical model of the Arabian Plate, which takes into account the observed plate boundary velocities[13], and simulates the in situ elastic stress field within the plate's interior. We demonstrate that the complex interaction of the various plate boundary forces and Arabian crustal architecture results in transitional stress states in various regions of the tectonic plate. We propose that such a model provides a predictive framework for in situ stress estimation in areas with scarce stress data in the Arabian Peninsula.

Geological Factors Considered in the Plate-Scale Model

Conceptually, stress in the subsurface represents the forces acting on all surfaces passing through any given point in a material continuum. The in situ stresses represent the summation of all forces acting on the surfaces from the plate-scale to the microscopic scale, e.g., stress concentrations at grain boundaries.

Table 2 shows some of the mesoscopic to megascopic sources of stresses in the sedimentary basins. Among these sources, global in situ stress patterns[2, 7, 16, 17] point

Table 2 *Controls on the in situ stresses in sedimentary basins (modified after Tingay et al. (2005))[3].*

Feature	Examples	Effect	Scale
Plate Boundary Forces	Mid-ocean ridges, continental collision zones, subduction zones	"Primary" control on stress field	Plate to regional: 100s to 1,000s of km
Major Intraplate Forces	Surface loads (mountains), isostatic compensation, continent-ocean transition deglaciation	"Secondary" control on stress field	Regional: 100s of km
Detachment Zones	Evaporites, overpressured shales, low angle faults	Mechanically detach overlying sediments from primary/secondary ("basement") stress field	Basin to local scale: 10 to 100s of km
Basin Geometry	Tertiary deltas, sedimentary basins	Regional control on stress field, particularly in detached basins	Basin scale (100s of km)
Geological Structures	Faults, fractures, diapirs, folds	Rotation of stress field due to mechanical contrasts between units	Local (meters to a few km)
	Active faults	Temporal change in stress associated with seismic cycle	Local to regional depending on scale of fault activity: 1 to 100s of km
Topography	Mountains, valleys	Rotation of principal stresses due to Earth's surface being a free surface	Shallow regions only: Near surface, within approximately one "wavelength" of topography

to some key controls on the first- and second-order stresses in continental lithospheres such as the Arabian Plate[6]. These are:

1. Plate boundary forces (first order).
2. Flexural stresses (second order).
3. Sedimentary loading on continental margins (second order).
4. Lateral density variations and topography (second order).
5. Continent-oceanic lithospheric transition (second order).
6. Glacial unloading (a relatively less important factor for the present-day stress in the Arabian Plate).

All the factors above impact the in situ stresses over different length scales. For example, plate boundary forces can affect stresses over lateral distances of thousands of km and up to a significant depth in the lithosphere. Flexural stresses and sedimentary loading, associated with orogens and crustal fault systems, impact stresses over distances of hundreds of km. Lateral density variations and topography, such as those caused by the Zagros orogen in the Arabian Gulf or the Arabian Shield in western Saudi Arabia, affect the in situ stresses over 10 km to 100 km. These primary and secondary sources of stresses are by far the main forces controlling the intra-plate stress field.

Over the past two decades, various academic studies[13, 18-21] analyzed the Arabian Plate deformation using a combination of GPS data, earthquake focal mechanisms and neotectonic geological indicators, e.g., volcanic dykes. Also seen in Fig. 2, the residual GPS velocities — velocities not consistent with coherent plate motion — reveal that the present-day internal deformation of Arabia is small and below the resolution of the published GPS observations (~1 mm/yr).

This observation supports the assumption of a quasi-rigid plate (for exceptions see AlOtaibi (2019))[21] with predominantly elastic strain accumulation in the interior portions of the Arabian Plate. Where observed, large displacement gradients in GPS data are often localized and associated with active geological features, e.g., faults.

In the model presented next, we assess the cumulative impact of factors 1 to 4 previously mentioned on the stress state in the Arabian Plate, which is modeled as a linear elastic solid. We do not consider the impact of the continent-oceanic transition in our analysis as the demarcation between the continental and oceanic crust in the Northern Red Sea is still debated and poorly constrained[10]. In the preliminary results presented later, we focus primarily on the effect of plate boundary forces on regional stress patterns and do not include the effects of tertiary geological features, e.g., fault systems, basin boundaries, and mechanical stratigraphy, which we assume, only affects the stresses locally.

Model Design

The 3D Arabian Plate geomechanical model discussed next uses the finite element modeling technique. The workflow employed in the creation of the model is summarized in Fig. 3.

Model Geometry and Material Properties

The first step in the development of a 3D geomechanical model is the creation of a watertight geometric framework using key geological surfaces that mark significant boundaries in the Arabian continental lithosphere.

These surfaces, in order of increasing depth are:

1. Topography (onshore) and bathymetry (offshore), which define the uppermost surface of the 3D model.
2. Interface between the sedimentary basin and the crystalline basement, i.e., top of crystalline basement[11, 22].
3. Base of the continental crust[23, 24].
4. Horizontal surface to define the lower boundary of the modeling domain:
   - A flat surface in the upper mantle, at a depth of 200 km below sea level, defines the lower boundary of the modeling domain. The chosen depth is below the isostatic compensation depth for the Arabian Plate and is sufficiently deep, such that any loading from the surface topography does not interfere with the fixed boundary condition at the base of the model.

The four layers listed are used to constrain a 3D watertight volume comprising of three layers viz., the sedimentary basin, crust, and upper mantle.

For defining the lateral extent of the model domain, we digitized the Arabian Plate boundary, which was then extruded vertically to create an enclosing control volume that intersects all four surfaces above. The plate boundary was scaled down in area, such that the extruded control volume intersects all the surfaces and that the resulting lateral faces (model boundary) are vertical and define a watertight configuration for all three layers. The three layers were assigned linear elastic material properties and densities.

Discretization

For the finite element analysis, the models were discretized using the 1.38 million C3D8R elements, which are general-purpose linear brick elements with reduced integration (1 integration point) and the simulation was done in the Abaqus software, Fig. 4.

Initial Stress State and Boundary Conditions

Following standard geological convention, compressive stresses are considered positive in this analysis. At the onset of the analysis, we assigned a pre-defined linear vertical stress gradient (24.5 MPa/km) with a lateral stress coefficient — ratio of horizontal to vertical effective stresses — of 0.8. This geostatic initialization step ensures that the initial geometry is in equilibrium with the gravitational loading before the imposition of the boundary conditions. If not implemented, significant deformation can accumulate before imposing the plate boundary displacements and the model geometry can deviate significantly from the present-day geometry of the Arabian Plate.

During geostatic initialization, we assigned a roller boundary condition for all the lateral faces of the model. Subsequently, in the analysis step, we converted

Fig. 3 *The workflow and data sources used for various stages in the development of the 3D Arabian Plate geomechanical model. The model presented considers the impact of features highlighted in the blue cells in Table 2.*

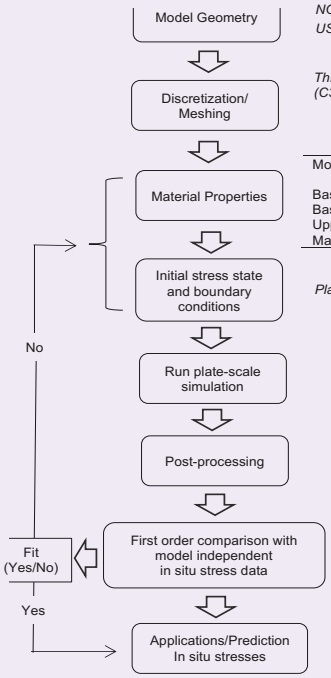

Model Layer	Young's Modulus (GPa)	Poisson Ratio	Density (kg/m^3)
Basin Cover	20	0.25	2,100
Basement	55	0.1	2,300
Upper Mantle	140	0.25	3,350

Fig. 4 *The finite element mesh showing the assignment of the linear hexahedral elements in all three layers. The mesh captures all the first-order geometry and topographic features such as the Arabian shield and Zagros orogen.*

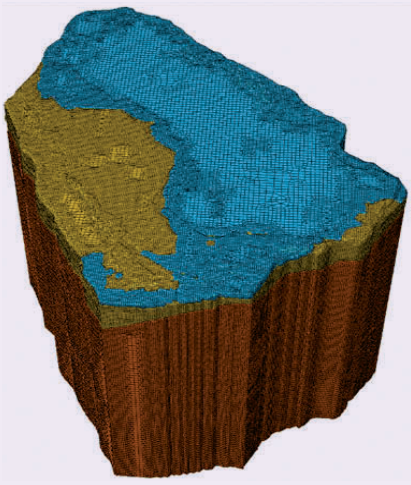

the plate boundary velocity vectors in ArRajehi et al. (2010)[13] to cumulative displacements over a 100,000-year duration, and imposed these along various segments of the plate boundary.

We assigned roller boundary conditions (zero horizontal velocities) along the northern and northeastern boundary — Zagros and Makran collision zones, and boundary with eastern Turkey — of the model Arabian Plate. This is consistent with the significantly reduced GPS velocities at these collision zones. We fixed the basal surface in the vertical direction throughout the analysis.

We do not consider the following factors in the model presented here:

1. Water loading in the Red Sea, and the Gulfs of Aqaba, Aden, and Arabia.
2. Pore pressure plays a very important role in the in situ stress state[25]. Owing to poor constraints on the regional distribution of initial pore pressures, we only focus on effective stresses ("dry rock") in the models presented here.
3. Thermal stresses[26].
4. Residual stresses[27] from past geological events are not considered in our analysis. The relative importance of residual stresses vis-à-vis present-day tectonic stresses is debated and difficult to constrain for modeling purposes.

The calculated final stress state in the model is a result of the superposition of the initial geostatic stress state and the stresses resulting from the imposed tectonic displacements and constraints along the plate boundaries. The boundary conditions were assigned such that the strains in the model domain remain low — < 0.4% at the finite element scale — and consistent with the assignment of linear elastic material properties.

Preliminary Results

In the following results, we specifically focus on the stress shape parameter[28-31] and the azimuth of the maximum principal compressive stresses (AMPS) across the Arabian Plate.

If S_1, S_2, and S_3 are the maximum, intermediate, and minimum principal compressive stresses, respectively, the stress shape parameter, $\emptyset$, is defined as:

$$\emptyset = (S_2 - S_3)/(S_1 - S_3) \quad (1)$$

The purpose of $\emptyset$ is to convey in one parameter the relative magnitudes of the principal stresses in relation to that of the intermediate principal stress[32]. $\emptyset$ is equal to 0 when the magnitudes of the intermediate and the minimum principal stresses are equal. Alternately, $\emptyset$ can attain a maximum value of 1 when the magnitude of the intermediate principal stress is equal to that of the maximum compressive stress.

Figure 5 is an image of the 3D Arabian Plate-scale geomechanical model, showing a horizontal slice at depth. The following trends can be observed and interpreted in the context of the Arabian Plate tectonic framework.

1. The low values of $\emptyset$ along the Southern Red Sea, the Dead Sea fault, the Zagros and Makran collisional zones, the Arabian Gulf, and the southeastern portion of the Arabian Plate. The Zagros and Makran

Fig. 5 *The results from the 3D Arabian Plate-scale geomechanical model, showing a horizontal slice at depth. The black line in the interior of the plate is the intersection between the "basement" and "overlying" sediment cover.*

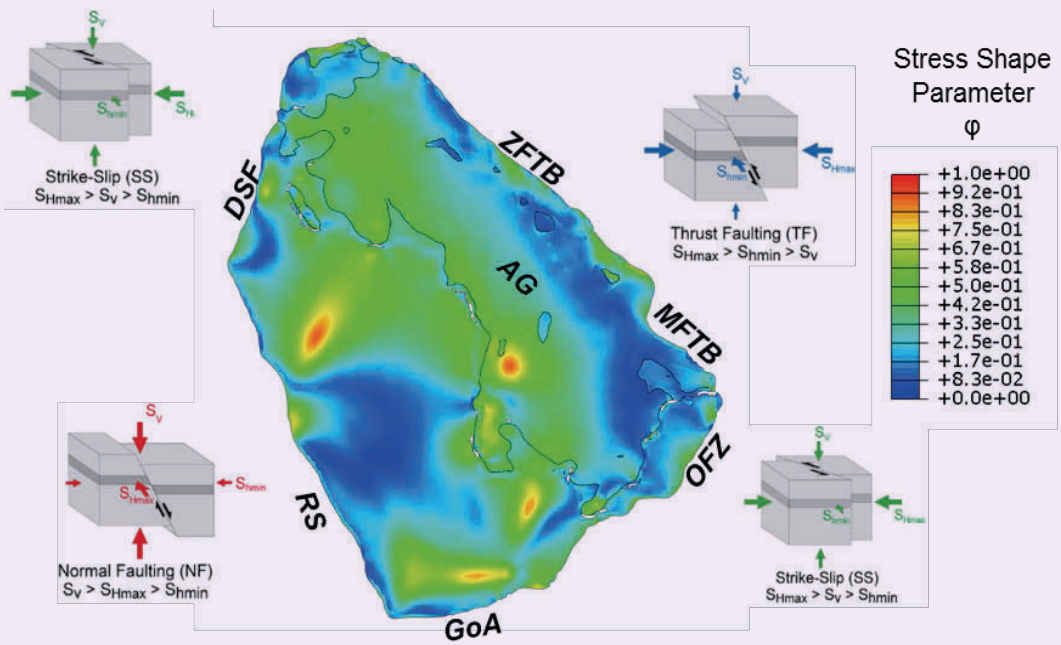

collision zones suggests that the intermediate and minimum principal stresses have close magnitudes in these locations.

2. The relative stress magnitudes exhibit significance along strike variations at each segment of the plate boundary, particularly where the boundary curvature changes.
3. Relatively uniform values of Ø (0.4 to 0.55) over large regions of the plate's interior suggest that the magnitude of S_2 is comparable to the mean magnitude of the other two principal stresses in these locations.
4. The variation of Ø (along an E-W transect) in the northern portion of the plate is a result of the superposition between the stresses arising from the collisional boundary in the East (Zagros) and the transform boundaries in the west (Eastern Turkey and the Dead Sea Fault). In addition, the flexural loading from the Zagros orogeny, and to a lesser extent, the topographic loading from the Arabian shield (particularly in SW Iraq) all contribute to the in situ stress variations in northern portions of the plate, including northern Saudi Arabia.
5. The Ø values are locally high in the Western Rub' al-Khali and NW Saudi Arabia. We hypothesize that the anomalous basin thickness in these locations may be causing these variations, albeit locally.
6. The rapid transition from moderate to low Ø values away from ZFTB suggests that the in situ stress perturbation from the Zagros orogen extends only from 100 km to 150 km inside the plate boundary.

In this article, we do not discuss the absolute magnitude of the principal stresses but only their relative magnitudes. This is because the deviatoric stresses in the linear elastic model presented here can be significantly larger than the typical frictional strength[33] of the upper continental lithosphere.

AMPS

Figure 6 shows the trends in the AMPS on a horizontal plane at a depth of 3 km below sea level. Please note that the maximum principal compressive stress does not necessarily coincide with the standard Andersonian maximum horizontal compressive stress, S_{HMax}. Therefore, any comparison presented is only a directional guide.

Several observations can be made regarding the spatial variations in the AMPS.

1. In the northeastern regions of the Arabian Plate, near the ZFTB and the MFTB, where the maximum compressive stress is sub-horizontal, AMPS is identical to the more widely used azimuth of the S_{HMax}[12].
2. Spatial variations in AMPS are generally consistent with the imposed boundary conditions along the various segments of the Arabian Plate boundary.
   a. Generally, the maximum principal stresses in the Zagros and Makran collisional zones run NNE-NE.
   b. Moderate to steeply plunging maximum principal compressive stress along the Red Sea and the GoA are consistent with the extensional/transtensional boundaries along these segments. The nonvertical plunge of the maximum compressive stress near the Red Sea is a departure from the anticipated Andersonian stress regime. We hypothesize that the presence of the high-relief topography east of the Red Sea (Arabian Shield) plays a strong role in the orientation of the principal stresses.

Future work will explore the effect of "pull" vs. "push" plate boundary forces on stress orientations and possible magnitudes along the Red Sea. In the current model,

Fig. 6 *Variations in the orientations of horizontal stress magnitudes and anisotropy in different regions of the Arabian plate. Stresses extracted from the plate-scale model can be used as boundary conditions for sub-models for reservoir management and field development.*

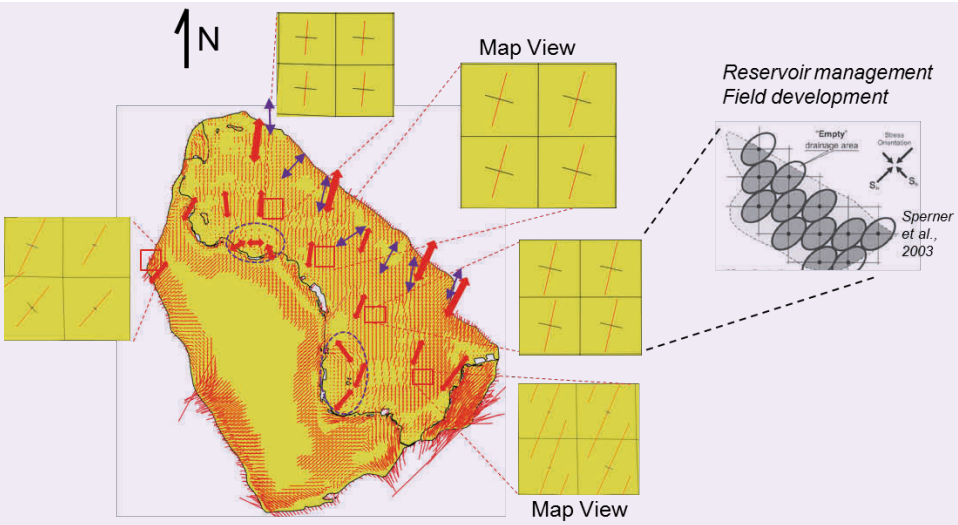

extension is primarily caused by differential stretching of the plate owing to larger displacements along the eastern portion of the GoA relating to those along the Red Sea boundary. Also, we did not include the sedimentary overburden along the Red Sea margin in our model.

c. The AMPS along the OFZ are consistent with the transition from transtensional to transform the margin in this region. The magnitude of the stresses is relatively high in this region (length of the arrows) due to the accommodation of the steep displacement gradient from the GoA on the west to very low displacements at the MFTB where the plate is kinematically "pinned."

Some additional observations are as follows:

1. Northeasterly AMPS are observed at the transition between the Red Sea and the Gulf of Aqaba.
2. In regions with anomalous sedimentary thickness (highlighted in ellipses in Fig. 6), the AMPS changes substantially over a localized region. In these locations, the AMPS wrap around the basement lows. We hypothesize that the local geometry of the basin plays a stronger role than the plate boundary forces in affecting the in situ stresses at these locations.
3. The AMPS changes from the NE in the southeastern portions of the plate to NNE near the Arabian Gulf. Farther north, it gradually changes to a ~N-S direction in western Iraq and eastern Syria.
4. Gholami et al. (2015)[34] documented the orientations of S_{HMax} from the ZFTB. Figure 6 also shows the orientation from their study by the purple arrows. The model results show general agreement with the regional trends from their work with some exceptions. We note that the effect of local structures (faults, folds) on the in situ stresses is not evident from their work.
5. Finally, the complex along strike variations in the AMPS at the collisional zone on the eastern boundary indicates the significance of the shape of the plate boundary on the in situ stresses. The azimuths vary from NNE-SSW in the MFTB to NE-SW near the southeastern end of the ZFTB. Farther north, the azimuths gradually rotate counterclockwise to a more NNE-SSW direction. Similar variations in the orientations of principal stresses have been hypothesized from other collisional plate boundaries where "indenter" tectonics predominated[35-37]. In the present context, the Arabian Plate is the indenter against the Eurasian Plate.

While the results presented here provide a sound starting point for the in situ stress prediction in the Arabian Peninsula, we note that a more detailed calibration to field data is warranted for a robust final model.

Applications of Plate-Scale Geomechanical Models

The Arabian Peninsula hosts some of the world's most prolific oil fields. Although extensive high-quality data exists, it is limited to regions with proven hydrocarbon fields. The regional in situ stress prediction framework from the model presented here can aid in providing a mechanics-based pre-drill stress estimate in frontier exploration and development areas with scarce stress data.

The results can be used for a broad range of oil and gas applications such as exploration well planning, regional field development, slip tendency analyses of faults, cap rock integrity studies for reservoir containment, underground CO_2 storage and designing hydraulic fracture reservoir stimulation. In addition, knowledge of stress state is also critical for applications in various other industries. Some examples include:

- Underground excavations (tunneling).
- Mining operations (stability and design).
- Large-scale infrastructure design (dams, tunnels).
- Stimulation of geothermal reservoirs[5, 38].
- Stability and safety analysis for underground gas storage or future nuclear waste disposal[2, 39].

Limitations

We note the following limitations, which need to be considered when interpreting the results:

1. The results presented are for a simplified geometry of the Arabian continental lithosphere. The model does not explicitly include major geological discontinuities — pre-Cambrian, Paleozoic, and Neotectonic fault systems — boundaries between individual sub-basins and lateral facies variations, all of which can contribute to significant local stress rotations with respect to the regional stresses.
2. Two prominent factors contribute to the stresses in a continental lithosphere[26, 40]: (1) differences in the gravitational potential energy (GPE) that arise from lateral density and topographic variations, e.g., Arabian shield, Zagros and Makran orogens, and (2) horizontal tractions at the base of the continental lithosphere arising from convection in the underlying mantle.

   The superposition of stresses from each of these factors controls the deviatoric stresses in the lithosphere, although their relative importance and weightage is still debated[9]. For example, numerical models of the North American plate have shown that models accounting for either GPE differences or mantle tractions can replicate lithospheric stress patterns only to a limited extent. Using 2D spherical shell modeling, AlOtaibi (2019)[21] demonstrated that the mantle tractions may in fact play a major role in controlling near surface stresses in the Arabian Plate. The author assumes a uniform lithospheric thickness across the entire Arabian Plate.

   In our model, we simulate the GPE component of the deformation by capturing the topographic features, lithospheric thickness variations as well as the plate boundary displacements. We however assumed little or no traction at the base of the Arabian continental lithosphere. A comparative study between the AlOtaibi (2019)[21] 2D study and the 3D approach presented here can provide more insights

into the factors affecting stresses in the Arabian Plate.

3. Sedimentary overburden, including the mechanical decoupling effect from thick salt layers in the Red Sea, is not included in our model.

In spite of these limitations, the current model can be used both for future studies on the neotectonic evolution of the Arabian Plate and for multiple field applications, which require pre-drill stress prediction. For example, if one of the principal stresses' magnitude is known from field data, e.g., S_v, the value of Ø from the model can be used to place constraints on the magnitudes of the other two principal stresses. Unlike parameters such as the regime stress ratio[4, 9], the shape stress parameter, Ø, does not indicate the tectonic stress regime[12], but should be used in combination with other indicators to identify the stress regime in any given location.

Conclusions

1. We presented preliminary results from the first ever 3D geomechanical model of the Arabian tectonic plate.
2. The model takes into account the present-day plate tectonic setting of the Arabian Plate, 3D sedimentary basin thickness variations, and surface topography in calculating the in situ stresses. It provides a predictive framework to support well planning in frontier exploration areas and regional field development planning throughout the Arabian tectonic plate.
3. The results from the study are compatible for multiple industry applications and provides a framework for advanced academic research on the neotectonic evolution of the Arabian Plate.
4. The model results suggest that the stress state in the interior of the Arabian Plate varies in a complex manner.
   a. Away from the plate boundaries, the relative magnitudes of the principal stresses vary laterally depending on the tectonic nature and superposition of forces from the closest plate boundaries. In addition, the architecture of the sedimentary basin also plays a significant role in affecting the stress ratio in the plate's interior.
   b. AMPS changes gradually from the NE in southeastern regions of the tectonic plate, to NNE near the Arabian Gulf. Farther north, it gradually changes to ~N-S direction in the northern portions of the plate.
   c. The shape of the plate boundary also has a significant impact on the rotation of the AMPS. Indentation tectonics can cause significant rotations along the plate boundary as well as the interior portions of the plate.
5. The current model highlights the interaction between plate boundary forces and crustal architecture in affecting the stresses within the Arabian Plate. It does not take into account the impact of local geological features such as faults and basin boundaries on the in situ stresses, and reflects the only impact of first-order controls on lithospheric stresses.

References

1. Zoback, M.D. and Zoback, M.L.: "Stress in the Earth's Lithosphere," *Encyclopedia of Physical Science and Technology*, Vol. 16, 2002, pp. 143-154.
2. Sperner, B., Müller, B., Heidbach, O., Delvaux, D., et al.: "Tectonic Stress in the Earth's Crust: Advances in the World Stress Map Project," *Geological Society, London, Special Publications*, Vol. 212, Issue 1, January 2003, pp. 101-116.
3. Tingay, M., Müller, B., Reinecker, J., Heidbach, O., et al.: "Understanding Tectonic Stress in the Oil Patch: The World Stress Map Project," *The Leading Edge*, Vol. 24, Issue 12, December 2005, pp. 1276-1282.
4. Rajabi, M., Tingay, M., Heidbach, O., Hillis, R., et al.: "The Present-Day Stress Field of Australia," *Earth-Science Reviews*, Vol. 168, May 2017, pp. 165-189.
5. Tomac, I. and Sauter, M.: "A Review on Challenges in the Assessment of Geomechanical Rock Performance for Deep Geothermal Reservoir Development," *Renewable and Sustainable Energy Reviews*, Vol. 82, Part 3, pp. 3972-3980.
6. Zoback, M.L.: "First and Second Order Patterns of Stress in the Lithosphere: The World Stress Map Project," *Journal of Geophysical Research: Solid Earth*, Vol. 97, Issue B8, July 1992, pp. 11703-11728.
7. Heidbach, O., Rajabi, M., Reiter, K., Ziegler, M., et al.: "World Stress Map Database Release 2016," *GFZ Data Services*, 2016.
8. Hillis, R.R. and Reynolds, S.D.: "The Australian Stress Map," *Journal of the Geological Society*, Vol. 157, Issue 5, 2000, pp. 915-921.
9. Lund Snee, J-E. and Zoback, M.D.: "Multiscale Variations of the Crustal Stress Field throughout North America," *Nature Communications*, Vol. 11, Issue 1, April 2020, pp. 1-9.
10. Bosworth, W., Huchon, P. and McClay, K.: "The Red Sea and Gulf of Aden Basins," *Journal of African Earth Sciences*, Vol. 43, Issues 1-3, October 2005, pp. 334-378.
11. Stern, R.J. and Johnson, P.: "Continental Lithosphere of the Arabian Plate: A Geologic, Petrologic, and Geophysical Synthesis," *Earth-Science Reviews*, Vol. 101, Issues 1-2, July 2010, pp. 29-67.
12. Anderson, E.M.: *The Dynamics of Faulting and Dyke Formation with Applications to Britain*, Hafner Pub. Co., 1951, 206 p.
13. ArRajehi, A., McClusky, S., Reilinger, R., Daoud, M.: "Geodetic Constraints on Present Day Motion of the Arabian Plate: Implications for Red Sea and Gulf of Aden Rifting," *Tectonics*, Vol. 29, Issue 3, June 2010.
14. Müller, R.D., Yatheesh, V. and Shuhail, M.: "The Tectonic Stress Field Evolution of India since the Oligocene," *Gondwana Research*, Vol. 28, Issue 2, September 2015, pp. 612-624.
15. Duarte, J.C. and Schellart, W.P.: "Introduction to Plate Boundaries and Natural Hazards," Chapter 1 in *Plate Boundaries and Natural Hazards*, Geophysical Monograph Series 219, John Wiley & Sons, August 2016, 352 p.
16. Zoback, M.L., Zoback, M.D., Adams, J., Assumpcao, M., et al.: "Global Patterns of Tectonic Stress," *Nature*, Vol. 341, September 1989, pp. 291-298.
17. Heidbach, O., Reinecker, J., Tingay, M., Müller, B., et al.: "Plate Boundary Forces are not enough: Second and Third Order Stress Patterns Highlighted in the World Stress Map Database," *Tectonics*, Vol. 26, Issue 6, December 2007, pp. TC6014-TC6033.

18. McQuarrie, N., Stock, J.M., Verdel, C. and Wernicke, B.P.: "Cenozoic Evolution of Neotethys and Implications for the Causes of Plate Motions," *Geophysical Research Letters*, Vol. 30, Issue 20, October 2003, pp. 6.1-6.4.

19. Bellahsen, N., Faccenna, C., Funiciello, F., Daniel, J.M., et al.: "Why did Arabia Separate from Africa? Insights from 3D Laboratory Experiments," *Earth and Planetary Science Letters*, Vol. 216, Issue 3, November 2003, pp. 365-381.

20. McClusky, S., Reilinger, R., Ogubazghi, G., Amleson, A., et al.: "Kinematics of the Southern Red Sea — Afar Triple Junction and Implications for Plate Dynamics," *Geophysical Research Letters*, Vol. 37, Issue 5, March 2010.

21. Alotaibi, T.: "Lithospheric Geodynamics of the Arabian Margin." Ph.D. Thesis, Pennsylvania State University, 2019.

22. Konert, G., Afifi, A.M., Al-Hajri, S.A., de Groot, K.M., et al.: "Paleozoic Stratigraphy and Hydrocarbon Habitat of the Arabian Plate," paper presented at the Pratt II Conference, San Diego, California, January 12-15, 2000.

23. Kaban, M.K., El Khrepy, S. and Al-Arifi, N.: "Isostatic Model and Isostatic Gravity Anomalies of the Arabian Plate and Surroundings," *Pure and Applied Geophysics*, Vol. 173, Issue 4, 2016, pp. 1211-1221.

24. Tesauro, M., Kaban, M.K., Petrunin, A.G., El Khrepy, S., et al.: "Strength and Elastic Thickness Variations in the Arabian Plate: A Combination of Temperature, Composition and Strain Rates of the Lithosphere," *Tectonophysics*, Vol. 746, October 2018, pp. 398-411.

25. Zoback, M.D.: *Reservoir Geomechanics*, Cambridge University Press, NY, 2010, 449 p.

26. Turcotte, D.L. and Schubert, G.: *Geodynamics*, 3rd edition, Cambridge University Press, NY, 2014, 639 p.

27. Engelder, T.: *Stress Regimes in the Lithosphere*, Princeton University Press, NJ, 2014, 486 p.

28. Bott, M.H.P.: "The Mechanics of Oblique Slip Faulting," *Geological Magazine*, Vol. 96, Issue 2, April 1959, pp. 109-117.

29. Angelier, J.: "Determination of the Mean Principal Directions of Stresses for a Given Fault Population," *Tectonophysics*, Vol. 56, Issues 3-4, July 1979, pp. T17-T26.

30. Angelier, J.: "Tectonic Analysis of Fault Slip Data Sets," *Journal of Geophysical Research: Solid Earth*, Vol. 89, Issue B7, July 1984, pp. 5835-5848.

31. Angelier, J.: "Inversion of Field Data in Fault Tectonics to Obtain the Regional Stress — III. A New Rapid Direct Inversion Method by Analytical Means," *Geophysical Journal International*, Vol. 103, Issue 2, April 2007, pp. 363-376.

32. Simpson, R.W.: "Quantifying Anderson's Fault Types," *Journal of Geophysical Research B: Solid Earth*, Vol. 102, Issue B8, August 1997, pp. 17909-17919.

33. Fossen, H.: *Structural Geology*, Cambridge University Press, NY, 2010, 463 p.

34. Gholami, R., Rasouli, V., Aadnoy, B. and Mohammadi, R.: "Application of in Situ Stress Estimation Methods in Wellbore Stability Analysis under Isotropic and Anisotropic Conditions," *Journal of Geophysics and Engineering*, Vol. 12, Issue 4, August 2015, pp. 657-673.

35. Gray, M.B. and Mitra, G.: "Migration of Deformation Fronts during Progressive Deformation: Evidence from Detailed Structural Studies in the Pennsylvania Anthracite Region, USA.," *Journal of Structural Geology*, Vol. 15, Issues 3-5, March-May 1993, pp. 435-449.

36. Gray, M.B. and Stamatakos, J.: "New Model for Evolution of Fold and Thrust Belt Curvature Based on Integrated Structural and Paleomagnetic Results from the Pennsylvania Salient," *Geology*, Vol. 25, Issue 12, 1997, pp. 1067-1070.

37. Weil, A.B. and Sussman, A.J.: "Classifying Curved Orogens Based on Timing Relationships between Structural Development and Vertical Axis Rotations," Chapter 1 in *Orogenic Curvature: Integrating Paleomagnetic and Structural Analyses*, Special Paper 383, The Geological Society of America, 2004, pp. 1-15.

38. Lashin, A., Chandrasekharam, D., Al Arifi, N., Al Bassam, A., et al.: "Geothermal Energy Resources of Wadi Al-Lith, Saudi Arabia," *Journal of African Earth Sciences*, Vol. 97, September 2014, pp. 357-367.

39. Fuchs, K. and Müller, B.: "World Stress Map of the Earth: A Key to Tectonic Processes and Technological Applications," *The Science of Nature*, Vol. 88, Issue 9, October 2001, pp. 357-371.

40. Ghosh, A., Holt, W.E. and Bahadori, A.: "Role of Large Scale Tectonic Forces in Intraplate Earthquakes of Central and Eastern North America," *Geochemistry, Geophysics, Geosystems*, Vol. 20, Issue 4, April 2019, pp. 2134-2156.

About the Authors

Dr. Rajesh Goteti

Ph.D. in Structural Geology and Geomechanics, University of Rochester

Dr. Rajesh Goteti is a Geological Specialist with the Petroleum Systems Modeling Team, in the Aramco Americas Houston Research Center (HRC), Houston, TX. He joined the HRC in 2014, and his primary area of expertise is structural geology and geomechanics. Since joining Aramco, Rajesh has worked in several diverse areas, including natural fracture prediction, salt tectonics, geomechanical forward modeling and regional in-situ stress prediction. Prior to joining Aramco, he worked as a Senior Geoscientist at the ExxonMobil Upstream Research Center. Rajesh's experience includes working in both conventional and unconventional basins worldwide.

He is an active member of the American Association of Petroleum Geologists (AAPG) and the American Rocks Mechanics Association (ARMA). Rajesh has published numerous papers in international journals, a book chapter, and was the co-editor for two special thematic articles in the *Petroleum Geoscience* journal.

He has received numerous internal and external recognitions for his work since joining Aramco, including the 2017 Exploration and Petroleum Engineering Center – Advanced Research Center (EXPEC ARC) Technology Milestone Award, the 2018 HRC Delivered Technology Award, and the 2019 ARMA Applied Rock Mechanics Award for his work on modeling salt tectonics in the Red Sea. Most recently, Rajesh was elected to the Petroleum Geoscience (Lyell Collection) Editorial Board in 2020. He was the recipient of the Academic Postdoctoral Fellowship from Dalhousie University, Halifax, Nova Scotia, Canada.

Rajesh received his B.S. and M.S. degrees in Applied Geology from the Indian Institute of Technology, Kharagpur, India, and his Ph.D. degree in Structural Geology and Geomechanics from the University of Rochester, Rochester, NY.

Dr. Yaser A. Alzayer

Ph.D. in Geological Sciences, University of Texas

Dr. Yaser A. Alzayer is Geoscientist leading the Unconventional Resources Focus Area in the Geology Technology Division of Saudi Aramco's Exploration and Petroleum Engineering Center – Advanced Research Center (EXPEC ARC). Prior to his current position, Yaser had multiple rotational assignments in the Southern Area Exploration, Wellsite Geology, and Geologic Solutions divisions.

Currently, he is leading several projects to enhance the mechanical and fracture characterization of conventional and unconventional reservoirs. Yaser's research interests include mechanical stratigraphy, fracture characterization, and forward geomechanical modeling.

He is an active member of the American Association of Petroleum Geologists (AAPG) and the Society of Petroleum Engineers (SPE). Yaser regularly serves as a technical reviewer for the *Journal of Petroleum Science and Engineering* and several international conferences such as the AAPG Annual Convention and Exhibition, the International Petroleum Technology Conference, and the American Rock Mechanics Symposium.

Yaser received his B.S. degree in Geology from the University of Kansas, Lawrence, KS. He also received his M.S. and Ph.D. degrees in Geological Sciences from the University of Texas at Austin, Austin, TX.

Dr. Hyoungsu Baek

Ph.D. in Applied Mathematics, Brown University

Dr. Hyoungsu Baek is an Applied Mathematician who worked for the Aramco Americas Houston Research Center (HRC), Houston, TX as a Research Geophysicist from 2014 to 2020. His research interests included seismic data processing, parallelized high performance computing and statics, and applying machine learning algorithms to automatic interpretation of fiber optic cable data for production monitoring.

Hyoungsu initiated and developed a distributed seismic data library to process huge amounts of seismic data, which bases simultaneous inversion of surface consistent amplitudes and statics. His innovative ideas and demonstrations were published and presented in multiple Society of Exploration Geophysics (SEG) conventions and workshops. In addition, Hyoungsu is specialized in image-based simulations and the application of computational geometry to process subsurface geometric data for meshing, simulation, and visualization.

He received his Ph.D. degree in Applied Mathematics from Brown University. After receiving his Ph.D., he worked at MIT as a Postdoctoral Associate to mitigate the ambiguities in inverse problems.

Condensate Banking Removal and Gas Production Enhancement Using Thermochemical Injection: A Field-Scale Simulation

Amjed Hassan, Mohamed Abdalla, Dr. Mohamed Mahmoud, Dr. Guenther Glatz, Dr. Abdulaziz Al-Majed, and Ayman R. Al-Nakhli

Abstract /

Condensate liquid accumulation near the well is known to curtail gas production up to 80%. Numerous approaches are employed to mitigate condensate banking and improve gas productivity. In this work, a field-scale simulation is presented for condensate damage removal in tight reservoirs using a thermochemical treatment strategy where heat and pressure are generated in situ. The impact of thermochemical injection on the gas recovery is also elucidated.

A compositional simulator was utilized to assess the effectiveness of the suggested treatment on reducing the condensate damage, and thereby improve the gas recovery. Compared to the base case, represented by an industry standard gas injection strategy, simulation studies suggest a significantly improved hydrocarbon recovery performance upon thermochemical treatment of the near wellbore zone.

For the scenarios investigated, the application of thermochemicals allowed for an extension of the production plateau from 104 days — as determined for the reference gas injection case — to 683 days. This represents a 6.5-fold increase in production plateau time, boosting gas recovery from 25% to 89%. The improved recovery is attributed to the reduction of both capillary pressure and condensate viscosity.

The presented work is crucial for designing and implementing thermochemical treatments in tight gas reservoirs.

Introduction

Condensate banking constitutes a common challenge for hydrocarbon production from tight gas reservoirs[1-3]. The reduction of reservoir pressure below dew point gives rise to condensate dropout[4-6]. Liquid accumulates near the wellbore, potentially reducing gas production by up to 80%[2, 7, 8]. Several methods are employed to remove condensate damage and restore gas productivity[3, 9]. Gas injection and hydraulic fracturing are among the most effective treatments in mitigating condensate banking[10-12].

Generally, gas injection strives to either increase or maintain pressure in proximity of the wellbore above the dew point pressure[10, 13, 14], allowing for the revaporization of the condensate liquid into the gas phase[4, 15, 16]. Usually, gas injection is initiated every six to nine months depending on specific reservoir conditions[3, 9]. Treatment involves the injection of hydrocarbon gases like methane, or nonhydrocarbon gases like nitrogen (N_2) or carbon dioxide (CO_2), in combination with a cyclic intervention approach[10, 12, 16-18].

The administration of CO_2 in a huff-and-puff configuration in particular shows great potential in mitigating condensate banking owing to the ability of CO_2 gas to reduce the dew point pressure of condensates, thereby counteracting liquid dropout[12, 19, 20]. Notably though, this procedure needs to be repeated about every six to nine months to maintain its effectiveness, giving rise to logistical challenges associated with CO_2 procurement, transportation, and on-site handling — challenging its economic viability[3, 9, 21].

Alternatively, hydraulic fracturing may be used to mitigate condensate banking by creating longer conductive paths between the wellbore and the formation[9, 11, 22]. Fractures induce help to reduce pressure drop, and delay condensate dropout[11, 23]. Consequently, once the reservoir pressure drops below the dew point as a result of the ongoing depletion process, liquids precipitate and accumulate within fractures, and then impede gas flow toward the production well[3, 9]. Solvent or gas injection may be used to vaporize the liquids and reestablish fracture conductivity[11, 23].

Evidently, gas injection, hydraulic fracturing, or a combination thereof constitute pragmatic approaches to mitigating condensate banking. Moreover, gas injection needs to be executed on a frequent basis to maintain its efficacy. Hydraulic fracturing only delays the inevitable development of a condensate bank. Therefore, at some point, gas injection may be required to become part of the reservoir management process. Both gas

injection and hydraulic fracturing treatments are of great concern with respect to project economics[3, 9].

Subsequently, in this article, an innovative condensate treatment concept based on thermochemical fluids (TCFs) is introduced[3, 24-27]. Exploiting enthalpy associated with the thermochemical reaction allows for remarkable increases in pressure and temperature to be realized downhole[28, 29]. The suggested treatment exhibits an attractive performance profile that can combat condensate banking related challenges for various types of gas reservoirs associated with carbonate, sandstone, and shale formations[27, 30].

Figure 1 illustrates the concept of thermochemical injection for removing the condensate bank. Initially, during gas production, condensate liquid drops out and accumulates near the wellbore, thereby restricting gas flow toward the producing well. The injection of TCFs into the condensate banking zone helps to reduce fluid viscosity and improve condensate mobility. Furthermore, the in situ generated pressure and temperature increase associated with the thermochemical reaction provides an additional driving force, enhancing the flow of the condensate liquid into the well.

Several fluids, such as magnesium sulfate, sodium nitrate, and ammonium chloride (NH_4Cl) solutions, may be used. Importantly, compared to conventional methods, the outlined process yielded higher thermal efficiency and lower energy loss compared to those of conventional gas injection methods on an equimolar basis.

Given successful lab trials[24-27, 30], this article for the first time presents a field-scale simulation based on experimentally obtained data for condensate removal from gas reservoirs by means of a thermochemical treatment strategy. In addition, sensitivity analysis was conducted to study the impact of different wellbore conditions on the gas production rate. Furthermore, the relationship between the condensate bank development, the gas production rate, and flowing bottom-hole pressure (FBHP) was investigated. Finally, the effectiveness of thermochemical treatments reflected in associated production profiles was contrasted with a conventional gas injection approach.

Methodology

Process Description

The described thermochemical process constitutes the injection of two chemicals that mutually react under downhole conditions to generate heat and nitrogen, thereby significantly increasing pressure and temperature. The induced temperatures and pressures can yield changes in excess of 533 K (500 °F) and 35 MPa (5,000 psi), respectively, depending on injected TCF volume and chemical concentrations. In this work, two aqueous solutions, sodium nitrite ($NaNO_2$) and NH_4Cl were used as TCFs. The thermochemical reaction is given by the following equation[24, 29]:

$$NH_4Cl + NaNO_2 \longrightarrow NaCl + 2H_2O + N_2 + \Delta H \quad (1)$$

The reaction could be accelerated by increasing the temperature and/or the lowering system's pH below 4. During the reaction, the produced N_2 led to a rise in pressure, and generated heat (ΔH) resulting in an increase in temperature. Consequently, TCF injection into a condensate region supported the revaporization of a portion of the condensate liquid, and the reduction of both condensate viscosity and density. Furthermore, in field applications, the chemical reaction could be triggered inside the reservoir formations to minimize risks associated with chemical reaction. TCFs can be injected into the formation around the wellbore; then, acidic fluid is injected to lower the pH, as it can activate exothermic reactions within the reservoir formation.

During the experimental investigation, heat and pressure were monitored, and condensate properties were measured before and after introducing the TCFs. Figure 2 displays the experimental configuration used to monitor the process. The setup consisted of a high-pressure, high temperature (HPHT) reactor, pressure temperature sensors, a heater, an N_2 cylinder, and a data acquisition system.

TCFs were injected into the HPHT reactor — without using a rock sample — to minimize the uncertainty associated with the rock's composition and then mixed, and the reaction was triggered by acetic acid. A pressure

Fig. 1 The proposed and experimentally proven technique for condensate bank removal using thermochemical injection.

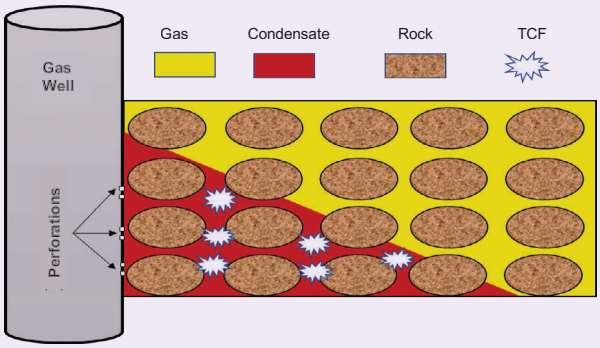

Fig. 2 The experimental setup for monitoring the thermochemical process.

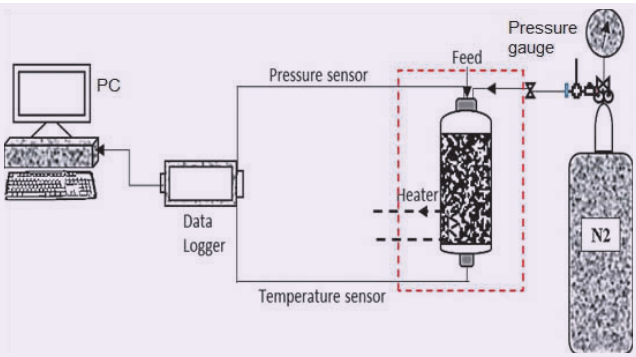

source (N_2 cylinder) was utilized to study the reaction behavior for various pressures. High accuracy sensors in combination with a data logging system were used to record the temperature and pressure profiles as a function of time.

Figure 3 summarizes the recorded temperature profiles resulting from the reaction at different initial system temperatures of 292 K, 314 K, 328 K, and 347 K (65 °F, 105 °F, 130 °F, and 165 °F). For all temperatures, the reaction increased the in situ temperature by around 333.15 K (140 °F). Expectedly, for the higher initial temperatures, temperature peaks were reached more quickly compared to the lower initial temperature conditions.

Figure 4 shows the conversion profiles of reactants as a function of time for the various initial temperatures. The time to reach the peak temperature decreased from 1,000 seconds, for an initial temperature of 292 K (65 °F), to around 320 seconds, for an operating temperature of about 347 K (165 °F).

In addition, the enthalpy impact on condensate liquids was investigated. Figures 5 and 6 illustrate the temperature and pressure profiles for two selected cases, a pure TCF and a TCF condensate system, respectively. Higher temperatures were recorded for the pure TCF system, while introducing the condensate liquid into the TCF system led to a reduction of the temperature, measured by around 7.4 K (11 °F) due to the added thermal capacity of the condensate.

The condensate properties were changed considerably after the chemical reaction occurred. Rheological measurements substantiated the condensate viscosity reduction from 0.94 cP to 0.57 cP after TCF injection, amounting to a 39% decrease. Upon injection, the generated pressure increased the gradient to push the condensate liquid toward the producing well. Importantly, the pressure generated multiple fractures, Fig. 7, in the treated formations, thereby increasing the pore throat size and reducing capillary pressure by up to 51%[25]. The reduction in capillary pressure due to the creation of multiple fractures can be explained by the following equation[25, 31]:

$$P_c = \frac{2\sigma cos\theta}{r}, \quad (2)$$

where P_c is the capillary pressure, σ is the interfacial tension, θ is the contact angle, and r is the pore throat size.

Reservoir Model

We utilized an advanced equation-of-state (EoS) compositional and unconventional simulator using Computer Modeling Group (CMG) software. The used data were collected from the available literature[32-34]. Ayub and Ramadan (2019)[12] examined reservoirs with respect to the areal extensions and associated drainage areas near the gas production well. They reported that a 1 km × 1 km sector could accurately represent the actual behavior of pressure depletion for a gas condensate reservoir. Consequently, the reservoir was built around a Cartesian grid covering a square

Fig. 3 *The temperature profiles for different initial vessel temperatures.*

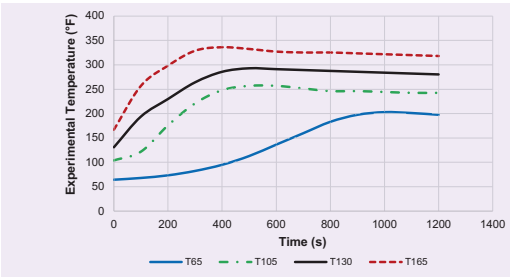

Fig. 4 *The conversion profiles for the different initial vessel temperatures.*

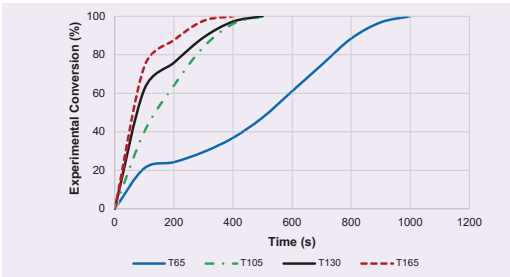

Fig. 5 *The temperature profiles for a pure TCF and the TCF condensate system.*

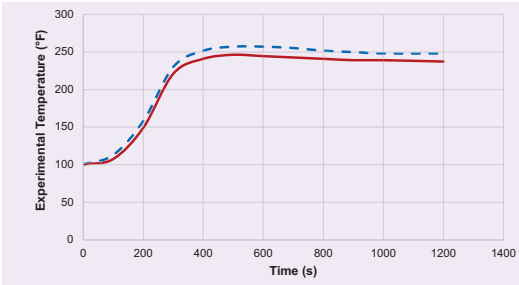

Fig. 6 *The pressure profiles for a pure TCF and the TCF condensate system.*

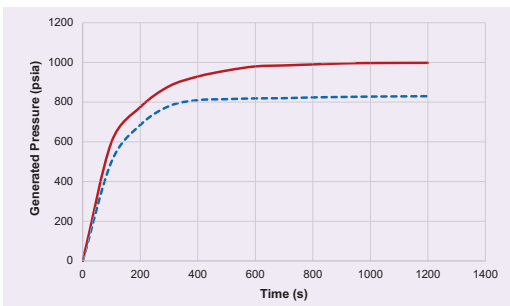

Fig. 7 *Images of the rock sample before and after thermochemical injection.Multiple fractures were induced upon thermochemical treatment[25].*

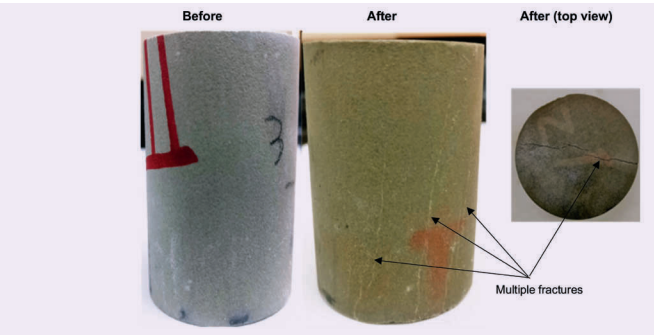

area of 1 km^2.

Figure 8 is a 3D view of the reservoir model used in this simulation. The initial reservoir conditions are listed in Table 1. Vertical heterogeneity is captured by defining four layers with permeabilities ranging from 5 mD to 315 mD. Based on field data reported[34], the reservoir porosity was given as 0.13, the initial reservoir pressure as 48.3 MPa (7,000 psi), the temperature as 408 K (275 °F), and the rock compressibility as 3.5e–8 1/Mpa (5.0e–6 1/psia). A single well was completed in the model center, and production was simulated for a total of five years. Two wellbore constraints were applied with a minimal FBHP of 10.4 MPa (1,500 psi) and a maximal flow rate of 30 million standard cubic feet per day (MMscfd).

In addition, relative permeability curves were generated using available correlations in the CMG software based on Correy's model[35]. Figure 9 summarizes the water and oil relative permeability curves, and Fig. 10 summarizes the gas and oil relative permeability curves used in this work.

Fluid Model

The fluid property characterization tool (WinProp) was employed to develop the EoS model based on the Peng-Robinson framework using the fluid composition listed in Table 2. Figure 11 details the resulting two-phase envelope. During production, the reservoir pressure decreased when entering the two-phase region, allowing for gas and liquid condensate to coexist.

Generally, it can be assumed that the gas is produced under isothermal conditions. Heat loss from the reservoir was considered negligible, due to the poor thermal conductivity of the reservoir rock and the insulating nature of the overburden formations. Importantly, constant composition expansion measurements were used

Fig. 8 *A 3D view of the rectangular reservoir model used in the simulation.*

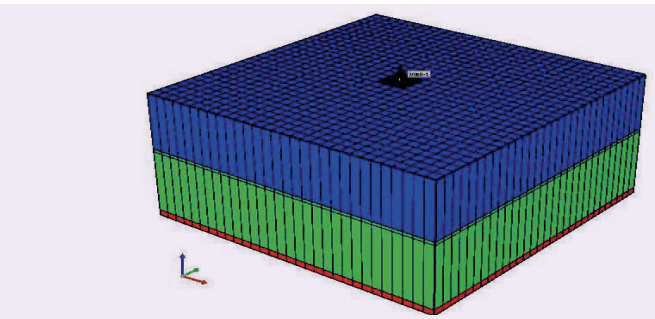

Fig. 9 *The water (K_{rw}) and oil (K_{row}) relative permeability curves used in the simulation model.*

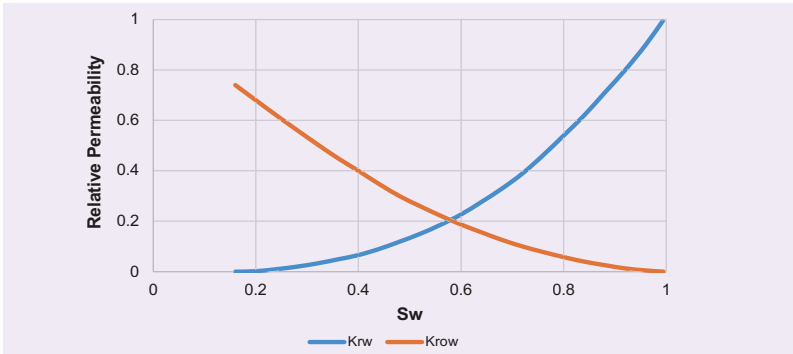

Table 1 *The diamond-graphite equilibrium curve.*

Parameter	Value
Total bulk reservoir volume (ft^3)	9.00E+08
Total pore volume (ft^3)	1.17E+08
Total hydrocarbon pore volume (ft^3)	9.83E+07
Original oil in place (STB)	1.79E+06
Original gas in place (scf)	2.77E+10

Fig. 10 *The gas (K_{rg}) and oil (K_{rog}) relative permeability curves used in the simulation model.*

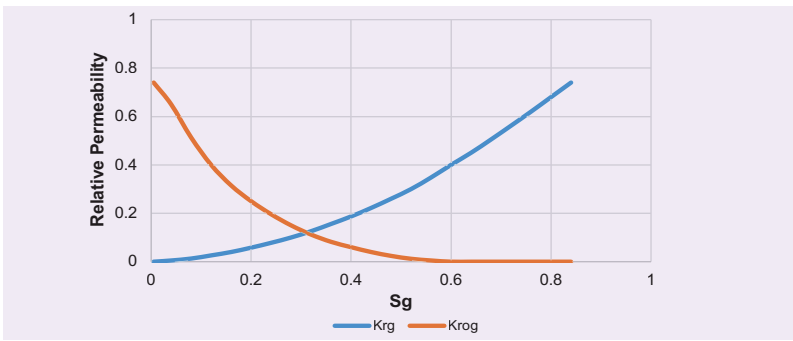

Table 2 *Fluid composition adopted in this work[32-34].*

Component	Mol %
N_2	10.07
CO_2	2.01
H_2S	2.65
CH_4	66.89
C_2H_6	6.85
C_3H_8	3.05
NC_4	1.25
IC_4	0.59
NC_5	0.5
IC_5	0.46
FC_6	0.68
FC_7	0.79
FC_8	0.8
FC_9	0.67
FC_{10}	0.53
FC_{11}	0.33
C_{12+}	1.88
Total	**100.00**

to validate the developed fluid model. Figure 12 shows that an acceptable match was achieved between the experimental measurements and the simulation results.

Results and Discussions

The simulation work was conducted in two stages: (1) condensate development, and (2) thermochemical injection. First, the impact of the wellbore conditions on the condensate formation was studied. The effects

Fig. 11 *The two-phase diagram for the gas condensate reservoir under consideration. The straight line indicates an assumed isothermal pressure depletion program.*

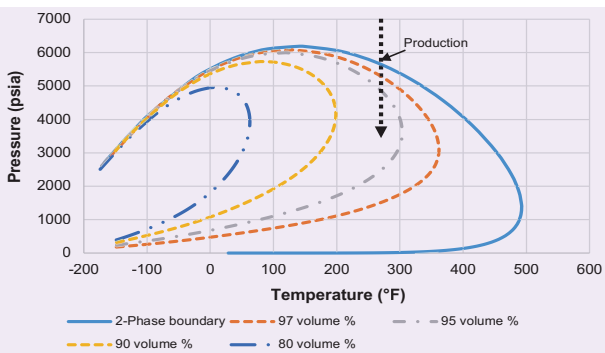

Fig. 12 *The simulation results and experimental measurements for constant composition expansion.*

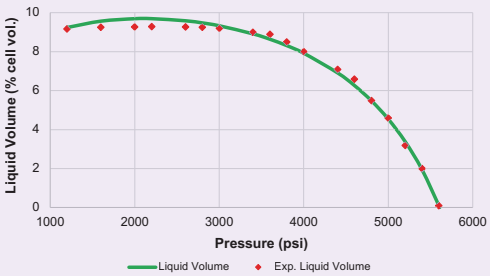

of FBHP and the gas production rate on the development of condensate banking were examined. A sharp decrease in the gas production profile served as an indicator for condensate banking. Next, production plateau time, defined as the duration of stabilized gas production, was calculated as functions of both the gas flow rate and FBHP.

During the second stage, the thermochemical treatment was initiated. The effects of the in situ generated heat, and pressure triggered by the thermochemical reaction on the condensate bank and gas production were studied. Finally, the effectiveness of the thermochemical treatment was compared with the efficiency of the conventional gas injection approach in terms of stabilized production times and total gas recovery.

Impact of FBHP

The relationship between the evolution of the condensate bank and associated FBHP was studied by producing the hydrocarbon gas at different levels of FBHP. Figure 13 summarizes the profiles of the gas flow rates at FBHP of 3.5 MPa, 6.9 MPa, and 10.4 MPa (500 psi, 1,000 psi, and 1,500 psi), respectively.

Production was constrained to a maximal gas flow rate of 30 MMscfd. Initially, the well produced at a constant production rate with the BHP decreasing as a result of the depletion process. Once pressure reached a specified BHP value (500 psi, 1,000 psi, and 1,500 psi), it was kept constant, and the production

Fig. 13 *The profiles of the gas flow rates at different levels of FBHP.*

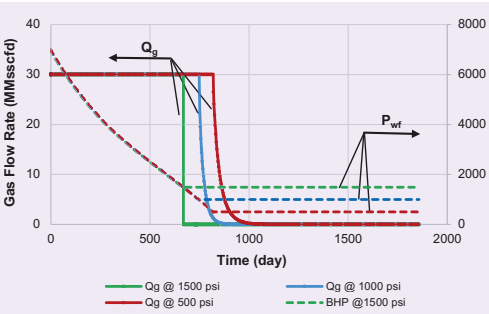

rate correspondingly decreased until it reached 0 MMscfd, revealing that the well had been killed due to condensate banking. At this point, the relationship between the stabilized gas production rate and FBHP was determined.

Figure 14 plots the production plateau as a function of the FBHP. Evidently, a decrease in FBHP allowed for sustaining the production plateau for increased periods. For example, the production plateau could be increased by approximately 13% by reducing the FBHP from 10.4 MPa to 6.9 MPa (1,500 psi to 1,000 psi). Consequently, curtailing the FBHP could exacerbate condensate dropout near the wellbore.

Impact of Gas Production Rate

Figure 15 encapsulates the gas production profiles for gas flow rates of 10 MMscfd, 30 MMscfd, and 60 MMscfd, respectively. The corresponding FBHP profiles are plotted in Fig. 16.

It can be observed that a constant production rate of 60 MMscfd could only be sustained for 400 days, with the rate sharply dropping thereafter due to flow impediments associated with condensate banking. Naturally, reducing the gas flow rate from 60 MMscfd to 10 MMscfd postpones the onset of liquid dropout.

Plotting the duration of the production plateau maintained in days vs. stabilized gas flow rate suggested exponential relation, as indicated in Fig. 17.

Fig. 14 *The duration of the production plateau plotted against the FBHP.*

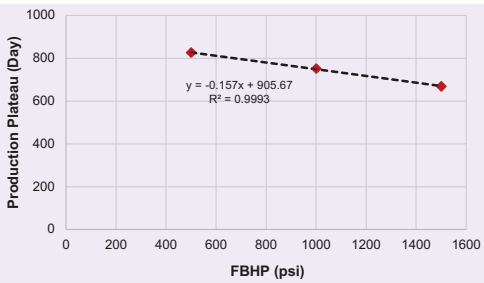

Fig. 15 *The profiles of gas production for gas flow rates of 10 MMscfd, 30 MMscfd, and 60 MMscfd, respectively.*

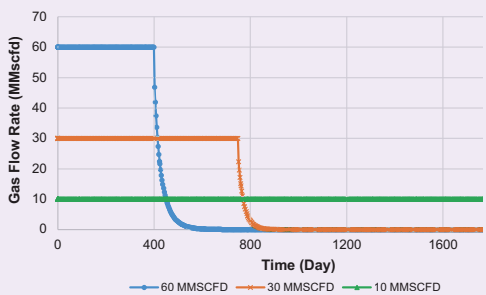

Fig. 16 *The profiles of the FBHP at gas production rates of 10 MMscfd, 30 MMscfd, and 60 MMscfd, respectively.*

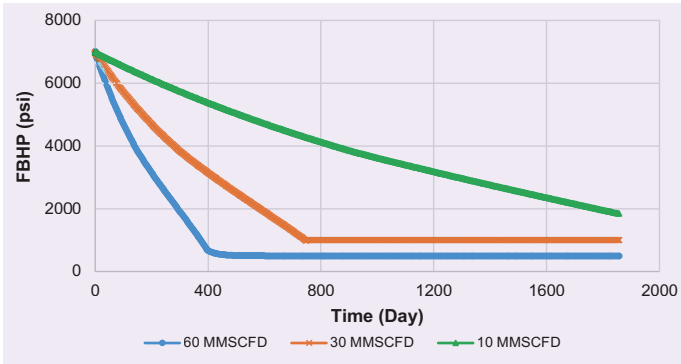

Fig. 17 *The stabilized production time (production plateau) plotted against the gas production rate.*

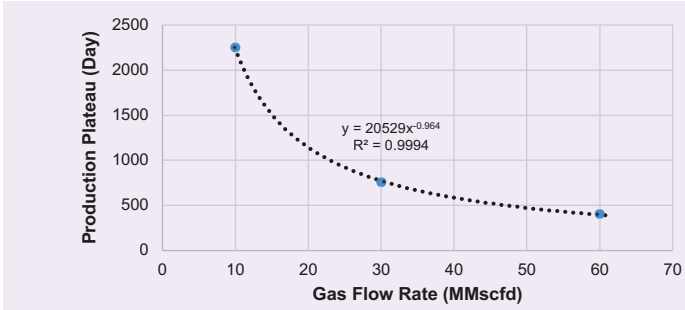

Thermochemical Treatment

The overall impact on gas production upon injection of TCFs into a gas condensate reservoir can be divided into three major components, all of which were included in the model.

First, the reaction products, mainly steam and nitrogen, yield an increase in pressure of up to 34.5 MPa (5,000 psi)[24, 28, 29]. Therefore, this effect finds equivalency in standard nitrogen injection.

Second, the released heat, able to boost temperatures in the order of 422 K (300 °F), promotes a reduction in viscosity[28].

Third, the pressure pulse resulting from released enthalpy stimulates the formation by creating microfractures. This particular effect was integrated by adjusting capillary pressure based on the work of Hassan et al. (2019)[9] and (2019)[25], who reported a reduction of the former by around 51%.

Figure 18 exemplifies the profiles of the gas flow rate and FBHP before and after thermochemical treatment. After 668 days of gas production, the FBHP dramatically dropped, resulting in a diminished gas flow rate due to condensate development. At this point, gas production was halted, and chemical treatment commenced.

Fig. 18 *The profiles of the gas production rate and FBHP prior to and after thermochemical treatment.*

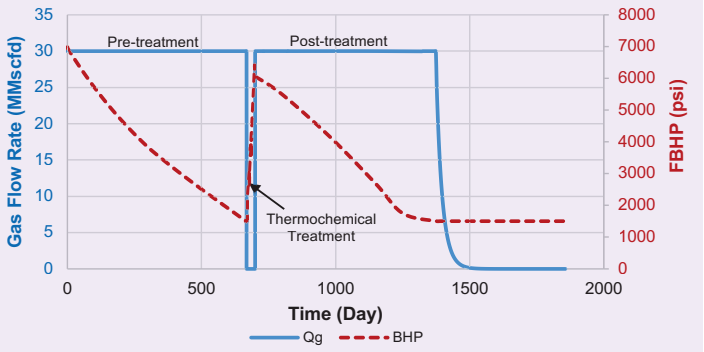

In total, three treatment cycles were performed; a chemical concentration of 1 molar and total chemical volume of 1,000 bbl were utilized. Each cycle was initiated with the injection of the chemicals, followed by a one-week soaking period. After completion of the cycles, production continued applying a maximal gas flow rate of 30 MMscfd, and a minimal FBHP of 10.4 MPa (1,500 psi). The intervention raised the pressure and temperature in the near wellbore region in excess of 31 MPa (4,500 psi) and 324.8 K (125 °F), respectively. Consequently, as illustrated in Fig. 19, liquids were revaporized, allowing for 683 additional days of gas flow rate at 30 MMscfd, succeeding the remedial efforts.

Comparison Analysis

The performance of the thermochemical treatment was compared to that of a conventional gas injection approach. The gas injection process was simulated using reservoir and wellbore conditions similar to thermochemical injection. The production well was shut-in after 668 days; subsequently, a mixture of N_2, CO_2, and CH_4 gases were injected in three cycles for a total of one month. All other parameters were kept the same with respect to the thermochemical treatment.

Figure 20 summarizes the profiles for gas production and the corresponding FBHPs pre- and post-treatment. After the gas injection treatment, production was stable only for a period of 104 days (3.5 months). With reference to Fig. 18, the thermochemical-based strategy enabled a sustained gas production rate for a period of 683 days (22.7 months) for equal reservoir and well conditions, extending the production plateau by a factor of 6.5, compared to the gas injection case.

The cumulative gas production is plotted in Fig. 21. The conventional approach only allowed for a production of 23.2 MMscf, equivalent to a total gas recovery of about 25% of hydrocarbons in place. In contrast, the application of thermochemicals improved gas recovery by a factor of 1.76 MMscf to 40.8 MMscf, corresponding to a total recovery of approximately 89% of the gas in place.

Given that the injected gas had a similar composition to that of reservoir fluids, no chemical reaction was expected, and only condensate revaporization took place. Gas injection only increases pressure in the near wellbore region, fostering the revaporization of the condensate liquid, thereby improving gas flow into the wellbore[16, 17]. Thermochemical injection, however, not only increases pressure, but also reduces capillary forces and decreases condensate viscosity[24-27].

Fig. 19 *The revaporization of condensate liquid due to thermochemical treatment.*

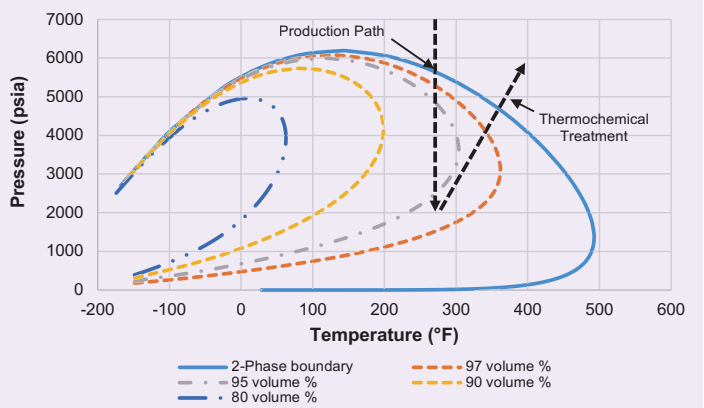

Fig. 20 *The profiles of the gas production and associated FBHP before and after the gas injection treatment.*

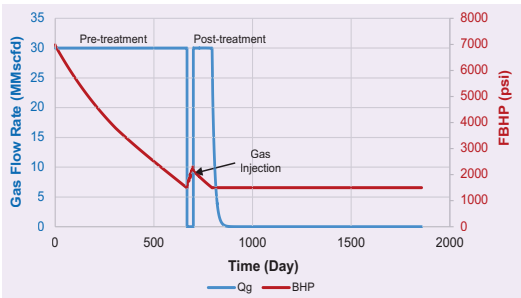

Fig. 21 *The profiles of the cumulative gas production during thermochemical treatment and gas injection.*

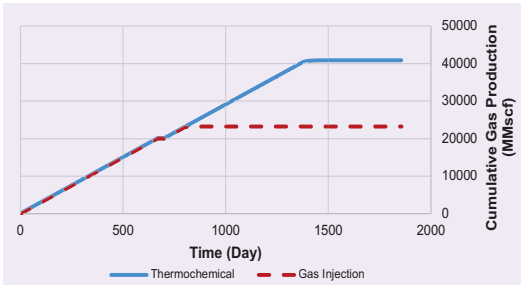

Conclusions

This work presented a field-scale simulation quantifying the effectiveness of thermochemical injection for removing the condensate bank, thereby improving gas recovery. The following conclusions could be drawn from this work:

- Compared to conventional gas injection treatment, the thermochemical approach was found to be vastly superior in coping with condensate banking-related production issues.
- The simulation work indicated that thermochemical injection could restore the initial reservoir condition and sustain gas production for more than 680 days, compared to 104 days using gas injection treatment.
- For the particular model used in this investigation, total gas recovery for the thermochemical-based procedure was 89%, compared to 25% for the traditional gas injection approach.
- In the case of the thermochemical-based approach, the exothermic nature of the thermochemical reaction released pressure and heat, thereby increasing pressure around the wellbore and heating fluids in this region.
- Edicts reacted rather violently, giving rise to a pressure pulse, fostering the creation of microfractures accompanied by an appropriate reduction in capillary pressure.

References

1. Craft, B.C. and Hawkins, M.: "Gas Condensate Reservoirs," Chapter 2 in *Applied Petroleum Reservoir Engineering*, Prentice-Hall, NJ, 1959, pp. 59-96.
2. Al-Anazi, H.A., Pope, G.A., Sharma, M.M. and Metcalfe, R.S.: "Laboratory Measurements of Condensate Blocking and Treatment for both Low and High Permeability Rocks," SPE paper 77546, presented at the SPE Annual Technical Conference and Exhibition, San Antonio, Texas, September 29-October 2, 2002.
3. Sayed, M.A. and Al-Muntasheri, G.A.: "Mitigation of the Effect of Condensate Banking: A Critical Review," *SPE Production & Operations*, Vol. 31, Issue 2, May 2016, pp. 85-102.
4. Muskat, M.: *Physical Principles of Oil Production*, "Chapter 11: Complete-Water-Drive Reservoirs," McGraw-Hill Book Co., NY, 1949, pp. 528-644.
5. Kniazeff, V.J. and Naville, S.A.: "Two-Phase Flow of Volatile Hydrocarbons," *Society of Petroleum Engineers Journal*, Vol. 5, Issue 1, March 1965, pp. 37-44.
6. Novosad, Z.: "Composition and Phase Changes in Testing and Producing Retrograde Gas Wells," *SPE Reservoir Engineering*, Vol. 11, Issue 4, November 1996, pp. 231-235.
7. Ahmed, T.: *Reservoir Engineering Handbook*, "Chapter 1: Fundamentals of Reservoir Fluid Behavior," Gulf Publishing Co., Houston, Texas, 2000, pp. 1-28.
8. Liu, D., Sun, W. and Ren, D.: "Experimental Investigation of Pore Structure and Movable Fluid Traits in Tight Sandstone," *Processes*, Vol. 7, Issue 3, March 2019, p. 149.
9. Hassan, A., Mahmoud, M., Al-Majed, A., Alawi, M.B., et al.: "Gas Condensate Treatment: A Critical Review of Materials, Methods, Field Applications, and New Solutions," *Journal of Petroleum Science and Engineering*, Vol. 177, June 2019, pp. 602-613.
10. Linderman, J.T., Al-Jenaibi, F.S., Ghori, S.G., Putney, K., et al.: "Feasibility Study of Substituting Nitrogen for Hydrocarbon in a Gas Recycle Condensate Reservoir," SPE paper 117952, presented at the Abu Dhabi International Petroleum Exhibition and Conference, Abu Dhabi, UAE, November 3-6, 2008.
11. Mahdiyar, H. and Jamiolahmady, M.: "Optimization of Hydraulic Fracture Geometry in Gas Condensate Reservoirs," *Fuel*, Vol. 119, March 2014, pp. 27-37.
12. Ayub, M. and Ramadan, M.: "Mitigation of Near Wellbore Gas Condensate by CO_2 Huff-n-Puff Injection: A Simulation Study," *Journal of Petroleum Science and Engineering*, Vol. 175, April 2019, pp. 998-1027.
13. Luo, K., Li, S., Zheng, X., Chen, G., et al.: "Experimental Investigation into Revaporization of Retrograde Condensate by Lean Gas Injection," SPE paper 68683, presented at the SPE Asia Pacific Oil and Gas Conference and Exhibition, Jakarta, Indonesia, April 17-19, 2001.
14. Einstein, M.A., Gerder Castillo, Y.C. and Gil, J.C.: "A Novel Improved Condensate Recovery Method by Cyclic Supercritical CO_2 Injection," SPE paper 107283, presented at the Latin American and Caribbean Petroleum Engineering Conference, Buenos Aires, Argentina, April 15-18, 2007.
15. Fevang, Ø. and Whitson, C.H.: "Modeling Gas Condensate Well Deliverability," *SPE Reservoir Engineering*, Vol. 11, Issue 4, November 1996, pp. 221-230.
16. Meng, X. and Sheng, J.J.: "Experimental and Numerical Study of Huff-n-Puff Gas Injection to Revaporize Liquid Dropout in Shale Gas Condensate Reservoirs," *Journal of Natural Gas Science and Engineering*, Vol. 35, Part A, September 2016, pp. 444-454.
17. Meng, X. and Sheng, J.J.: "Optimization of Huff-n-Puff Gas Injection in a Shale Gas Condensate Reservoir," *Journal of Unconventional Oil and Gas Resources*, Vol. 16, December 2016, pp. 34-44.
18. Wang, F., Liu, Y., Hu, C., Wang, Y., et al.: "Experimental Study on Feasibility of Enhanced Gas Recovery through CO_2 Flooding in Tight Sandstone Gas Reservoirs," *Processes*, Vol. 6, Issue 11, November 2018, pp. 214-226.
19. Odi, U.: "Analysis and Potential of CO_2 Huff-n-Puff for Near Wellbore Condensate Removal and Enhanced Gas Recovery," SPE paper 160917, presented at the SPE Annual Technical Conference and Exhibition, San Antonio, Texas, October 8-10, 2012.
20. Monger, T.G. and Khakoo, A.: "The Phase Behavior of CO_2 — Appalachian Oil Systems," SPE paper 10269, presented at the SPE Annual Technical Conference and Exhibition, San Antonio, Texas, October 4-7, 1981.
21. Jia, B., Tsau, J-S. and Barati, R.: "A Review of the Current Progress of CO_2 Injection EOR and Carbon Storage in Shale Oil Reservoirs," *Fuel*, Vol. 236, January 2019, pp. 404-427.
22. Li, L., Sheng, G. and Su, Y.: "Water-Gas Two-Phase Flow Behavior of Multi-Fractured Horizontal Wells in Shale Gas Reservoirs," *Processes*, Vol. 7, Issue 10, 2019, pp. 664-683.
23. Khan, M.N., Siddiqui, F.I., Mansur, S. and Ali, S.D.: "Hydraulic Fracturing in Gas Condensate Reservoirs: Successes, Setbacks and Lessons Learned," SPE paper 142848, presented at the SPE/PAPG Annual Technical Conference, Islamabad, Pakistan, November 10-11, 2010.

24. Hassan, A.M., Mahmoud, M.A., Al-Majed, A.A., Elkatatny, S., et al.: "Novel Technique to Eliminate Gas Condensation in Gas Condensate Reservoirs Using Thermochemical Fluids," *Energy & Fuels*, Vol. 32, Issue 12, 2018, pp. 12843-12850.

25. Hassan, A.M., Mahmoud, M.A., Al-Majed, A.A., Al-Nakhli, A.R., et al.: "Mitigation of Condensate Banking Using Thermochemical Treatment: Experimental and Analytical Study," *Energies*, Vol. 12, Issue 5, February 2019, pp. 800-812.

26. Hassan, A.M., Mahmoud, M.A., Al-Majed, A.A., Al-Shehri, D., et al.: "Gas Production from Gas Condensate Reservoirs Using Sustainable Environmentally Friendly Chemicals," *Sustainability*, Vol. 11, Issue 10, 2019, pp. 2838-2853.

27. Al-Nakhli, A.R., Hassan, A.M., Mahmoud, M.A. and Al-Majed, A.A.: "Removal of Condensate Banking from Different Formations Using Thermochemical Treatment," SPE paper 197847, presented at the Abu Dhabi International Petroleum Exhibition and Conference, Abu Dhabi, UAE, November 11-14, 2019.

28. Al-Nakhli, A.R., Sukkar, L.A., Arukhe, J., Mulhem, A., et al.: "In Situ Steam Generation a New Technology Application for Heavy Oil Production," SPE paper 184118, presented at the SPE Heavy Oil Conference and Exhibition, Kuwait City, Kuwait, December 6-8, 2016.

29. Alade, O.S., Mahmoud, M.A., Hassan, A.M., Al-Shehri, D., et al.: "Evaluation of Kinetics and Energetics of Thermochemical Fluids for Enhanced Recovery of Heavy Oil and Liquid Condensate," *Energy & Fuels*, Vol. 33, Issue 6, April 2019, pp. 5538-5543.

30. Hassan, A.M., Mahmoud, M.A., Al-Majed, A.A. and Al-Nakhli, A.R.: "New Chemical Treatment for Permanent Removal of Condensate Banking from Different Gas Reservoirs," *ACS Omega*, Vol. 4, Issue 26, December 2019, pp. 22228-22236.

31. Xu, H., Fan, Y., Hu, F., Li, C., et al.: "Characterization of Pore Throat Size Distribution in Tight Sandstones with Nuclear Magnetic Resonance and High-Pressure Mercury Intrusion," *Energies*, Vol. 12, Issue 8, April 2019, pp. 1528-1545.

32. Temeng, K.O., Al-Sadeg, M.J. and Al-Mulhim, W.A.: "Compositional Grading in the Ghawar Khuff Reservoirs," SPE paper 49270, presented at the SPE Annual Technical Conference and Exhibition, New Orleans, Louisiana, September 27-30, 1998.

33. Kuntadi, A.: "North Field, Qatar: A Study of Condensate Blockage and Petroleum Streams Management," M.S. thesis, Norwegian University of Science and Technology, Trondheim, Norway, June 2004, 125 p.

34. Whitson, C.H. and Kuntadi, A.: "Khuff Gas Condensate Development," IPTC paper 10692, presented at the International Petroleum Technology Conference, Doha, Qatar, November 21-23, 2005.

35. Corey, A.T., Rathjens, C.H., Henderson, J.H. and Wyllie, M.R.J.: "Three-Phase Relative Permeability," *Journal of Petroleum Technology*, Vol. 8, Issue 11, November 1956, pp. 63-65.

About the Authors

Amjed Hassan

M.S. in Petroleum Engineering
King Fahd University of Petroleum and Minerals

Amjed Hassan is a Ph.D. Researcher at King Fahd University of Petroleum and Minerals (KFUPM), and a lecturer at the University of Khartoum, Sudan. His research interests are varied and cover condensate removal processes, enhanced oil recovery methods, well testing, and artificial intelligence applications in the petroleum industry.

Amjed has participated in many workshops, conferences, and regional contests. He has received several awards, the most recent include the Society of Petrophysicists and Well Log Analysts (SPWLA) prize for the best research in petrophysics, and the Schlumberger award for the best academic performance in petroleum engineering.

Amjed is the author of 15 of scientific articles and Society of Petroleum Engineers (SPE) papers.

He received his M.S. degree in Petroleum Engineering from KFUPM.

Mohamed Abdualla

M.S. in Petroleum Engineering,
King Fahd University of Petroleum and Minerals

Mohamed Abdualla is currently working as a Petroleum Engineering Software Engineer at the College of Petroleum and Geoscience's Department of Petroleum Engineering, at King Fahd University of Petroleum and Minerals (KFUPM), Dhahran, Saudi Arabia.

Previously, he worked as a Teaching Assistant in the Petroleum Engineering Department of the University of Khartoum, Sudan. While working on his M.S. degree, Mohamed was involved as a Research and Teaching Assistant.

He received his B.S. degree in Petroleum Engineering from the University of Khartoum, Khartoum, Sudan, and his M.S. degree in Petroleum Engineering from KFUPM.

Dr. Mohamed Mahmoud

Ph.D. in Petroleum Engineering,
Texas A&M University

Dr. Mohamed Mahmoud is an Associate Professor working in the Petroleum Engineering Department of the King Fahd University of Petroleum and Minerals (KFUPM), Dhahran, Saudi Arabia. Prior to assuming this position in 2016, he had been a Research Assistant in the same department since 2008. Mohamed has taught both undergraduate and graduate courses in Petroleum Engineering.

Since joining KFUPM in 2011, he has been a member (PI and COI) in several externally funded projects carried out by the Research Institute (the Petroleum Engineering Department at KFUPM), KACST, SABIC, and Saudi Aramco. Mohamed has also conducted several projects in the area of productivity enhancement and enhanced oil recovery (EOR).

From 2004 to 2008, he worked as a Petroleum Engineer at Belayim Petroleum Co. in Egypt. During the period from 2001 to 2004, Mohamed was a Drilling Engineer at Magawish Petroleum Co., Egypt.

He has published more than 150 technical papers and a large number of reports related to various areas of research, including formation damage and well stimulation. Mohamed holds 43 patents in the area of productivity enhancement and EOR.

He is a member of the Society of Petroleum Engineers (SPE) and the Society of Petrophysicists and Well Log Analysts (SPWLA).

Mohamed received the Distinguished Researcher Award in 2017 and the Distinguish Teaching Award in 2016.

He received his B.S. degree in 2001, his M.S. degree in 2006, and his Ph.D. degree in 2011, all in Petroleum Engineering and from Texas A&M University, College Station, TX.

Dr. Guenther Glatz

Ph.D. in Petroleum Engineering, Stanford University

Dr. Guenther Glatz has worked for several national and international energy companies, most notably as a Technology Consultant for the Chief Technology Office of British Petroleum (BP) and as a Reservoir Engineer Consultant for Total S.A.

His research focuses on visualizing and quantifying flow and transport phenomena under extreme temperature and pressure conditions in 4D. Guenther also investigates the application of image processing and deep learning methods to improve coiled tubing data quality and to allow for the detection of phenomena on a sub-voxel level.

In 2009, he received his B.S. degree in Petroleum Engineering from the Mining University of Leoben, Leoben, Austria. In 2012, Guenther received his M.S. degree and in 2017, he received his Ph.D. degree, both in Petroleum Engineering from Stanford University, Stanford, CA.

Dr. Abdulaziz A. Al-Majed

Ph.D. in Petroleum Engineering, University of Southern California

Dr. Abdulaziz A. Al-Majed is an Associate Professor working in the Department of Petroleum Engineering at King Fahd University of Petroleum and Minerals (KFUPM) in Dhahran, Saudi Arabia. Prior to that he was Chairman of the Department and Director of the Center for Petroleum and Minerals at the Research Institute in KFUPM.

Abdulaziz has taught courses in drilling engineering, reservoir engineering, and petroleum engineering economics, supervised numerous M.S. Thesis and Ph.D. Dissertation committees, and managed many client funded research projects in the Research Institute. He has published over 60 journal and conference papers, and obtained five patents. Abdulaziz has won several educational and research awards.

He was a member of the committee that prepared the "Strategic Plan for Innovation, Localization and Development of Oil and Gas Exploration and Production Technologies in Saudi Arabia." Abdulaziz was also the Team Leader of the team charged to prepare "The Improved Drilling Operations; Quality and Efficiency Technology Target Area" as part of the Strategic Plan.

He is a member of the Society of Petroleum Engineers (SPE) and the American Institute of Mining Engineers (AIME), and a previous member of the Board of Directors of the SPE-Saudi Arabia Section.

In 1978, Abdulaziz received his B.S. degree from KFUPM, in 1981, he received his M.S. degree from Stanford University, Stanford, CA, and in 1988, Abdulaziz received his Ph.D. degree from the University of Southern California, Los Angeles, CA, all in Petroleum Engineering.

Ayman R. Al-Nakhli

M.S. in Entrepreneurship for New Business Development, Open University Malaysia

Ayman R. Al-Nakhli is a Petroleum Scientist in Saudi Aramco's Exploration and Petroleum Engineering Center – Advanced Research Center (EXPEC ARC), where he leads the research program on thermochemicals and develops technologies related to conventional and unconventional reservoirs such as pulse fracturing, stimulation, water shutoff, diverting agents, and heavy oil.

Ayman has developed several novel technologies, and received the World Oil Award for Best Production Chemical in 2015. He has also been awarded for his innovative work within Saudi Aramco.

Ayman has filed more than 20 patents and published several papers.

He received his B.S. degree in Industrial Chemistry from King Fahd University of Petroleum and Minerals (KFUPM), Dhahran, Saudi Arabia, and an M.S. degree in Entrepreneurship for New Business Development from Open University Malaysia, Bahrain.

Novel Methods for Production Data Forecast Utilizing Machine Learning and Dynamic Mode Decomposition

Dr. Anton Gryzlov, Dr. Sergey Safonov, Muqbil S. Alkhalaf, and Dr. Muhammad Arsalan

Abstract /

Multiphase flow rate measurements play an important role during the reservoir characterization and production optimization phase of reservoir management. The accurate multiphase flow rate measurement is an indispensable tool for production optimization from oil and gas fields. One of the industry's accepted solutions is the use of multiphase flow meters, which are expensive, have a limited operational envelope, and are exposed to erosion and failures. This can limit the applicability of physical metering devices due to frequent calibration, transportation issues, space, safety, security, and possible high costs.

Virtual flow metering (VFM) is a method for estimating oil, gas, and water flow rates produced from wells without measuring them directly. The method uses data available from the field, such as downhole pressure and temperature measurements as well as a choke position and electric submersible pump operational parameters, to estimate the flow rates by implementing hydrodynamic multiphase models, measurement data, and a reconciliation algorithm.

In this article, an overview of the conventional multiphase flow metering solutions is presented, which is followed by the application of some advanced artificial intelligence and data analytics techniques for a specific case of multiphase production monitoring in a highly dynamic wellbore.

The considered case refers to a typical scenario, where the measurements of oil, gas, and water flow rates are obtained in real-time using a topside multiphase flow meter. Alternatively, the values of these multiphase rates are estimated using a data-driven dynamic flow model obtained using a dynamic mode decomposition (DMD) technique. The results obtained with this method are compared with another VFM approach, where the rates are obtained using a deep long short-term memory (LSTM) neural network.

Introduction

Accurate and consistent measurements of multiphase rates allow operators to make decisions for better reservoir characterization, production monitoring, and reservoir management. The availability of such measurements is strongly related to the performance of monitoring equipment, which is used to obtain oil, gas, and water flow rates from each well. Currently, there are two industry established approaches, where the flow rates are measured either by a test separator or by a multiphase flow meter. Application of both abovementioned techniques has advantages and disadvantages[1], but generally, this metering equipment requires additional well instrumentation, which is expensive to maintain.

Conversely, the increased availability of cost-effective downhole sensors dramatically raised the amount of data obtained from a wellbore. A virtual flow meter (VFM) is a computational model, which enables estimation of multiphase production rates from the available raw data without measuring flow rates directly. VFM systems can be considered as a cheaper alternative to the conventional multiphase flow measurements, as they do not require additional hardware deployment.

The VFM, primarily using available pre-installed measurements — pressure and temperature gauges — can potentially serve as a cost-effective counterpart to physical flow metering devices. Depending on the balance between the availability of measurement data and modeling uncertainty, VFM algorithms can be classified as model-driven or data-driven[2].

The goal of the present work is to demonstrate the predictive capabilities of VFM using advanced data-driven techniques, such as the long short-term memory (LSTM) deep neural network and the dynamic mode decomposition (DMD). A synthetic example is considered, describing multiphase slug flow in a horizontal well with a riser, where downhole pressure and temperature measurements are used to predict topside rates of liquid and gas. The results demonstrate the superior performance of the DMD approach over a machine learning-based method in terms of computational performance and accuracy.

This article is organized as follows: first, the traditional multiphase flow metering solutions are introduced with the analysis of the main technological features and specific advantages and limitations. Second, the VFM concept description is introduced, including discussion on the main approaches and techniques used in academic and industrial applications. Afterwards, the application of DMD and deep neural networks for a specific case of multiphase production monitoring is demonstrated, outlining the benefits of the data-driven model based on system identification principles.

Multiphase Flow Metering

A multiphase flow meter is a device for measuring liquid and gas rates in a multiphase flow. In the petroleum engineering nomenclature, multiphase refers to a flow, which consists of some or all the following phases: a liquid hydrocarbon phase (crude oil or gas condensate), a gas phase (natural gas or air), a water phase and a solid phase. Multiphase flow meters measure oil, gas, and water production rates in situ, i.e., without separating the flow components continuously at high sampling frequency enabling real-time production monitoring[3].

Despite more than a few decades of continuous development and multiple cases of successful deployment, there is still no single instrument, which is capable of accurately and consistently measuring three multiphase rates directly. The most common strategy is to use several measurement modules, each of them sensitive to a specific component of multiphase mixture, and to combine separate readings via complex data interpretation algorithms. Within this approach, the various sensors are employed to measure velocities of phases and the composition of multiphase flows — or the quantities, which are closely related to these.

Multiphase flow rates are deduced by combining instantaneous velocity and cross-sectional fraction measurements of the flow components via a computational algorithm. The number of required measurements can be reduced by mixing the flow, which equalizes the velocities of each phase, or by partial separation, where gas, for example, is removed from the multiphase stream and the problem of multiphase metering is reduced to a combination of single phase and two-phase measurements[4].

Next, the overview of common technologies used for fraction and velocity measurement is given. Note that the choice of described methods is not biased by a particular vendor and should be considered as the general analysis of measurement techniques available in commercialized products.

Component fraction measurement is not a trivial task as it depends not only on actual ratios of the fractions occupying the measurement volume, but also on the geometrical distribution of phases if these are not well mixed. Also, depending on the technology, the salinity of the water component as well as the different velocities of liquid and gas phases can influence the results of the fraction measurements.

One of the common technologies for fraction measurement is based on the use of radioactive methods, which are non-intrusive, sufficiently fast, and sensitive to the fluids with significantly different densities. Gamma densitometry is one of the most widely used radioactive techniques used in multiphase flow metering; however, the use of X-ray based generators and sensors is feasible[5]. The simplest layout is represented by a single-beam gamma densitometer, where the energy absorption is measured between a single collimated gamma ray source and a collimated detector, where the resultant beam intensity is determined.

The loss of intensity is proportional to the composition of the multiphase mixture and linear attenuation coefficients, meaning that the gas void fraction can be determined from the measurement if the water-to-liquid ratio is known (from other measurements). Alternatively, dual energy systems may be applied, which measures the attenuation properties at two distinct energy levels, thereby enabling the measurements of two fractions simultaneously[6].

The measured fractions correspond to the measurement volume confined by the size of the transmitted gamma beam, wherefore it will only produce the valid results if the flow is homogeneously mixed. If the flow regime is different, a special correction needs to be applied; alternatively, a multi-beam configuration may be used. In the latter case, the measurements are taken with several detectors mounted at different circumferential locations of the pipe allowing the estimation of the actual flow regime[7]. It should be noted that using gamma densitometry statistical fluctuations in the attenuation measurement occur due to the random nature of the photon emission. It is necessary then to average the pulse-rated signal using an appropriate time window, which can be measured in seconds.

Another measurement technology, the electrical impedance, is measured in the flow volume between the excitation and detector electrodes where the oil-gas-water mixture is flowing. Depending on the actual fluid concentration, the flow can be either water continuous or oil continuous. In the first case, the conductivity of the multiphase mixture is measured, whereas the oil continuous flow is characterized by the capacitance of the mixture. The determination of the phase inversion point is not unique, and there is a range where the mixture is unstable and switching from oil continuous to water continuous.

Measurements of electrical impedance are based on the fact that dialectic permittivity of a multiphase mixture depends on the permittivity of its components and the actual distribution of the fluids in the cross-section of a meter[8]. Contrary to gamma attenuation methods, here the measurements are taken over the whole measurement volume defined by the dimensions of the electrodes. Subsequently, this method is still flow regime dependent and sensitive to gas content.

Given the different distributions of a gas phase, the electrical response may vary. Even for homogeneous flow, the interpretation model, which relates measured permittivity with phase fractions (such as Bruggeman),

implies that the entrained phase is represented by infinitely small elements of a spherical shape, which is not the case, even for bubbly flow. It is well-known that the permittivity of water depends on the conductivity, making this method highly sensitive to the salinity of water phase[9].

The measurements are affected by this dependence if the flow is water continuous. Despite all the challenges, the combination of impedance and gamma sensors are frequently used in the oil and gas industry, since the first technique is sensitive to water content, whereas the last allows us to determine the amount of gas in the multiphase stream. This is summarized in Table 1.

The most common method for velocity measurements is based on creating artificial contraction and measuring the differential pressure drop. The most common differential pressure measurements are based on the use of Venturi, though many other possible configurations are available (orifice, V-cone). When the differential pressure-based sensor is used, the assumption is made that the flow is well mixed and the velocity of all phases are equal. The Bernoulli law formulated under this condition of a homogeneous mixture relates the measured pressure drop to some averaged flow velocity and density of the mixture. The assumption of the well-mixed flow is supported by the Venturi configuration itself, where its converging part ensures a sufficient increase in turbulence providing additional mixing.

Another prominent method for phase velocity measurement is a cross-correlation technique. This is a commonly used method, applicable to track the changes of the nonuniform signal, which is typical for multiphase flows with gas. This technology is still applicable for only liquid flows; however, the sensitivity for liquid-gas flows is much higher due to a significantly different heterogeneity as the characteristic size of an oil droplet in water is significantly smaller than the typical bubble size.

The principle use of cross-correlation is based on the application of two identical sensors, which are positioned at a certain distance from each other. The output of each sensor is detected, where the similar patterns are identified using advanced data processing techniques. Assuming that the distance between the sensors is known, and the time-delay between two signals can be identified, the characteristic velocity can be defined. Note that the obtained variable still needs to be post-processed to acquire a physical meaning of the velocity of a dispersed phase. The big advantage of cross-correlation principles is that it can be built on almost every measurement technology, as it detects the variation in fluid property such as density, electric permittivity, or conductivity.

The velocity measurements for multiphase flows are summarized in Fig. 1, where the case of intermittent flow is considered.

The model for the measurement of multiphase rates treats the flow as four components: large gas bubbles, dispersed liquid-gas phase, which consists of oil, water, and gas dispersed as small bubbles in the liquid. The latter will be referred to as the dispersed gas phase for further discussion.

From the analysis of time series signals, the dynamic variation caused by the flow of the large bubbles through the measuring volume can be identified. Considering electrical impedance measurements, a large gas bubble results in a temporal decrease of the mixture permittivity signal and leads to a local increase of gas fraction.

Using the cross-correlation technique is then possible to calculate the velocity, corresponding to the dynamics of the large gas bubbles. The measurements of the dispersed phase are more relevant to the use of differential pressure instruments, such as the Venturi meter, as it provides a reading of the effective velocity of the homogeneously mixed multiphase mixture. The velocity of the gas phase can be calculated as:

$$Q_{GAS} = Q_{GAS\ Bubble} + Q_{GAS\ Dispersed} \quad (1)$$

While the first term in Eqn. 1 is clearly defined from using the cross-correlation measurement, the contribution from the dispersed gas needs to be separated from the Venturi readings. This implies that the relationship

Table 1 *Sensitivity of different measurement techniques for various production fluids.*

	Gas	Oil	Water
ε_r (-)	~1	~2	~80
σ(S/m)	~0	~0	~5
ρ(g/cm^3)	~0.05	~0.8	1
μ_{32kev} (cm^{-1})	0	0.2	0.4

Fig. 1 *A summary of the velocity measurement for multiphase flows.*

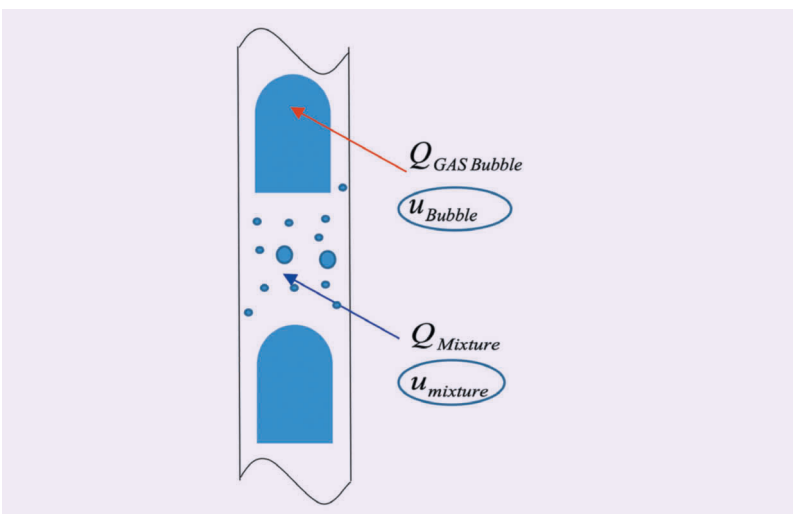

between the mixture velocity and the velocity of the dispersed gas phase needs to be established.

$$Q_{GAS\ Dispersed} = f(U_{mix}) \quad (2)$$

This concludes the overview of basic technologies for multiphase fraction and velocity measurements. As a summary, depending on the application and the actual production conditions, it is necessary to employ the multiphase meter with sensors sensitive to the specific fluid types. For example, for the wells with little or zero water cut, the impedance-based sensors are not feasible to use as the contrast between oil and gas permittivity is too small.

For the scenarios where the gas is absent, the gamma attenuation methods will fail and use of cross-correlation methods will not be that effective due to a lack of significant variations in flow. It has also been demonstrated that defining the flow rates from fraction measurements is not a trivial task, as it requires not only the use of multiple velocity measurements, but also some closure relationships, which are not uniquely defined.

By combining all the available measurements, the flow rates can be defined via some general function as:

$$Q = f(dP, \varepsilon_{mix}, U_{xcor}, P, T \ldots.) \quad (3)$$

VFM Theory and Applications

Considering the discussed technological challenges as well as high associated costs for multiphase flow meter operations, the alternative solution, such as VFM, needs to be explored for further applications. The main idea behind VFM is to consider instrumented wells and utilize the available measurements, which are readily accessible to estimate the multiphase rates via some mathematical model. The general equation for VFM to estimate multiphase flow rates can be given as:

$$Q = f(p_1, T_1, p_2, T_2, p_3, T_3, dP_{esp}, Choke\% \ldots) \quad (4)$$

Here, the input measurements include the readings from downhole pressure gauges (p_1 - p_3), downhole temperature gauges (T_1 - T_3), pressure build up by electric submersible pump, choke opening, etc. Contrary to surface multiphase flow meters, where the measurements are taken locally on the flow via a compact hardware-based solution, the VFM concept represents a distributed software focused solution, where the measurements reflect the general changes in production dynamics.

Generally, two principal approaches for VFM do exist: (1) physics-driven, and (2) data-driven. The complete classification of the VFM methods is available[2, 10]. A physics-driven approach requires the application of a hydrodynamic numerical simulator, which calculates the values of flow variables. These calculated variables are later compared with the available measurements using some optimization algorithms. In addition, it is necessary to formulate the first principles governing equations, the exact definition of the wellbore geometry, the correct values of numerous input parameters, and the choice of a proper numerical method.

A data-driven approach, conversely, does not require any prior information on process physics. Rather, it is based on collecting all the available measurements and establishing the hidden relationship between these measurements, and the target flow rates via some mathematical and statistical techniques. It can be considered as a part of the system identification method, where the underlying dynamics are estimated from analyzing the input/output data rather than trying to rigorously describe it using the physics-driven approach. The main disadvantage of the data-driven approach is the lack of generality and problems with extrapolation to the data outside the training range.

The use of a generic data-driven VFM can be formulated in a following paradigm. All the dynamic information is considered as time series $x_i(t)$ and $y_i(t)$, where x is the vector of input parameters (known as features in machine learning nomenclature), and y represents the output vector of the target flow rates. Normally, the input features correspond to the measurements available for time-related predictions, e.g., readings from pressure and temperature gauges. Moreover, it is possible to construct structures that are more elaborate where the input vector also includes the past values of multiphase rates to improve the future prediction.

This method is referred to as recurrent feature engineering. A mathematical formulation of the prediction process can be given as the necessity to estimate the output value of y_i at the time, t, given the time series of the input features with a temporal length, l. This, in case the measurements are equally spaced in time, corresponds to the shifted time window of $t-l, t$. Given the set of training data, where the target flow rates are known, it is split into a finite number of overlapping sequences of l, shifted by a one-time step from each other. The resulting training input matrix can be represented as:

$$X = \begin{bmatrix} x_0 & \cdots & x_{TR-l} \\ x_1 & \cdots & x_{TR-l+1} \\ \vdots & \ddots & \vdots \\ x_l & \cdots & x_{TR} \end{bmatrix}. \quad (5)$$

Similarly, the array of production flow rates is defined as:

$$Y = [y_t \quad y_{t+1} \quad \ldots \quad y_{TR}]. \quad (6)$$

Here, the subscript TR corresponds to the number of data points in the training sequence. The data-driven VFM defines the numerical operator, which maps every column of X to the entries of vector Y.

$$X(t) \rightarrow Y(t). \quad (7)$$

A traditional approach for defining this mapping operator, Eqn. 7, is based on the application of artificial neural networks, where the most promising results have been obtained with recurrent neural networks, such as the LSTM approach[11]. This method was used with

synthetically generated simulator data to demonstrate the predictive capabilities for the severe slugging scenario of multiphase flow in a pipe[12].

The superior performance of LSTM over a feed-forward neural network was demonstrated in Omrani et al. (2018)[13]. Some additional examples of the application of LSTM for the VFM purposes can be found in Loh et al. (2019)[14] and Sun et al. (2018)[15]. The LSTM maps the input sequences, x, to the output sequences, y, via a composition of linear transformation functions and nonlinear activation functions. The weights of the linear transformations are iteratively updated to minimize the loss function, which defines the difference between the predicted and target sequences.

In this work, the different approach is also considered. DMD is used to construct a data-driven model for the estimation of production flow rates. The DMD originates from the fluid mechanics as a tool for analyzing the dynamics of nonlinearly evolving flows[16]. Based on a singular value decomposition and tensor algebra, the DMD computes sets of modes, each of which is associated with the underlying dynamics of flow processes and characterized by the frequency and growth/decay rate. In addition, the DMD acts like a model reduction algorithm effectively extracting the most relevant dynamic information from the data. The mapping defined by Eqn. 7 is achieved by constructing a high order linear tangent approximation to the underlying multiphase flow dynamics. The significant difference between DMD and other machine learning methods is how the data-driven model is formulated. With the DMD, a dynamic operator explicitly defines the relationship between previous and future measurements. This allows its use for predictions or applying the derived model for optimization tasks.

Although DMD has an abundant history of applications in different aspects of experimental and computational fluid dynamics, it has a very little exposure in the field of VFM. Filling this niche is one of the objectives of this research article. Both LSTM and DMD has been applied as a research prototype of a VFM tool for analyzing highly dynamical production data examples.

Numerical Experiments

Figure 2 is a simple example of the production system for a VFM application. A long horizontal segment followed by a vertical part of the well defines the well geometry. The last part of the horizontal section is slightly inclined downwards to induce terrain slugging. The inflow from a reservoir to the wellbore is defined by three separate volumetric source terms placed along the horizontal part of the well at different positions. These source terms are the simplified representations of different perforation intervals where the fluid from the reservoir enters into the wellbore.

The wellbore's performance is controlled using a choke that is installed topside. In addition, the pressure and temperature gauges are placed at the entry point of the vertical part of the well. Assuming that only the pressure and temperature gauges are available as the downhole measurements, they are required to attain an estimation of the topside multiphase flow rates. The performance of the model can be improved if additional measurements are taken into consideration. These could include more information from downhole gauges or data from the distributed fiber optic sensors.

Transient data for this scenario is depicted in Fig. 3. The simulations were performed for 4 hours of production, where after the first hour the choke settings have been changed. Then, after two more hours of production, these choke settings returned to its initial value. The simulations have been performed with the commercially available multiphase OLGA simulator.

Following Figs. 2 and 3, the problem of VFM can be defined as follows. Given the time series of pressure and temperature measurements, it is necessary to predict the time series behavior of the output flow rates. Although it is necessary to predict the whole sequence of multiphase flow rates, the prediction is performed

Fig. 2 *A simple example of the production system for a VFM application.*

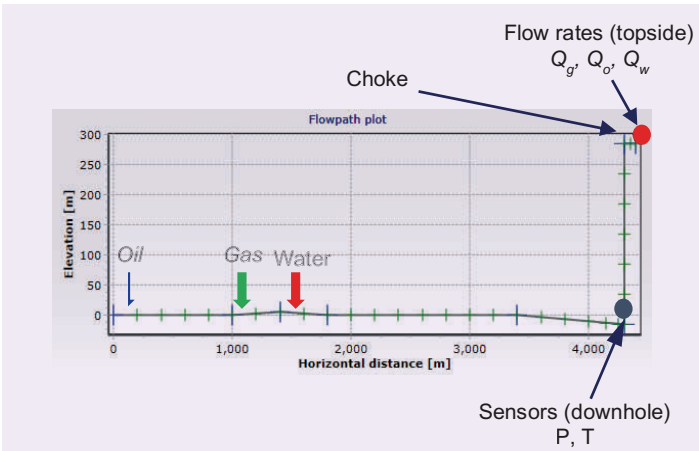

Fig. 3 *Downhole pressure and temperature measurements used as inputs.*

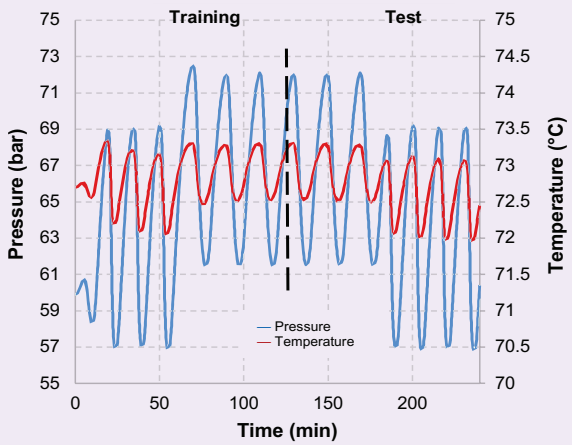

within the same time interval when measurements are available. This is different from the forecasting problem, where the measurements at present and past are used to predict the future values of multiphase rates. Figure 4 illustrates the general VFM workflow.

Following general machine learning ideology, we split all the available data into training and test sets by a 50%-50% ratio. The first 50% of data is used to define a mapping operator, whereas the last data set is used to check the resulting performance in terms of the defined metric. Although the simulations with OLGA have been initially performed for a three-phase scenario, eventually the flow rates of oil and water have been summed up to ensure that the number of input measurements is sufficient to estimate the rates.

The DMD model has been set with $l = 100$ time steps (Eqn. 5) and used 100 main eigenvalues as input parameters. For the LSTM model, all the training data has been split into overlapping sequences with $l = 80$ time steps length each. The architecture of the deep LSTM network included three hidden layers with 30 memory cells at each layer. These network parameters were iteratively defined by trial and error. Figure 5 illustrates the multivariate prediction workflow. For forecasting the t index of the target rates, t will be displaced forward, relative to the input feature denoting the relationship to future time.

Figure 6 shows the estimated gas flow rate with DMD, and Fig. 7 shows the estimated total liquid flow rate with DMD. The important conclusion is that DMD is capable of dealing with data, which is not only fully transient, but also subject to some external control. In this scenario, the choke position affects the pressures, which in turn defines the flow rates at the topside location. For the quality metric, the average relative error has been used. Note that the error was calculated for the entire data set, including both the training and test data. The relative error for each predicted flow rate is calculated as:

$$error = \frac{|Q_{PREDICTED} - Q_{TRUE}|}{Q_{TRUE\ MAX} - Q_{TRUE\ MIN}} \cdot 100\% \quad (8)$$

The average relative error of the DMD predictions was 0.3% for the liquid flow rate and 0.6% for the gas flow rate, respectively. Figure 8 shows the estimated gas flow rate with LSTM, and Fig. 9 shows the estimated total liquid flow rate with LSTM. The average relative error of LSTM predictions was 2.1% for the liquid flow rate and 1.4% for the gas flow rate, respectively.

The LSTM performance decreases after the data period when the choke opening is restored to its initial value. This may be because the training data set does not include such a transition since the LSTM is highly

Fig. 4 *The general VFM workflow.*

Fig. 5 *The multivariate prediction workflow.*

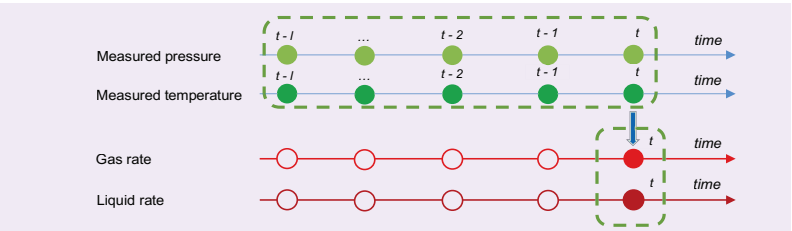

Fig. 6 *Estimated gas flow rate with DMD.*

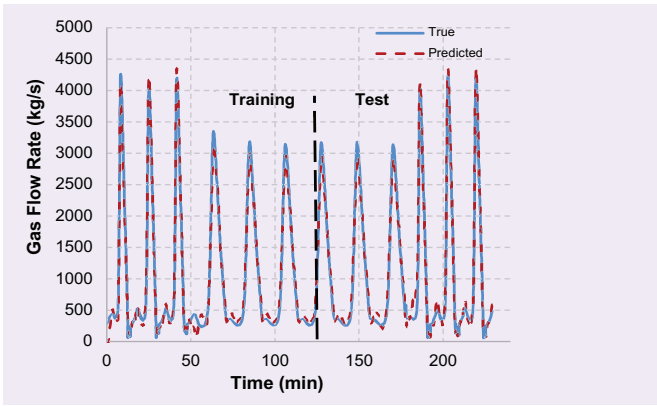

Fig. 7 *Estimated total liquid flow rate with DMD.*

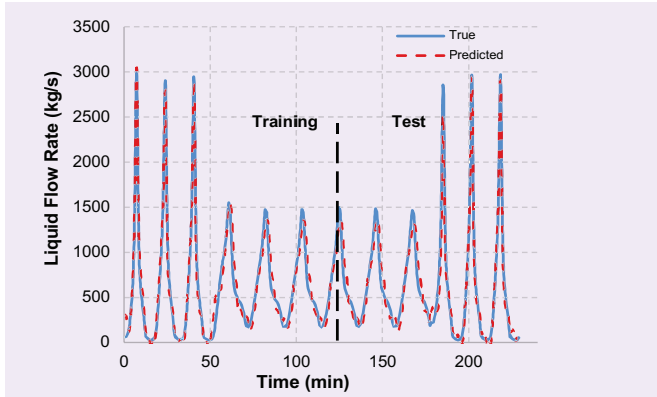

Fig. 8 Estimated gas flow rate with LSTM.

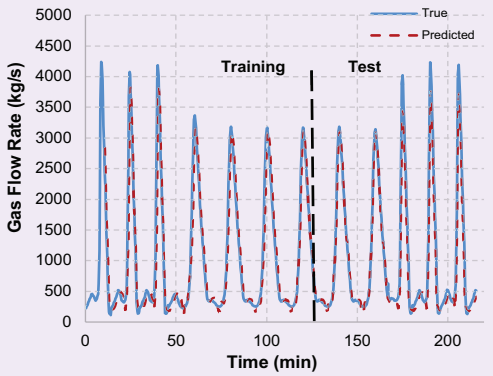

Fig. 9 Estimated total liquid flow rate with LSTM.

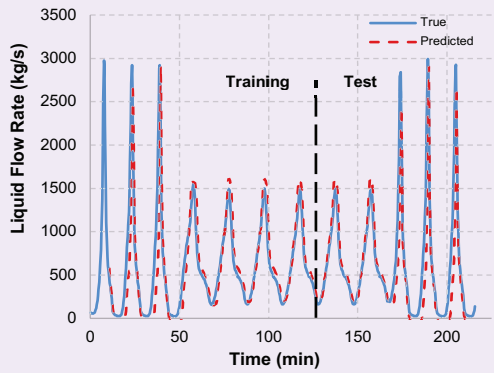

nonlinear — contrary to the DMD, which is based on a combination of tangent models. It is also important to mention that the computational effort with the DMD is sufficiently smaller than with the use of the LSTM. The total time for training of the LSTM was about 30 minutes, whereas it is approximately 1 minute with the use of the DMD, utilizing the similar computational hardware used for both simulations.

Conclusions

As it follows from the demonstrated results, the suggested data-driven approach is a promising tool to analyze production system dynamics and is able to make the predictions directly from the data. The obtained results can be summarized as follows:

- In an emerging method, DMD can be used for the system identification purposes and is therefore applicable for VFM applications.
- Contrary to "standard" machine learning methods, DMD requires significantly less computational time and work to prepare the model for analysis.
- Although promising, additional research activities are required to be more conclusive before the DMD method can be put in practice for real-time field data applications. One of the important points for further investigation is the analysis of the sensitivity of the DMD method to measurement noise and drifts.
- In this work, the benefits of the data-driven approach have been demonstrated for the VFM; however, a similar technique can be used as well for other applications. Consequently, this would require additional study to identify what instrumentation is needed for such scenarios.

Acknowledgments

This article has been prepared for presentation at the Abu Dhabi International Petroleum Exhibition and Conference, Abu Dhabi, UAE, November 9-12, 2020.

References

1. Falcone, G., Hewitt, G.F., Alimonti, C. and Harrison, B.: "Multiphase Flow Metering: Current Trends and Future Developments," SPE paper 71474, presented at the SPE Annual Technical Conference and Exhibition, New Orleans, Louisiana, September 30-October 3, 2001.
2. Amin, A.: "Evaluation of Commercially Available Virtual Flow Meters (VFMs)," OTC paper 25764, presented at the Offshore Technology Conference, Houston, Texas, May 4-7, 2015.
3. Falcone, G., Hewitt G. and Alimonti, C.: *Multiphase Flow Metering: Principles and Applications*, Elsevier Science, 2009, 328 p.
4. Thorn, R., Johansen, G.A., Hjertaker, B.T.: "Three-Phase Flow Measurement in the Petroleum Industry," *Measurement Science and Technology*, Vol. 24, Issue 1, October 2012, pp. 233-957.
5. Tjugum, S-A. and Mihalca, R.: "X-ray Based Densitometer for Multiphase Flow Measurement," paper prepared for presentation at the North Sea Flow Measurement Workshop, Tonsberg, Norway, October 20-23, 2009.
6. Sætre, C., Johansen, G.A. and Tjugum, S.A.: "Salinity and Flow Regime Independent Multiphase Flow Measurements," *Flow Measurement and Instrumentation*, Vol. 21, Issue 4, December 2010, pp. 454-461.
7. Sætre, C., Johansen, G.A. and Tjugum, S.A.: "Tomographic Multiphase Flow Measurement," *Applied Radiation and Isotopes*, Vol. 70, Issue 7, July 2012, pp. 1080-1084.
8. Nyfors, E. and Vainikainen, P.: *Industrial Microwave Sensors*, Artech House, 1989, 351 p.
9. Bø, Ø.L. and Nyfors, E.: "Application of Microwave Spectroscopy for the Detection of Water Fraction and Water Salinity in Water/Oil/Gas Pipe Flow," *Journal of Non-Crystalline Solids*, Vol. 305, Issues 1-3, July 2002, pp. 345-353.
10. Bikmukhametov, T. and Jäschke, J.: "First Principles and Machine Learning Virtual Flow Metering: A Literature Review," *Journal of Petroleum Science and Engineering*, Vol. 184, January 2020, pp. 106487-106513.
11. Hochreiter, S. and Schmidhuber, J.: "Long Short-Term Memory," *Neural Computation*, Vol. 9, Issue 8, 1997, pp. 1735-1780.
12. Andrianov, N.: "A Machine Learning Approach for Virtual Flow Metering and Forecasting," *IFAC-PapersOnLine*, Vol. 51, Issue 8, 2018, pp. 191-196.
13. Omrani, P.S., Dobrovoschi, I., Belfroid, S., Kronberger, P.,

et al.: "Improving the Accuracy of Virtual Flow Metering and Back-Allocation through Machine Learning," SPE paper 192819, presented at the Abu Dhabi International Petroleum Exhibition and Conference, Abu Dhabi, UAE, November 12-15, 2018.

14. Loh, K., Omrani, P.S. and van der Linden, R.: "Deep Learning History Matching for Real Time Production Forecasting," *Proceedings of the First EAGE/PESGB Workshop Machine Learning*, Vol. 2018, November 2018, pp. 1-3.

15. Sun, J., Ma, X. and Kazi, M.: "Comparison of Decline Curve Analysis DCA with Recursive Neural Networks (RNN) for Production Forecast of Multiple Wells," SPE paper 190104, presented at the SPE Western Regional Meeting, Garden Grove, California, April 22-26, 2018.

16. Schmid, P.J.: "Dynamic Mode Decomposition of Numerical and Experimental Data," *Journal of Fluid Mechanics*, Vol. 656, August 2010, pp. 5-28.

About the Authors

Dr. Anton Gryzlov

Ph.D. in Applied Physics,
Delft University of Technology

Dr. Anton Gryzlov is a Petroleum Engineering Specialist working at the Aramco Innovations Global Research Center (GRC) in Moscow, Russia. He is involved in the development of intelligent solutions for multiphase flow metering and optimization and control.

Prior to joining the newly established Moscow GRC in 2019, Anton worked for 14 years in various positions related to different aspects of multiphase flow metering development and commercialization. This includes extensive R&D experience at Roxar and Schlumberger.

He is the author of more than 15 technical publications on fluid flow, including Society of Petroleum Engineering (SPE) proceedings and papers in peer-reviewed journals.

In 2005, Anton received his M.S. degree in Mechanical Engineering from Bauman Moscow State Technical University, Moscow, Russia. In 2010, he received his Ph.D. degree in Applied Physics from Delft University of Technology, Delft, the Netherlands.

Dr. Sergey Safonov

Ph.D. in Quantum Semiconductor Physics,
University of Exeter

Dr. Sergey Safonov is a Research Program Director working at the Aramco Innovations Global Research Center in Moscow, Russia. He is currently leading a new team of research data scientists focusing on developing new digital solutions using novel artificial intelligence, machine learning, and data analytics technologies.

Sergey has 15 years of R&D experience in upstream oil and gas gained from working on various research positions in Schlumberger in Russia and in the U.K. He has extensive experience in multidomain aspects of multiphase fluid flow, advanced core analysis, digital rock modeling, and drilling processes.

Sergey is the author of more than 30 scientific and technical papers, including Society of Petroleum Engineering (SPE) proceedings and papers in peer-reviewed journals.

He received his M.S. degree in Applied Physics from the Moscow Institute of Physics and Technology, Moscow, Russia, and his Ph.D. degree in Quantum Semiconductor Physics from the University of Exeter, Exeter, U.K.

Muqbil S. Alkhalaf

B.S. in Chemical Engineering,
University of Colorado

Muqbil S. Alkhalaf is a Chemical Engineer working in the Production Technology Division of Saudi Aramco's Exploration and Petroleum Engineering Center – Advanced Research Center (EXPEC ARC), where he works on providing Fourth Industrial Revolution (IR 4.0) based solutions and technologies, gaining extensive knowledge over the past two years. During this period, Muqbil has published and presented several technical papers.

He received his B.S. degree in Chemical Engineering with a minor in Computer Science from the University of Colorado at Boulder, Boulder, CO.

Dr. Muhammad Arsalan

Ph.D. in Electronics Engineering,
Carleton University

Dr. Muhammad Arsalan joined Saudi Aramco in 2013 as a Senior Research Scientist. He is leading a team of experts in multiphase metering, sensing, intervention, and robotics focus area within the Production Technology Division of Saudi Aramco's Exploration and Petroleum Engineering Center – Advanced Research Center (EXPEC ARC). Muhammad is also leading the global digital transformation team of EXPEC ARC in advanced sensing domain. His team is working on innovative surface and subsurface production monitoring, control, and optimization technologies.

Muhammad is a seasoned professional with over 20 years of experience in academia and various industries, including biomedical, space, chemicals, and oil and gas. He has over 100 international granted patents and publications related to integrated sensors, systems, and tools.

Muhammad is the recipient of several major national and international awards and distinctions for his entrepreneurial skills and his groundbreaking contributions to the innovation, research and technology development.

Muhammad is the co-founder of two North American technology startups.

In 2004, he was an Invited Researcher and Natural Sciences and Engineering Research Council–Japan Society for the Promotion of Science (NSERC–JSPS) Fellow with the Tokyo Institute of Technology. From 2005 to 2008, Muhammad was an NSERC Alexander Graham Bell Graduate Scholar with the Carleton University.

From 2009 to 2010, he was a National Aeronautics and Space Administration (NASA) postdoctoral Fellow. In 2010, Muhammad joined King Abdullah University of Science and Technology (KAUST) in Thuwal, Saudi Arabia, as an NSERC postdoctoral Research Fellow.

From 2011 to 2016 he was an Adjunct Research Professor with Carleton University, Ottawa, Canada.

Muhammad received his B.Eng. degree from the Institute of Industrial Electronic Engineering, NED University of Engineering and Technology, Karachi, Pakistan in 1999, and his M.S. and Ph.D. degrees, both in Electronic Engineering, from Carleton University, Ottawa, Ontario, Canada, in 2004 and 2009, respectively.

Additive Manufactured Shapes Used to Cure Total Lost Circulation Events

Graham R. Hitchcock

Abstract /

Lost circulation is a major cause of drilling nonproductive time. Lost circulation events can range from seepage, partial, severe, and total losses. Extensive ranges of lost circulation materials (LCMs) are available and commonly used to cure seepage and partial losses. Subsequently, severe and total losses are not curable using standard LCM solutions, and alternative time-consuming and expensive remedial solutions are required. A supplement to conventional LCMs has been designed to extend standard LCM loss curing capability and to cope with severe total loss circulation events.

Conventional LCM limitations are reported to be formation fracture widths up to 4 mm to 6 mm in size. Formation fractures greater than this limit will become problematic to cure using conventional LCMs, the fractures are too large for LCM to collect, bridge, and create an efficient pressure seal between the formation and wellbore. When conventional lost circulation cure solutions prove ineffective, more costly solutions involving tripping and specific remedial treatments have to be utilized.

An additive manufactured shape used as a supplement to standard LCM has been designed and tested, and has been shown to increase the loss curing capabilities of the standard LCM to larger formation fractures typical of total lost circulation events.

The additive manufactured lost circulation shape (LCS), when used with existing and readily available LCM products, has been shown to extend the plugging range of a LCM from the typical 4 mm to 6 mm to larger total loss fractures of 20 mm to 40 mm. The lost circulation supplement deployed with a standard LCM will extend the loss curing capability of existing standard LCMs. By extending the curing capabilities of the standard LCM's costly and time-consuming tripping, alternative lost circulation remedial solutions can be avoided.

Introduction

Lost circulation is a well-documented industry issue stemming back to when oil wells were first drilled, and today still represents a significant challenge when drilling an oil well. Drilling an oil well using standard drilling practice uses a drilling fluid to act as a primary safety barrier, a drill bit cooling medium, and a method to transport the drilling cuttings from a well as it progresses. Simplistically stated, the drilling fluid circulation process is down the drillpipe, back to the surface up the annulus, where the cuttings are removed, and then back down the drillpipe.

Lost circulation is exactly as the term describes in that drilling fluid (or cement) pumped down the drillstring no longer arrives back at the surface, but leaks into the formation through which it is being drilled. Lost circulation events can represent well control issues, significant drilling fluid costs, lost time in controlling and/or remedial curing operations. These issues are documented and add millions of dollars to the cost of drilling operations annually.

Lost circulation is described using several categories relating to the severity of the loss, and the mechanism of the loss event. These categorized descriptions are then used to catalog and describe the types of solutions available.

The volume of fluid that is lost or not returned to the surface categorizes the lost circulation severity. The widely accepted categories used are seepage, partial, severe, and total losses. Each of the four categories are defined with a loss flow rate, some generally accepted definition rates are listed in Table 1[1].

The mechanism for lost circulation can also be categorized, pore throat, induced and natural fractures, and vugs and caverns[2].

A final important consideration with lost circulation is whether the lost circulation is occurring within the reservoir or non-reservoir section of the well[3] as this will dictate the type of lost circulation treatment that can or cannot be used.

The most widely accepted method to cure lost circulation is the use of lost circulation materials (LCM).

Table 1 Lost circulation severity category definitions.

Category	Oil-Based Mud Loss Rate (bbl/h)	Water-Based Mud Loss Rate (bbl/h)
Seepage	< 10	< 25
Partial	10 to 30	25 to 100
Severe	> 30	> 100
Total	No Returns	No Returns

The concept of using LCM has been around since the beginning of oil and gas well drilling. An early patent in 1890 describes a method of introducing adhesive material into the drilling fluid[4]. This early application of curing lost circulation is the most simplistic concept of introducing a material into the drilling fluid that will plug and seal the holes/cracks/fissures through which loss is occurring. The understanding of the different mechanisms of lost circulation have advanced as to have the concepts to prevent loss circulation occurring in the first place, i.e., induced lost circulation. Techniques such as wellbore strengthening, managed pressure drilling, underbalanced drilling, and casing while drilling are all preventative techniques.

Most LCMs are good for seepage, partial and maybe severe losses, but the limit of most LCMs is between 4 mm to 6 mm, as curing total lost circulation events remains a significant challenge to the industry[5]. Total lost circulation events become more complicated to cure and typically utilize more severe options such as cement squeezes, gunk plug, polymer pills, etc. These solutions have to be carefully placed; they tend to be deployed as remedial operations and generally cannot be applied to a reservoir section, as they would cause permanent formation damage[6].

A new concept has been designed to be used in conjunction with standard LCM solutions typically suitable for seepage and partial losses, but capable of curing total loss circulation scenarios.

Concept

In simplistic terms, the issue with a total loss circulation event is that the formation fissure is too big for LCM to collect and bridge, as shown schematically in Fig. 1. The LCM is lost to the formation with the drilling fluid.

The concept proposed is to reduce the formation fissure size such that the standard LCM can then bridge and plug as designed. Reducing the formation fissure size will be achieved by introducing a LCM "catcher" shape. The shape will be deployed downhole through a standard drilling bottom-hole assembly (BHA), allowed to flow into the formation where it would become wedged, Fig. 2a. Once the shape is trapped within the formation fissure, a deployed LCM would collect and

Fig. 1 A schematic of the standard LCM and total loss event scenario.

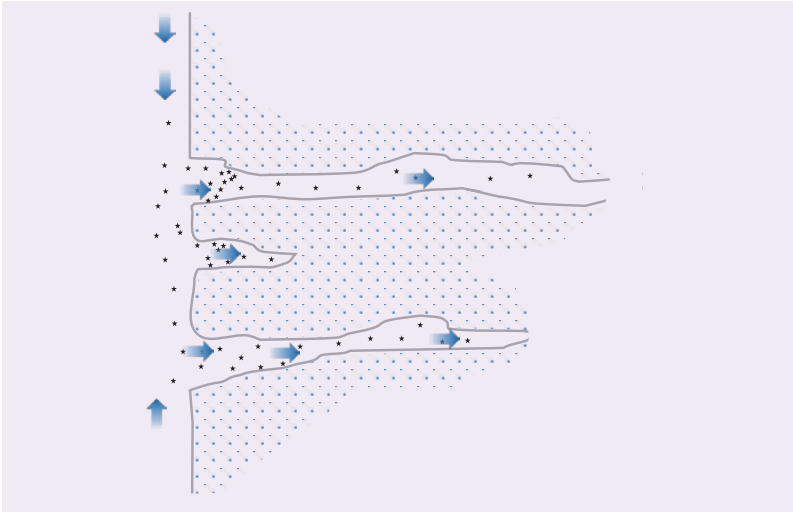

Fig. 2 (a) Deployment of lost circulation shape, and (b) The LCM deployment interaction.

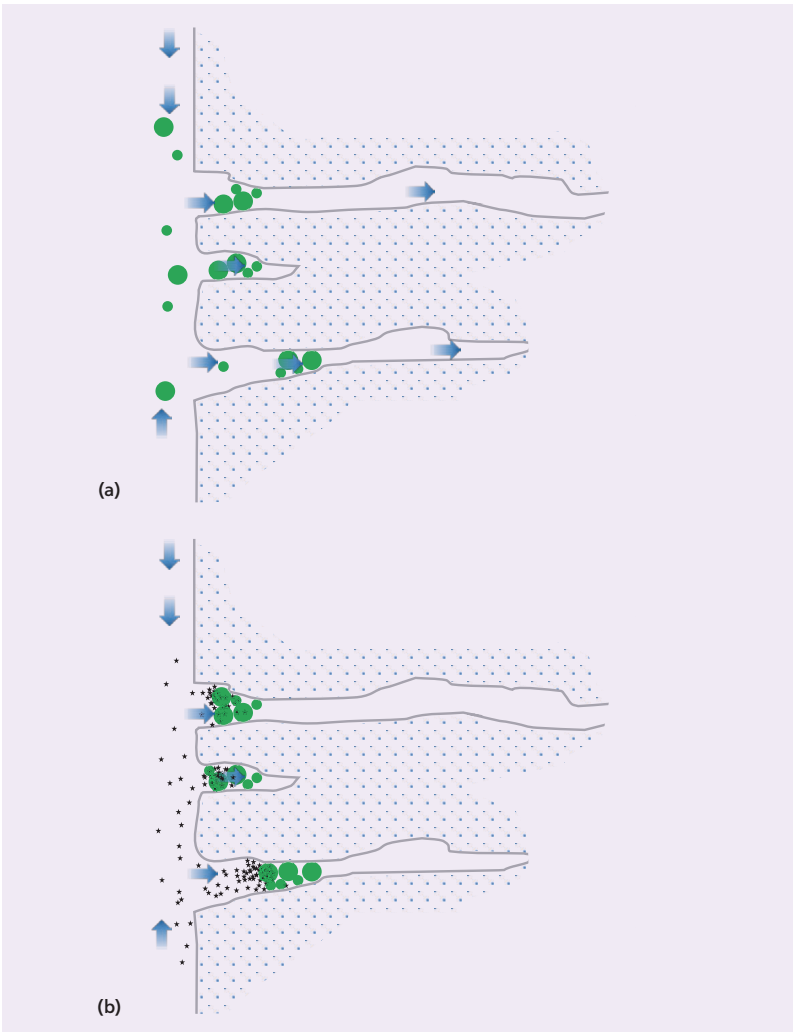

bridge on the shape, creating a formation pressure seal and curing the loss, Fig. 2b. The concept has been called a lost circulation shape (LCS).

The operational concept of the LCS is that it is to be deployed under normal drilling operations — the deployment of the LCS does not require remedial operations, e.g., drilling BHA pulled out and remedial BHA run in hole. This concept consideration led to four basic LCS design requirements:

- The LCS must have a "neutral buoyancy" — a neutral buoyancy is required so the LCS will flow with the drilling fluid and be drawn into the formation thief zones.
- The LCS must be customizable to suit different drilling fluids; different LCMs and formation fissure characteristics where known.
- The LCS must pass through a standard drilling BHA circulating sub or a larger ported specifically designed drilling BHA deployment tool.
- The LCS must not create a stuck pipe scenario, i.e., LCS that is not drawn into the formation thief zones must be circulated out of hole and not allowed to accumulate within the wellbore.

The concept design is a hollow perforated shape. The shape perforation can be optimized to suit whatever LCM is used, i.e., the perforation shape and size matched to the optimum LCM bridging capability. The overall external shape of the LCS is not fixed and would be customized to the formation fissure's size and shape, and the best stacking combination.

Additive manufacturing has been selected as the most appropriate method to create the LCS. Additive manufacturing has become a widely accepted manufacturing process and allows the creation of single parts not possible to manufacture through traditional subtractive manufacturing — material removal — techniques. Additive manufacturing techniques allow the creation of complex 3D objects by building successive layers on top of each other. Each layer sticks to the preceding layer until a complete form is produced.

Many different materials can be used in this layering process, including metal, thermoplastics, ceramics, composites, glass, and even edibles and biomedicals. The ability to create complex geometry features (internal and external) in many different materials without the need for expensive molds or dies were the main considerations for producing the LCS using additive manufacturing. The flexibility of the process will allow the customization of LCS to suit specific total loss circulation events if required.

There are various additive manufacturing processes used today, the chosen technique for the proof of testing was stereolithography. Sterolithography uses a process of photopolymerization where an ultraviolet light source is directed into a vat of photopolymer resin, which causes local solidification of the resin. Parts can be 100% polymeric or ceramic bonded with polymer resin.

The material selection criteria for the initial prototype LCS was kept simplistic for qualitative observation as opposed to strength or density considerations. The use of a translucent polymer was used for the initial prototypes.

Three initial prototype concepts were considered. Two designs were simplistic spheres with different perforations: One sphere has simple circular perforations, and the other sphere design has small slots.

A third faceted concept was designed to observe the overall effect of shape stacking and consequent plugging performance. The stacking of simple spheres will generate relatively large spaces between the spheres. Using faceted shapes or combinations of faceted and sphere shapes will improve the stacking, and therefore, the LCM's catching performance of multiple LCSs in fissures, Fig. 3a. Figure 3b is an image showing prototype LCSs manufactured in two sizes.

Test Apparatus

A qualitative proof of concept testing campaign was conducted. The initial testing was kept qualitative to observe visually the deployment behavior of the LCS into various test orifices and the interaction of the LCM with the deployed LCS.

A custom-made test apparatus with two fluid circuits was designed to enable the observation of the LCS deployment into a test orifice using a simple test fluid. Then, the interaction of a LCS test fluid deployed into the LCM was observed. Figure 4 is a schematic of the test apparatus.

Flow through the test apparatus was controlled using a flow control exit valve, test fluids were contained in pressure vessels such that flow through the test chamber could be gravity fed or assisted with a back pressure.

For observation purposes the test chamber was made transparent, the test fluid used was water and the LCM

Fig. 3 *(a) LCS stacking schematic using one shape or a combination of shapes, and (b) An image showing prototype LCSs in two sizes.*

Fig. 4 *A schematic of the test apparatus.*

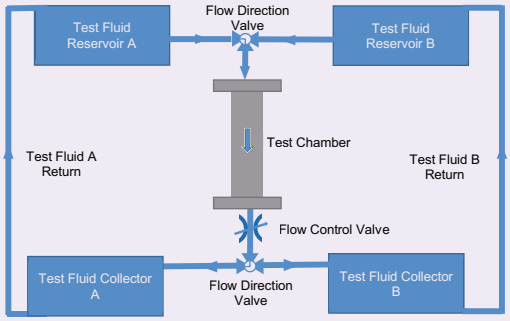

used was pine sawdust.

LCSs were introduced into the test fluid flow using a pressure isolated LCS introduction chute. Test orifices were positioned at the bottom end of the test chamber so that all fluid flow passed through the test orifice before exiting the test chamber. Figure 5 shows the test chamber and images of the actual test chamber used.

Two test orifice designs were utilized during the proof of concept testing. Figure 6a is an image of the initial plain hole orifice, and Fig. 6b is an image of the formation orifice. Figures 7a and 7b are detailed images of the formation orifices.

A qualitative flow test to give an indicative plugging performance of the LCM test fluid mix was conducted by running the LCM through a 4 mm slot at the test flow rate. The LCM test fluid mix passed through the 4 mm slot with no apparent plugging bridging, Fig. 8. The test fluid mix was therefore considered appropriate for the qualitative testing of the LCM in a total loss event scenario.

Results

Initial testing was conducted with the larger LCS and a plain hole orifice plate. A single LCS was deployed through the LCS introduction chute into the main test chamber, and then flowed into the test orifice. Once the

Fig. 5 *Test apparatus.*

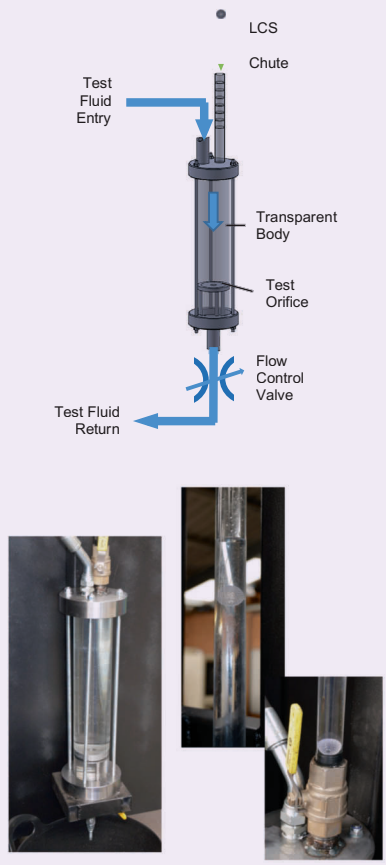

Fig. 6 *Plain hole orifice and formation orifice.*

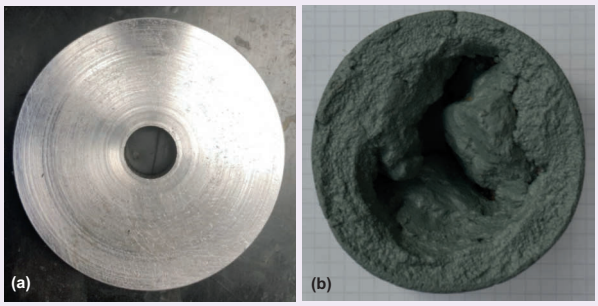

Fig. 7 *Formation orifice detail.*

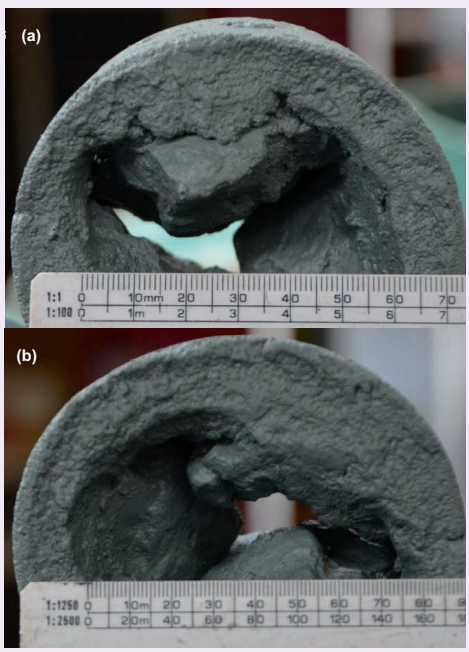

Fig. 8 *Results of a 4 mm slot flow test on with a test fluid/LCM mix.*

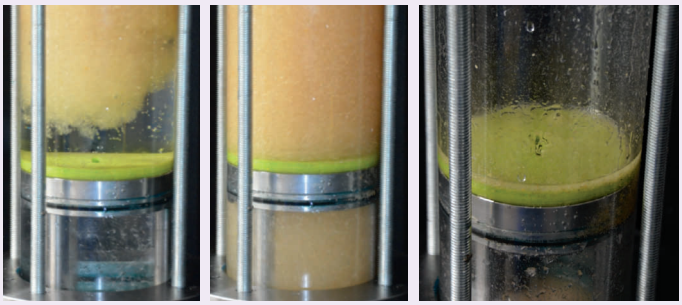

LCS was seated into the test orifice, the test fluid was switched to the LCM loaded test fluid and observed.

Figures 9a, 9b, 9c, and 9d shows a sequence of images taken from a high definition video stream of the test run using the faceted LCS. The LCS is shown landing and seating in the circular test orifice. No visible reduction of flow rate occurred once the LCS was seated in the test orifice.

Figures 9b, 9c, and 9d show the switch to the LCM loaded test fluid and its deployment into the test chamber, and then onto the seated LCS. No LCM was observed to pass through the seated LCS, which can be seen in Figs. 9b and 9c by the clear test fluid underneath the test orifice. A complete seal rapidly formed causing the flow to stop and the test fluid under the plugged orifice plate to drain away, Fig. 9d.

The plain hole orifice test was repeated for the two other prototype LCSs and the same results were obtained for each shape geometry, i.e., no LCM was seen to pass through the LCS and a complete seal was rapidly formed causing the flow to stop.

A second phase of testing was conducted using the formation orifice previously seen in Fig. 7, with multiple LCSs — both small and large. LCSs were deployed into the test fluid flow in a random combination, and then drawn into the formation orifice, Fig. 10. No significant reduction in the test flow rate was observed during the deployment of the LCS.

Figures 11a, 11b, 11c, and 11d shows a sequence of test run images, which shows a similar result to that shown in Figs. 9a, 9b, 9c, and 9d, but obtained for

Fig. 9 *The faceted LCS deployed to a circular orifice.*

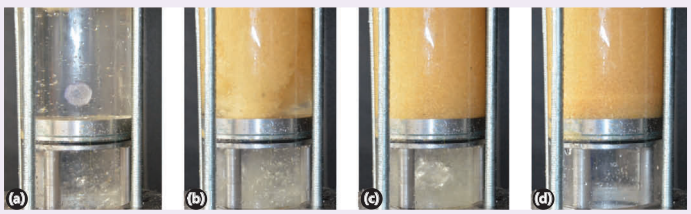

Fig. 10 *LCS deployment into the formation orifice.*

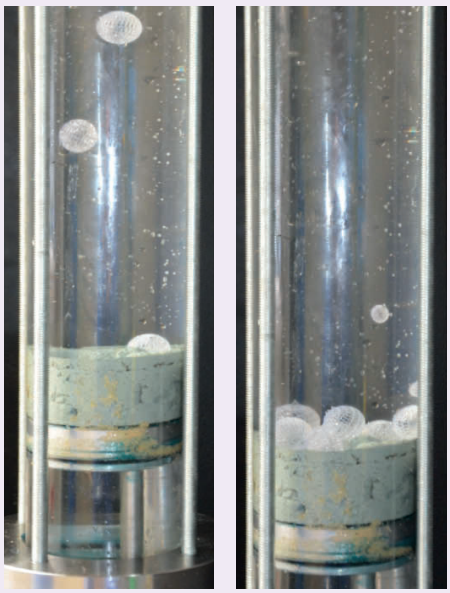

Fig. 11 *LCS deployment into the formation orifice.*

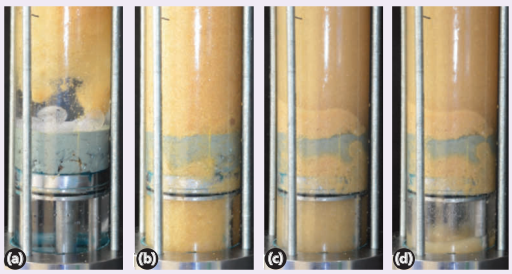

the formation orifice as the test fluid was changed to the LCM test fluid mix. Figure 11a shows the rapid deployment of the LCM test fluid onto the formation orifice and LCS followed by a rapid buildup of LCM in Figs. 11b and 11c. Unlike the results for the single hole test orifice, LCM was observed to pass through the formation orifice before a complete seal was obtained. The amount of flow through the LCM was reduced rapidly and a complete seal was obtained, Fig. 11d, where the test fluid has drained away from under the formation orifice and flow has ceased.

The post-test disassembly of the formation showed a good packing of large and small LCSs within the orifice, and the LCM spread within and between the LCSs, Fig. 12.

Conclusions and Further Development

Initial qualitative testing of the LCS has shown that the concept of a simple mechanical shape deployed into a large open orifice can extend the curing capacity of a

Fig. 12 *(a) The formation orifice, and (b) the orifice full of LCS and LCM.*

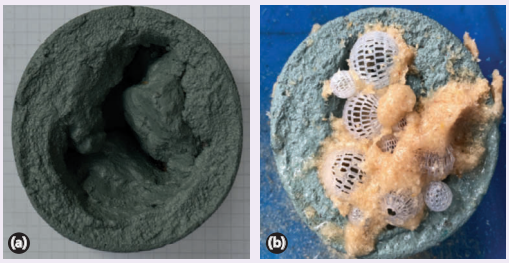

typical standard LCM, normally suitable for seepage to partial losses, i.e., orifices having less than a 4 mm opening. Large opening test orifices (> 10 mm) typical of those used in severe and total loss test scenarios have been successfully plugged.

Initial testing using the single hole orifice plate, although a perfect test scenario, i.e., a 20 mm sphere in a smaller 17 mm diameter hole, is considered a valid start point for the proof of concept. As seen in the results, the LCS once seated in the orifice allowed continued flow and caused no orifice seal. When the LCM was deployed, the seated LCS trapped all LCM causing the orifice to plug and seal. Post-test apparatus testing has shown the test LCM fluid mix was not capable of sealing a 4 mm test slot, which is considered near the limit of typical LCM sealing bridging capabilities.

The testing conducted has been purely exploratory and qualitative observation on the deployment of LCSs and the interaction of the LCS with the LCM. All testing has been conducted with a simplistic test fluid, LCM, and low-test pressures.

An extended test campaign using a single design of LCSs and alternative materials is planned to investigate the plugging capability of the LCS under pressure ratings typical of standard LCM testing regimes[7]. The optimum LCS size distribution, the optimum LCS material selection, and the most appropriate additive manufacturing technique for volume manufacture of the LCS will also be investigated in parallel to the extended test campaign.

Acknowledgments

This article was prepared for the Offshore Technology Conference, Houston, Texas, May 4-7, 2020.

References

1. Drilling Specialties Company: "Lost Circulation Guide," revised 2014/DSG, 82 p.
2. Ghalambor, A., Salehi, S., Shahri, M.P. and Karimi, M.: "Integrated Workflow for Lost Circulation Prediction," SPE paper 168123, presented at the SPE International Symposium and Exhibition on Formation Damage Control, Lafayette, Louisiana, February 26-28, 2014.
3. Savari, S., Whitfill, D.L. and Walker, J.: "Lost Circulation Management in Naturally Fractured Reservoirs," SPE paper 178165, presented at the SPE/IADC Middle East Drilling Technology Conference and Exhibition, Abu Dhabi, UAE, January 26-28, 2016.
4. White, R.J.: "Lost Circulation Materials and their Evaluation," API paper 56-352, presented at the Drilling and Production Practice Conference, NY, 1956.
5. Lavrov, A.: *Lost Circulation: Mechanisms and Solutions*, Gulf Professional Publishing, 2016, 264 p.
6. Alkinani, H.H., Al-Hameedi, A.T., Flori, R.E., Dunn-Norman, S., et al.: "Updated Classification of Lost Circulation Treatments and Materials with an Integrated Analysis and their Applications," SPE paper 190118, presented at the SPE Western Regional Meeting, Garden Grove, California, April 22-26, 2018.
7. Al-Arfaj, M., Amanullah, M. and Al-Ouhali, R.: "Loss Circulation Materials Testing Methods: Literature Review," SPE paper 193678, presented at the SPE International Heavy Oil Conference and Exhibition, Kuwait City, Kuwait, December 10-12, 2018.

About the Author

Graham Hitchcock

M.S. in Polymer Technology, Loughborough University

Graham Hitchcock is a Research Consultant at the Aramco Overseas Company (AOC), Aberdeen, Scotland. Since joining AOC in 2018, his work has been focused on developing drilling and completion tool technology.

Graham has more than 20 years of oil and gas industry experience, working with a major service company, and 5 years of experience working as a Researcher in Academia.

He is the author of more than 12 journal and conference publications.

Graham received his M.S. degree in Polymer Technology from Loughborough University, Loughborough, U.K.

A Novel Application of Filter Cake Remover to Free Differential Stuck Pipe

Peter I. Egbe, Fawaz N. Al-Mousa and Ahmed E. Gadalla

Abstract /

Historically, stuck pipe events have been shown to cost the industry several hundred millions of dollars per year, and over 30% nonproductive time (NPT)[1]. In all cases, remedial operations to salvage the subject well are expensive; and success is not guaranteed. This article describes a case history demonstrating how a differentially stuck string was freed in a relatively short time using an innovative enzyme/weak acid recipe.

The string was a 4½" lower completions bottom-hole assembly (BHA) comprising of swell packers and inflow control devices. The string was deployed in a carbonate reservoir. After deploying the string in the first 1,000 ft of open hole, the crew stopped to fill up the string to confirm circulation. Upon resumption of operations, the completions string was found to be stuck with no string movement possible in the upward or downward direction. Full circulation was still achieved. The fluid in hole was a water-based fluid.

The string was diagnosed to be differentially stuck. It was established that the stuck point was across the high permeable zone. Efforts to work the string free with glycol pills proved unsuccessful. An attempt to place 20% hydrochloric (HCl) acid induced up to 30 to 40 barrels per hour (bph) of dynamic losses at the shoe. Luckily, the losses healed relatively quickly, but the string remained stuck. After 29 hours of several unsuccessful attempts, a recipe of an enhanced combination pill of enzymes, and a weak acid accelerator was proposed, pumped across the stuck point, and allowed to soak. After a relatively shorter period of soaking, the string became free. The action of the enzyme/acid pill worked by destroying the polymer base of the filter cake created by the water-based drilling fluid. The homogeneous placement and action of the enzyme/weak acid pill across the stuck area ensured that it was more effective than the conventional HCl acid pill. Therefore, the application is being presented as a potentially safe, efficient, and cost-effective option to free a differentially stuck BHA in a water-based drilling fluid.

Success in freeing a stuck pipe usually depends on two critical factors: (1) an accurate diagnosis of the mode of stuck pipe event, i.e., differentially or mechanically; and (2) the ability to implement the remedial operations quickly, and effectively. By implementing this technique, significant NPT was averted. The technique has since been implemented in subsequent differential stuck pipe events in water-based drilling fluids with a 100% success rate.

Introduction

The demand for hydrocarbons has led to the necessity of exploring new ways to develop new or existing oil fields to keep up with the ever-increasing demand. Subsequently, the complexity to reach these reservoirs has proven to be constantly increasing, not only because some of these fields have been under production for many years, but also due to the requirement of optimizing reservoir contact, minimizing formation damage, and drilling with the lowest possible nonproductive time (NPT).

A need to design and construct wells for long-term economic value requires that specific downhole completions equipment are deployed to better manage well performance optimization regarding fluids off-take. Wellbore conditions, however, do present significant challenges that must be overcome to achieve the desired objectives.

Deploying downhole tubulars in total or partial loss circulation, high overbalance situations, or in wells with wellbore instability issues can result in unplanned stuck pipe events leading to significant NPT. Sometimes even with the best designs, there are still residual risks to the operations. Our ability to innovate using current or novel technologies and techniques, including assessing the right application through in-depth risk assessment, remain a collective strength to support drilling teams in achieving seemingly impossible objectives.

Stuck pipe events costs the industry significant amounts globally each year. Stuck pipe mechanisms can be classified as either mechanical (pack off/bridging and wellbore geometry), or differential. The classification of stuck pipe mechanisms differs from well to well, e.g., hole section being drilled, vertical or directional, and including geographical locations.

Historically, differential sticking mechanisms appear to contribute from 25% to 40% of the stuck pipe events[1, 2]. Additionally, the highest proportion of stuck events seem to occur when the string is stationary, which is a prerequisite for differential sticking. A typical statistical distribution of stuck pipe mechanisms, and the rig activities prior to stuck pipe events are detailed in Figs. 1 and 2, respectively.

The focus of this article is on differential sticking; which occurs against permeable formations when the string (drilling bottom-hole assembly (BHA), casing/liners, completions, or logging tools) embeds in the mud filter cake. The string is held in place by a mud pressure acting outwards from the wellbore into the formation, which exceeds the formation pressure by a significant overbalance pressure. The magnitude of "overbalance pressure" that results in differential sticking varies from well to well. What is known, however, is that the likelihood for differential sticking increases with increasing overbalance pressures if no mitigating actions are implemented.

The conditions for differential sticking to occur requires that the string remains stationary for an amount of time, or moving relatively slowly, opposite the permeable formation where a mud filter cake has built up over time. After a string becomes differentially stuck, the drillstring motion is lost with no reciprocation and rotation possible, although unrestricted circulation would be possible.

Differential sticking does not occur across low permeable formations (such as shales), where mud filter cakes do not normally form. The quality of the mud filter cake is critical for the avoidance of differential sticking, and the filter cake quality (thickness, lubricity, and strength) is influenced by a host of mud properties[3].

This article demonstrates that the destruction of the filter cake around a differentially stuck string using filter cake remover recipes is an application that presents an opportunity to free the string. By destroying or removing the mud filter cake, the hydrostatic pressure acting on the string is reduced/eliminated, and the string has a chance of being freed. Therefore, the application of mud filter cake removers have proven this to be a cost-effective and safe application to free differentially stuck strings in water-based muds (WBMs). For the application to be successful, however, a detailed mud filter cake analysis is required with confirmation that the filter cake remover recipe will be effective in destroying the filter cake[4].

Fig. 1 *Stuck pipe events mechanism.*

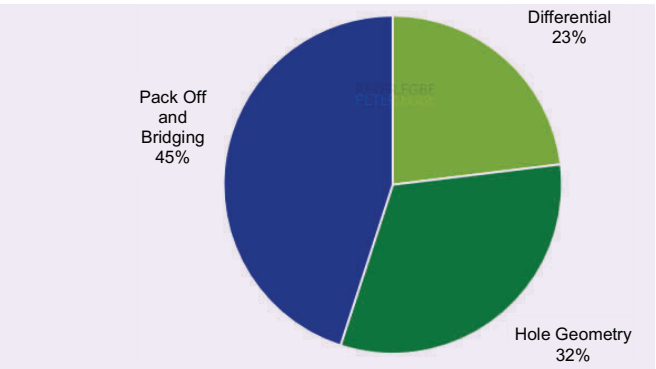

Fig. 2 *Rig activities prior to stuck pipe event.*

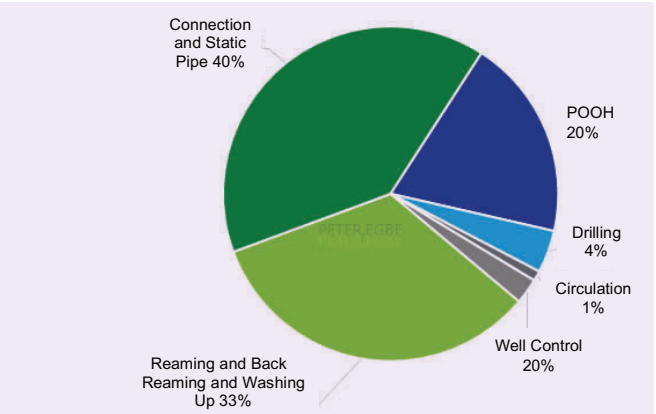

Effects of Filter Cakes on Differentially Stuck Pipe

It has been established that the force required to differentially stick a drillstring is influenced by a combination of the differential pressure, i.e., the overbalance pressure, in the wellbore, the contact area between the drill string and the mud filter cake, and the friction factor between the two[5]. This is illustrated by the equation:

$$F_{st} = \Delta pAf \quad (1)$$

where, F_{st} is the freeing force, Δp is the differential pressure between the wellbore and the permeable formation, A is the effective area of string in contact with the mud filter cake, and f is the coefficient of friction between the pipe and the mud filter cake.

Based on this relationship, Fig. 3, it is clear that the overpull force required to free a differentially stuck

Fig. 3 *Rig activities prior to stuck pipe event.*

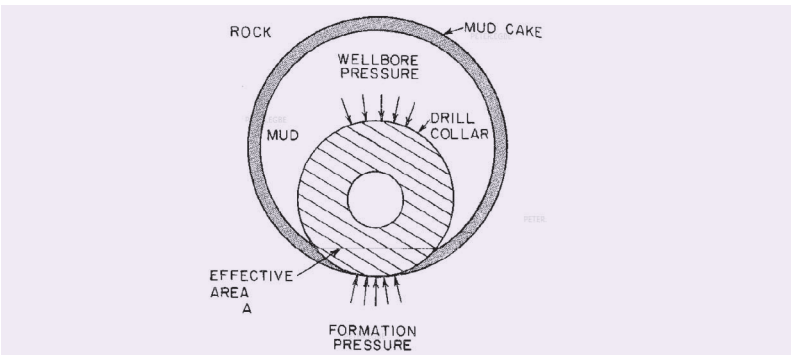

string increases with the rate of increase of the isolated portions of the string, which is equally dependent on the pipe-to-hole diameter ratio, and the rate of mud cake thickening. The ratio of the pipe-to-hole diameter affects the initial area of the pipe isolated from the hydrostatic pressure, and is time-dependent.

The rate of cake thickening (or cake build up rate) is driven by the mud characteristics and the formation permeability. The rate of cake thickening is also time-dependent. As time passes, if the mud filter cake is permeable, fluid loss continues, and the filter cake consequently thickens. Eventually, and with time, the filtration process through the mud filter cake continues, and the isolated portion of the string increases[6].

Therefore, as mentioned, the differential sticking force increases with time. Subsequently, the popular oil field understanding that the longer a string stays stuck, the harder it is to free.

Mud Filter Cake Treatment Using Enzymes and Weak Acids

Typically, in horizontal producer wells, treatment to remove the mud filter cake is done to improve long-term production[7]. The conventional treatment practice for the filter cake formed by water-based fluids utilizes strong mineral acids, buffered organic acids, oxidizers, enzymes, and chelating agents. Esters of organic acids have demonstrated improved filter cake removal efficiency by delaying acid release; although the same has been found to generally hydrolyze quickly.

Acetic, citric, and lactic acid precursors have been found to hydrolyze relatively slower, but do not provide the same efficiency to remove the filter cake[8]. Therefore, a balance needs to be struck, and is dependent on the properties of the reservoir formation under evaluation.

Water-based drill-in fluids commonly consist of xanthan gum, starch, cellulose, calcium carbonate, and salt. The filter cake that forms from these WBM drill-in fluids will typically be of acid soluble sized calcium carbonates, and in some cases, polymers. The most commonly used acid is hydrochloric (HCl) acid. Consequently, the high exothermic reaction rates of HCl acids imply that it creates wormholes with an increased potential for causing severe loss circulation, including a nonuniform filter cake removal treatment. The use of polymer breakers have equally been promoted, but have been found to be of reduced efficiency in breaking down carbonate particles[9].

Use of acid precursors — such as those of acetic, citric, and lactic acids — previously mentioned, have found good application within the industry. A major drawback of these acid precursors is the low acid strengths[10, 11]. Moreover, for the application to free differentially stuck drillstrings, it is exactly what is required, providing for slow reaction times necessary to ensure the treatment is circulated across the stuck string for uniform action on the filter cake.

This article presents a case history that exploits the capability of filter cake removal treatments as alternative applications for the freeing of drillstrings diagnosed to be differentially stuck. The same properties and principles of the filter cake treatment recipes remain the same, but the intended use and outcome differ in application. The advantage over conventional acid pills (of typically high concentration) includes delayed action, relatively cheaper cost, ease/safety of handling at the rig site, and general safety, e.g., logistics handling — storage and transportation, compared to traditional HCl acid or viscoelastic diverting acid applications.

Filter Cake Remover Treatment Design

The criteria for an efficient and effective enzyme/acid pill mud filter cake removal treatment recipe are as follows[8]:

- Remove the filter cake efficiently and overcome the disadvantages associated with conventional chemical means used for filter cake removal.
- Provide sufficient delay time for the treating fluid to be distributed uniformly in the treated areas for total zonal coverage, as well as for in certain well completions where significant delay time is needed for running operations. This is particularly desirable in horizontal/multilateral well applications.
- Provide a downhole reactive fluid to remove filter cake and formation damage caused by the filter cake with minimum corrosion tendency to the oil field tubulars.

Technical Approach

The adopted approach is a method of using chemically enhanced combinations of enzymes and a weak acid accelerator to free a differentially stuck work string. The action of the enzyme/acid pill works by destroying the polymer base of the filter cake created by the drilling fluids. The delayed and homogeneous action of the enzyme/acid pill across the stuck area ensures that pills are relatively more effective, and efficient compared to a conventional HCl acid pill. A conventional HCl acid pill has the potential to create wormholes leading to lost circulation, with no acid across the stuck pipe area, and an overall ineffective placement of the HCl pill across the stuck pipe zone.

Methodology and Application

The main component in forming any filter cake if using WBM is the polymer base and the solids size and type contained in the WBM. In this case, the fluid loss reducing polymers will form an emulsion base for the solids to be embedded.

The emulsion base is broken by the use of enzymes, acid, and an osmotic process to result in freeing the differentially stuck pipe. The risk or potential for differential sticking is usually exacerbated by a high difference between the wellbore hydrostatic pressure, and the reservoir pore pressure.

The methodology for placing the enzyme/weak acid pill to free the differentially stuck pipe is as follows:

1. Place a brine pill ahead of the enzyme/acid pill, which acts to dehydrate the filter cake through an osmotic process. The brine pill equally acts as a spacer.
2. Follow the brine pill with the enzyme/acid pill

prepared in a brine base. The enzymes work by breaking up the polymer base of the filter cake; while the weak acid in the pill formulation acts as a catalyst by accelerating the action of the enzymes, including dissolving of the solids. The enzyme/brine mix also acts by drying or shrinking the filter cake via an osmotic process; where the salt concentration is driven or determined by the salinity of the WBM. A high salinity WBM will require the use of freshwater, or a lower salinity fluid pill to create the osmotic drive required to dehydrate the filter cake.

3. A volume of the weak acid pill is then pumped behind the enzyme/acid pill. The goal of this weak acid pill is to react and dissolve the remaining solids that may be present in the filter cake. The type of solids contained in the WBM will determine the type and concentration of acid required in the formulation to react with the solids.
4. The displacement procedure and recipe needs to be properly optimized to get the best results, which is to free the stuck pipe.
5. After displacing the pills, it should be allowed to soak, while alternatively working the stuck string in tension and compression in a 30 to 60 minute cycle.

The methodology described here is best applied in wellbore drilling environments where the drilling fluid is water-based.

Results and Discussions

Well-A Case History

1. Background information:
   a. A single lateral producer with a 2,000 ft section in the target reservoir.
   b. An executed dedicated semi-stiff reaming trip to condition the hole prior to open hole mechanical caliper logs.
   c. An executed dedicated stiff reaming trip to condition the hole prior to running in the hole with the lower completion.
   d. Planned to deploy lower completions consisting of a liner hanger, inflow control devices, and swell packers.
   e. Run the completions string in the hole as planned, midway into the open hole. Stop to connect the top drive system to fill up, reciprocate the string, and check that the gravel pack valve shoe with a double float valve is not plugged.
   f. After connecting the top drive system, the string was observed to be stuck. No movement possible (up/down, and rotation). Full unrestricted circulation possible with 100% returns at the surface.
   g. Stuck pipe diagnosed as classic differential sticking.
2. Remedial actions taken:
   a. Citric acid available on the rig. The mud engineer was instructed to mix and spot the citric acid pill. Under displaced, and held some citric acid in the string. Allowed to soak for 8 hours.
   b. Slumped string with ±100 Klb slack off. No right-hand torque applied due to having a completions BHA in the hole. Maintained same while intermittently putting string in tension and refreshing acid in the open hole by 1 bbl to 2 bbl every 15 minutes. No success.
   c. Circulate out and condition the hole with mud, and dumped the citric acid at the surface. Flow checked. Well static. No losses.
   d. Mixed and spot 30 bbl glycol pill across the open hole. Allowed to soak for 8 hours while slacking string as per 2b. No success.
   e. Circulate out and condition the hole with mud, and dumped the glycol pill at the surface. Flow checked. Well static. No losses.
   f. Mobilized 20% HCl acid pills. Spot the acid pill as follows:
      - Pumped 10 bbl of brine and 25 bbl of weighted mud ahead as spacer.
      - Pumped 30 bbl of 20% HCl acid.
      - Followed up by pumping 10 bbl of brine and 15 bbl of weighted mud behind.
      - Observed immediate 30 to 40 barrels per hour (bph) loss circulation while pumping acid into the open hole. HCl acid created wormholes and induced losses.
      - Slumped string as per 2b. No success.
      - Loss rate reduced as HCl acid got spent. Regained full circulation once the acid was fully spent.
   g. Circulate out and condition the hole with mud, and dumped HCl acid at the surface. Flow checked. Well static. No losses.
   h. Mobilized enzyme. Spot enzyme/citric acid pill as follows:
      - Pumped 10 bbl of brine ahead as spacer + 80 bbl of enzyme + 50 bbl of citric acid + 10 bbl of brine.
      - Chased it with 80 bbl of mud. Under displaced, and held 20 bbl of citric acid in the string.
      - Maintained string slumped as per 2b. Allowed to soak. String free within 60 minutes despite being previously stuck for 29 hours.

Table 1 *The sample enzyme/citric acid soaking pill recipe for 100 bbl at 75 lb/ft³.*

Product	Concentration
Sodium Chloride Brine (75 pcf)	94% by volume
Enzyme S	1% by volume
Enzyme X	5% by volume
Citric Acid	1 ppb

Fig. 4 *The chemical structure of citric acid*[12].

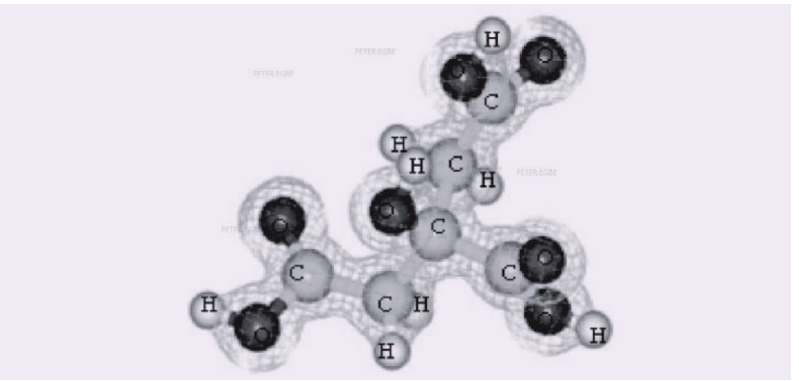

Table 1 lists the sample enzyme/acid soaking pill recipe for 100 bbl at 75 lb/ft^3.

The overall equation of the reaction of citric acid with calcite is given in Eqn. 2[12]:

$$2H_3AOH + 3CaCO_3 \leftrightarrow Ca_3(AOH)_2\,(s) \downarrow + 3H_2O + 3CO_2 \quad (2)$$

where $A = C_6H_4O_6$.

Figure 4 shows the chemical structure of citric acid.

Conclusions

An enzyme/weak acid mud filter cake remover recipe was successfully applied to free a differentially stuck lower completions string. The string was freed within 1 hour of displacing the filter cake remover across the length of the string in an open hole. The string became free relatively quickly despite being differentially stuck for 29 hours.

The innovative technique ensured that expensive pipe recovery, and potential sidetrack drilling operations were avoided. Subsequent lower completion strings were deployed successfully, and the subject well was delivered as per the planned objectives. By utilizing the properties of the mud filter cake to free the string, an estimated 14 days of remedial operations and associated operating expenditure was avoided.

Since the implementation of the technique in this case history, the same concept has been used in several other wells with success in water-based drilling fluids in the hole.

References

1. Muqeem, M.A., Weekse, A.E. and Al-Hajji, A.A.: "Stuck Pipe Best Practices — A Challenging Approach to Reducing Stuck Pipe Costs," SPE paper 160845, presented at the SPE Saudi Arabia Section Technical Symposium and Exhibition, al-Khobar, Saudi Arabia, April 8-11, 2012.
2. Alshaikh, A.A. and Amanullah, M.: "A Comprehensive Review of Differential Sticking, Spotting Fluids, and the Current Testing and Evaluation Methods," SPE paper 192169, presented at the SPE Kingdom of Saudi Arabia Annual Technical Symposium and Exhibition, Dammam, Saudi Arabia, April 23-26, 2018.
3. Reid, P.I., Meeten, G.H., Way, P.W., Clark, P., et al.: "Mechanisms of Differential Sticking and a Simple Well Site Test for Monitoring and Optimizing Drilling Mud Properties," SPE paper 35100, presented at the IADC/SPE Drilling Conference, New Orleans, Louisiana, March 12-15, 1996.
4. Bageri, B.S., Mahmoud, M.A., Al-Mutairi, S.H. and Abdulraheem, A.: "Filter Cake Porosity and Permeability Profile along the Horizontal Well and Their Impact on Filter Cake Removal," IPTC paper 18465, presented at the International Petroleum Technology Conference, Doha, Qatar, December 6-9, 2015.
5. Bourgoyne Jr., A.T., Millhelm, K.K., Chenevert, M.E. and Young Jr., F.S.: *Applied Drilling Engineering*, SPE Textbook Series, Vol. 2, 1986, 502 p.
6. Helmick, W.E. and Longley, A.J.: "Pressure Differential Sticking of Drill Pipe and How It Can Be Avoided or Relieved," paper API 57-055, presented at the Spring Meeting of the Pacific Coast District, Division of Production, Los Angeles, California, May 1957.
7. Degouy, D., Sofyan, M., Jaffar, M.B., Al-Naimi, A., et al.: "Engineered Formic Acid Precursor Helps Operator Successfully Stimulate Longest Open Hole Section in Carbonate Reservoir to Date," IPTC paper 18350, presented at the International Petroleum Technology Conference, Doha, Qatar, December 6-9, 2015.
8. Wang, X., Smith, K.L., Cutler, J.L. and Beall, B.B.: "Advancement in Acid Precursor Chemistry for Removal of Drill-in Fluid Filter Cake," SPE paper 147480, presented at the SPE Deepwater Drilling and Completions Conference, Galveston, Texas, June 20-21, 2012.
9. Cobianco, S., Albonico, P., Battistel, E., Bianchi, D., et al.: "Thermophilic Enzymes for Filter Cake Removal at High Temperature," SPE paper 107756, presented at the European Formation Damage Conference, Scheveningen, the Netherlands, May 30-June 1, 2007.
10. Siddiqui, M.A.A., Al-Anazi, H.A., Al-Ansari, A.A., Bataweel, M.A., et al.: "Evaluation of Acid Precursor Enzyme System for Filter Cake Removal by a Single Stage Treatment," SPE paper 99799, presented at the SPE EUROPEC/EAGE Annual Conference and Exhibition, Vienna, Austria, June 12-15, 2006.
11. Leschi, P., Demarthon, G., Davidson, E. and Clinch, D.: "Delayed Release Acid System for Cleanup of Al Khalij Horizontal Open Hole Drains," SPE paper 98164, presented at the SPE International Symposium and Exhibition on Formation Damage Control, Lafayette, Louisiana, February 15-17, 2006.
12. Al-Khaldi, M.H., Nasr-El-Din, H.A. and Sarma, H.K.: "Kinetics of the Reaction of Citric Acid with Calcite," SPE paper 118724, presented at the SPE International Symposium on Oil Field Chemistry, The Woodlands, Texas, April 20-22, 2009.

About the Authors

Peter I. Egbe

M.S. in Drilling and Well Engineering,
Robert Gordon University

Peter I. Egbe currently works as a Senior Drilling Engineer in Saudi Aramco's Exploration and Oil Drilling Engineering Department. He joined Saudi Aramco in 2014, and has over 20 years of experience working with BP International, TAQA Bratani (a subsidiary of Abu Dhabi National Oil Company), Energy Division (an arm of the U.K. Government's Health & Safety Executive responsible for regulating offshore oil and gas operations in U.K. waters), Total S.A., and Schlumberger.

Peter's interests are in drilling optimization through the application of new technologies, well and completions design optimization, and well integrity assurance throughout the well's life cycle from the design phase to well abandonment.

He holds professional certifications as a Chartered Engineer, and Chartered Petroleum Engineer from the Engineering Council U.K., and the Energy Institute U.K., respectively.

Peter received his B.S. degree in Chemical Engineering, and his M.S. degree in Drilling and Well Engineering, from the Robert Gordon University in Aberdeen, Scotland, U.K. He is currently pursuing a Ph.D. degree in Drilling & Well Engineering (degree in view autumn 2020) from his alma mater.

Fawaz N. Al-Mousa

B.S. in Petroleum and Natural Gas Engineering,
King Saud University

Fawaz N. Al-Mousa joined Saudi Aramco in 2011 as a Drilling Engineer working in the Exploration and Oil Drilling Engineering Department. His experience includes working with several service companies in optimizing the running of smart completions.

Fawaz has participated in several Society of Petroleum Engineers (SPE) conferences and events.

He received his B.S. degree in Petroleum and Natural Gas Engineering from King Saud University, Riyadh, Saudi Arabia.

Ahmed E. Gadalla

B.S. in Geology,
Menoufia University

Ahmed E. Gadalla joined Saudi Aramco in September 2014 as a Drilling Fluids Specialist working in the Drilling Operations Support Unit of Saudi Aramco's Exploration and Petroleum Engineering Center – Advanced Research Center (EXPEC ARC). He has over 20 years of experience in technical and operational procedures, including coordination and supervision of onshore and offshore operations in several countries.

Ahmed was trained as a Drilling and Completion Fluids Engineer and has advanced knowledge in the design and field applications of drilling fluids systems, well productivity, and drilling optimization.

He received his B.S. degree in Geology from Menoufia University, Al Minufya, Egypt.

Notes

Notes

Have an article you would like to publish? Here are our guidelines.

These guidelines are designed to simplify and help standardize submissions. They need not be followed rigorously. If you have any questions, please call us.

Length

Average of 2,500-4,000 words, plus illustrations/photos and captions. Maximum length should be 5,000 words. Articles in excess will be shortened.

What to send

Send text in Microsoft Word format via email. Illustrations/photos should be clear and sharp. Editable files are requested for graphs, i.e., editable in Excel.

Procedure

Notification of acceptance is usually within three weeks after the submission deadline. The article will be edited for style and clarity and returned to the author for review. All articles are subject to the company's normal review. No paper can be published without a signature at the manager level or above.

Format

No single article need include all of the following parts. The type of article and subject covered will determine which parts to include.

Working Title
Lorem Ipsum here.

Abstract
Usually 150-300 words to summarize the main points.

Introduction
Different from the abstract in that it sets the stage for the content of the article, rather than telling the reader what it is about.

Main body
May incorporate subtitles, artwork, photos, etc.

Conclusion/Summary
Assessment of results or restatement of points in introduction.

Endnotes/References/Bibliography
Use only when essential. Use author/date citation method in the main body. Numbered footnotes or endnotes will be converted. Include complete publication information. Standard is *The Associated Press Stylebook*, 52nd ed. and *Wesbter's New World College Dictionary*, 5th ed.

Acknowledgments
Use to thank those who helped make the article possible.

Illustration/Tables/Photos and explanatory text

If the files are large, these can be submitted separately, due to email size limits. Initial submission may include copies of originals; however, publication will require the originals. When possible, submit original images. Color is preferable.

File Format

Illustration files with .EPS extensions work best. Other acceptable extensions are .TIFF/.JPEG/.PICT.

Permission(s) to reprint, if appropriate

Previously published articles are acceptable but can be published only with written permission from the copyright holder.

Author(s)/Contibutor(s)

Please include a brief biographical statement.

Submission/Acceptance Procedures

Papers are submitted on a competitive basis and are evaluated by an editorial review board comprised of various department managers and subject matter experts. Following initial selection, authors whose papers have been accepted for publication will be notified by email.

Papers submitted for a particular issue but not accepted for that issue may be carried forward as submissions for subsequent issues, unless the author specifically requests in writing that there be no further consideration.

Submit articles to:

Editor
The Saudi Aramco Journal of Technology
C-3D, Room AN-1080
North Admin Building #175
Dhahran 31311, Saudi Arabia
Tel: +966-013-876-0498
Email: *william.bradshaw.1@aramco.com.sa*

Submission deadlines

Issue	Paper submission deadline	Release date
Summer 2021	February 9, 2021	June 30, 2021
Fall 2021	May 11, 2021	September 30, 2021
Winter 2021	August 12, 2021	December 31, 2021
Spring 2022	November 15, 2021	March 31, 2022

There is more.

A Step Change in Cementing — Mitigating Sustained Casing Pressure

Thomas Heinold, Dean S. Porter, Urooj K. Qasmi, and Salim Taoutaou

Abstract / Wellbore construction practices are complex; and achieving dependable zonal isolation is a critical and challenging process for optimizing asset life and minimizing future well intervention. Sustained casing pressure challenges related to poor zonal isolation are well documented and can affect production, which may require significant remedial well intervention. The need to address these challenges called for revisiting cementing operational practices and led to the development of a basis of design (BoD) document as a tool to help manage well design practices and standards.

First Worldwide Implementation of a New Multilateral Intervention Tool Facilitates Logging in Complex Multilateral Wells

Sajid Mehmood, Rifat Said, Alaa S. Shawly, and Zouhir Zaouali

Abstract / Reservoir monitoring, surveillance, and intervention present immense challenges in multilateral wells in terms of the availability of robust technology to access these wells. As more and more multilateral wells are drilled to improve the productivity or the injectivity of the formation, through a cost-effective and reduced footprint of well trees in the field, it is increasingly difficult to intervene in these wells and acquire the necessary data to map the flow profiles in producers or injectors. It has been a continuous endeavor of the oil industry to address these challenges by introducing new technologies in the field. To overcome these challenges, a new tool was developed to conduct production logging in multilateral wells, providing the access selectively to the desired lateral

Understanding Pitfalls of Nonreservoir Effects on Pressure Transient Test Data to Avoid Misleading Interpretation

Dr. N.M. Anisur Rahman, Sukru Sarac, and Bertrand C. Theuveny

Abstract / The determination of well and reservoir parameters is paramount during exploration, and the appraisal of new reservoirs are equally important during the development and production phases of a field. The interpretation of pressure transient test data is one of the tools to obtain such parameters under dynamic conditions. Often, this data is substantially influenced by nonreservoir factors such as gauge drift, adjacent noise due to natural or operational reasons, insufficient gauge resolution and dominant tidal effects. Any of these nonreservoir factors can significantly lead to a misleading interpretation of the formation. Rigorous vigilance against such occurrences is particularly important in designing deep transient well tests. The article quantifies these effects.

To read these articles and others, go to www.saudiaramco.com/jot

أرامكو السعودية
saudi aramco

Aramco
Journal
of Technology

Liked this issue? Sign up. It's free.

To begin receiving the *Aramco Journal of Technology* please complete this form, scan and send by email to ***william.bradshaw.1@aramco.com.***

Got questions?

Just give us a call at +966-013-876-0498 and we'll be happy to help!

Scan the QR code to go straight to your email and attach the form!

Subscription Form

Name

Title

Organization

Address

City

State/Province

Postal code

Country

Email address

Phone number

Number of copies